Evolution of vacancy-type defects in semiconductors: A positron annihilation study

Al-Abdulmalik, Dana A.

Award date:
2007

Awarding institution:
University of Bath

EVOLUTION OF VACANCY-TYPE DEFECTS IN SEMICONDUCTORS: A POSITRON ANNIHILATION STUDY

Dana A. Al-Abdulmalik

A thesis submitted for the degree of Doctor of Philosophy

University of Bath

Department of Physics

August 2007

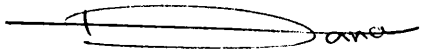

ProQuest LLC
789 East Eisenhower Parkway
P.O. Box 1346
Ann Arbor, MI 48106-1346

بِسمِ اللهِ الرَّحمنِ الرَّحِيمِ

﴿سُبْحَنَ الَّذِى خَلَقَ الأَزْوَجَ كُلَّهَا مِمَّا تُنبِتُ الأَرْضُ

وَمِنْ أَنفُسِهِمْ وَمِمَّا لَايَعْلَمُونَ﴾ يـــس 36

(Glorified is He who has created all the pairs of that which the earth produces, as well as of their own (human) kind (male and female), and of that which they know not) *The Noble QURÂN, Yā-Sīn 36*

Abstract

The study of defects is an exceptionally important branch of semiconductor physics, as defects govern many important properties of these materials. In this thesis, variable-energy positron annihilation spectroscopy (VEPAS) has been employed to acquire knowledge about the evolution of vacancy-type defects in semiconductors.

Evolution of vacancy-type defects introduced by low-energy (50keV) self-implantation has been investigated and compared in Czochralski (Cz)- and epitaxial (epi)-grown Si. The annealing behaviour of the defects was found to be relatively the same in both types; however, a slightly faster annealing rate was noted in Cz-Si, which is possibly due to the presence of impurities enhancing the clustering and the annealing processes. Low-temperatures (300-500°C) appear to cause migration and clustering of the defects, while higher temperatures (>500-640°C) were required to anneal away these clusters. High-energy (2MeV) self-implanted Cz-Si was also examined. Agglomeration of the implantation-induced defects was observed upon annealing at 600-650°C forming clusters, most likely of the size of hexavacancies. The response of open-volume defects, created by He^+ implantation and subsequent annealing, to different annealing ambients (nitrogen and oxygen) was inspected in $Si_{0.92}Ge_{0.08}$. Reduction in defect size was observed, the effect being larger for nitrogen, implying suppression of interstitial injection into the substrate during oxidation; this is contrary to what is known in Si.

Fluorine-vacancy (FV) complexes were directly observed in Si and Si-$Si_{0.94}Ge_{0.06}$-Si structures. With the aid of secondary ion mass spectrometry (SIMS), they were proposed to be of the form of $F_{3n}V_n$ or $F_{4n}V_n$, in Si and Si-SiGe-Si, respectively, with n most probably 1 and/or 2. These complexes were found (by SIMS) to significantly reduce boron transient-enhanced diffusion.

VEPAS has also been used to study defects in compound semiconductors. The formation and evolution of vacancy clusters was observed in 70keV He^+-implanted InP upon annealing at 640°C. In collaboration with optically-detected magnetic resonance spectroscopy, vacancy-type defects have been detected in Mg-doped GaN and they were associated with the detected red luminescence.

Acknowledgments

Throughout my journey to attain my ambition of completing my educational quest to achieve my PhD degree, I had tremendous support from pillars of light in my path, without which it wouldn't have been possible for me to be in this place at this time.

First, I pray in thanks and gratitude to Allah for the knowledge and all that I have been blessed with.

My greatest thanks are to my parents and especially to the voice of my beloved mother who was my eternal companion through all the years of my study abroad. In the darkest, coldest and loneliest of nights, comes her voice through the phone to shine light in my path, comfort me with her motherly care and remind me of how much she is waiting for my achievement. For her, coming from a very traditional upraising, it was the hardest decision she had to live with; leaving her youngest daughter all alone, thousands of miles away from home, and confronting the voices of disapproval. I can only say thank you very much Mom. I also thank all my sisters and brothers for their continuous support and for being there for me whenever I needed them.

Great appreciation goes to my extraordinary supervisor, Professor Paul Coleman. Whatever I said, I cannot express my gratitude to him. He has been a source of knowledge for me, providing support and encouragements when all roads lead to dead end. Thank you very much Paul, I can only thank you for all what you have done for me.

The other special appreciation is to my advisor from my first year in college until today. I cannot express my thanks to her; she played a great role in my academic achievements; and most of all she is a special friend of mine. Dr. Ilham Al-Qaradawi, I can only say thanks and hope one day I can do for others a little of what you have done for me.

Lastly; I want to express my gratitude to my country Qatar. Qatar opened all doors to me with generosity and support. I hope my achievement today can make Qatar proud of me.

This section cannot be ended without thanking all my lovely friends without whom I wouldn't have had enjoyable three years in Bath. Thank you very much my friends. Thanks to every helping soul and thank you for those who prayed for me once or lots.

Table of Contents

List of Figures

List of Symbols and Abbreviations

ACAR Angular Correlation of Annihilation Radiation
ADC Analogue-to-Digital Converter
B boron
c speed of light
C_d defect concentration
C_v vacancy concentration
Cz Czochralski
CEMA channel electron multiplier array
D_+ diffusion coefficient of positrons
DBAR Doppler broadening of Annihilation Radiation
DLTS deep level transient spectroscopy
e elementary charge
e^+ positron
e^- electron
E energy of implanted positrons
E_a activation energy
ΔE broadening in energy
EOR end-of-range
Epi epitaxial
EPR electron paramagnetic resonance
eV electronvolt
F fluorine
positronium fraction parameter
F_s fraction of positrons diffuse back to the surface
F_d fraction of positrons annihilate in defects
F_b fraction of positrons annihilate in bulk material **FZ** float-zone
FV fluorine-vacancy
γ gamma quanta
Γ gamma function
GaN Gallium Nitride
Ge Germanium
h Plank's constant
H Hydrogen
He Helium
HBT heterostructure bipolar transistors
HPGe High-purity germanium detector
HRXRD high-resolution x-ray diffraction
InP Indium Phosphide
IR Infrared spectroscopy
κ_{eff} effective escape rate of positrons from the diffusion process
κ positron trapping rate
k_B Boltzmann's constant
λ positron annihilation rate
defect decay rate
λ_b positron annihilation rate in bulk material
L positron diffusion
L_+ positron diffusion length in defect-free material
L_{eff} effective positron diffusion length
μ positron mobility
m shape parameter
m_o electron and positron rest mass
MCA Multi-Channel Analyser
MD Molecular dynamics
Mg magnesium
MOVPE metal-organic vapour phase epitaxy
ν specific positron trapping rate
$\Delta\nu$ frequency shift
n(z) positron density at a distance z from the surface
N_{at} atomic density
n_e electron density
ns nanoseconds
ODMR Optically detected Magnetic Resonance
P momentum
P(z,E) positron implantation profile
$P_{x,y}$ momentum component in x,y direction
P_z momentum component in z direction
PAL Positron Annihilation Lifetime

PAS Positron Annihilation Spectroscopy
PL Photoluminescence
ps picoseconds
Ps Positronium atom
o-Ps ortho-positronium
p-Ps para-positronium
$\Delta\theta$ angular deviation
ρ material's density
r_o classical electron radius
R range of implanted ions
R_p projected range
ΔR_P projected straggle
$\Delta R_\perp$ lateral straggle
RBS Rutherford backscattering
RT room temperature
RTA rapid thermal annealing
S spin
S (sharpness) parameter
ion dose per unit area
S_s characteristic S parameter in surface
S_d characteristic S parameter in defects
S_b characteristic S parameter in bulk
S_v characteristic S parameter in vacancies
Sccm standard cubic centimetres per minute
SEM Scanning Electron Microscope
Si silicon
SiGe Silicon-Germanium structure
SIMS secondary ion mass spectrometry
SiO_2 Silicon dioxide
SOI Silicon-on-Insulator
SPE solid phase epitaxy
τ positron lifetime
τ_b positron lifetime in bulk material
T Temperature
Tesla
TED Transient enhanced diffusion
TEM transmission electron microscopy
TRIM TRansport of Ions in Matter
V_2 divacancies
V_6 hexavacancies
V_{Ge} germanium vacancies
V_N nitrogen vacancies
VO vacancy-oxygen complexes
VEPAS Variable Energy Positron Annihilation Spectroscopy
VEPFIT Variable Energy Positron FIT
W W (wing) parameter
XTEM cross-sectional transmission electron microscopy
Z atomic number
$\bar{z}$ mean implantation depth

List of Publications

Below is a list of publications related to this thesis.

1. D.A. Abdulmalik and P.G. Coleman, Phys. Status Solidi C, accepted.

2. D.A. Abdulmalik, P.G. Coleman, H. El-Mubarak, and P. Ashburn, J. Appl. Phys. **102**, 013530 (2007).

3. D.A. Abdulmalik, P.G. Coleman, H.Z. Su, Y.M. Haddara, and A.P. Knights, J. Mater. Sci.: Mater. Electron. **18**, 753 (2007).

4. D.A. Abdulmalik, P.G. Coleman, N.E.B. Cowern, A.J. Smith, B.J. Sealy, W. Lerch, S. Paul, and F. Cristiano, Appl. Phys. Lett. **89**, 052114 (2006).

5. S. Zeng, G.N. Aliev, D. Wolverson, J.J. Davies, S.J. Bingham, D.A. Abdulmalik, P.G. Coleman, T. Wang, and P.J. Parbrook, Appl. Phys. Lett. **89**, 022107 (2006).

6. D.A. Abdulmalik, P.G. Coleman, and I.Y. Al-Qaradawi, Appl. Surf. Sci. **252**, 3209 (2006).

Chapter 1

Introduction

1.1 General Introduction

Of the many strange consequences of the theory of relativity, one of the most puzzling is the dichotomy of the natural world, the division of the universe into matter and antimatter, for each elementary particle there exists an antiparticle.

Though the discovery of the existence of the first antiparticle was an incredible mystery, nowadays scientists talk about and deal with these antiparticles easily, and the first known antiparticle, which is called the positive-electron or positron, has great speciality and importance in various aspects of life. Experimental techniques based on the positron annihilation concept have become a standard tool not only in research laboratories for probing matter down to atomic dimensions and studying defects at low and high temperatures, but also in industrial (e.g. diagnosis of manufactured materials) and medical (e.g. diagnosis of tumours) applications.

The work carried out in this thesis gives examples of the use of positrons to gain quantitative or qualitative information on structural changes of materials caused by device-fabrication techniques, such as ion implantation and thermal treatments.

The structure of this thesis is as follows. The rest of the present chapter is a general introduction; it gives a basic overview of positron physics, the annihilation process of the positrons, the experimental techniques of positron annihilation spectroscopy

(PAS), positron beams, positron depth profiling and positron's diffusion and trapping. Chapter 2 presents an insight into the different types of defects induced by ion implantation in semiconductors and their importance in some phenomena related to semiconductor device fabrication. In chapter 3, the experimental system used in performing the measurements of the present work and the data analysis method are described. From chapters 4 onwards, the experimental results of measuring specific samples are discussed. Chapter 4 deals with the evolution of vacancy-type defects generated by ion implantation in different types of Si upon various thermal treatments. Chapter 5 is concerned with the formation of fluorine-vacancy complexes in both Si and Si-SiGe-Si structure and the role of these complexes on the transient enhanced diffusion (TED) of B. Chapter 6 gives examples of the applications of PAS in studying vacancy-type defects in compound semiconductors, namely InP and GaN. Each chapter starts with brief review of some relevant earlier studies and ends with a concise conclusion. Lastly, an overall summary of the work presented in this thesis is given at the end.

1.2 Positrons

In early 1933 Carl D. Anderson published his most notable paper, 'The Positive Electron' [1]. This came to verify the theoretical assumption of the existence of the positron postulated by Dirac three years before as the "negative" energy solution in his theory of electron energy levels [2].

The positron, as the anti-particle of the electron, has a rest mass (m_o=511 keV/c^2) and spin (1/2) that are identical to those of the electron but a charge and magnetic moment that are opposite. It is stable in vacuum with a mean lifetime τ >2x10^{21} year [3], but in condensed matter it normally annihilates with an electron mainly via the emission of two γ photons each with 511 keV.

Positrons do not exist naturally in the world, however, they can be obtained either by the pair production process, the inverse of which is the pair annihilation, where

high enough energy γ photon produces e^--e^+ pair during its collision with matter; $e^+ + e^- \underset{\text{Production}}{\overset{\text{Annihilation}}{\rightleftarrows}} Energy$, or by β^+ decay of some radioisotopes, such as ^{22}Na.

1.3 Annihilation of Positrons

As mentioned above, positrons are stable in vacuum but, if electrons are present, the two particles wave-functions overlap and they annihilate predominantly by emitting two γ photons, $e^+ + e^- \rightarrow 2\gamma$, each with an energy of $m_o c^2 = 511$keV.

If both the positron and the electron are at rest at the moment of annihilation, the conservation of momentum will cause the two γ photons to be emitted collinearly in opposite directions each with an exact energy of $m_o c^2$. However, because of the non-zero momentum of the annihilating pairs, the annihilation photons are emitted with an energy of $m_o c^2 \pm \Delta E$ and at an angle of $180^\circ \pm \Delta\theta$.

The broadening, ΔE, of the 511keV annihilation line can be calculated from the electron momentum in the propagation direction, P_z;

$$\Delta E = \frac{P_z c}{2} \tag{1.1}$$

while the angular deviation, Δθ, can be determined from the momentum components, $P_{x,y}$, perpendicular to the propagation direction of the annihilation photons;

$$\Delta\theta_{x,y} = \frac{P_{x,y}}{m_0 c} \tag{1.2}$$

1.4 Positronium Atom

In some circumstances the positron can bind with an electron and form a positronium (Ps) atom with a vacuum binding energy of ~6.8eV. The Ps atom was

predicted theoretically by Mohorovicic in 1934 [4] and then observed by Deutsch in 1951 in his positron-lifetime measurements in nitrogen and other gases [5].

As a result of the fact that the positron and the electron are spin ½ particles, Ps can basically be formed in two ground states; 75% as ortho-Ps (o-Ps) with parallel spins (triplet state, $^3S_1$) and 25% as para-Ps (p-Ps) with anti-parallel spins (singlet state, $^1S_0$). The lifetime of p-Ps in vacuum is approximately 125 ps and about 142 ns for o-Ps. p-Ps annihilates intrinsically mainly into two γ-rays each with ~511keV, whereas o-Ps requires annihilation into three γ-rays in order to conserve charge parity. However, the positron wave function in high electron density materials could overlap with electrons outside the Ps. The annihilation with such electrons having an anti-parallel spin, the so called pick-off reaction, results in two γ-rays emission and reduces the o-Ps lifetime to a few ns.

Because of the large radius of the Ps atom, it is more likely to be formed in a relatively open structure materials such as gases and molecular solids compared to high electron density bulk materials, such as metals and semiconductors. It is normally found in defect-free solids in self-trapped states or it can be captured in structural defects such as vacancies and vacancy clusters. In some cases, Ps can also be found in semiconductors, for example it has been observed in porous Si [6,7]. However, as no large open-volume defects are normally present in the bulk of semiconductors, Ps may only exist at the surfaces. Hence, Ps measurements in semiconductors could be used as an indication of the fraction of positrons diffusing back to the surface. No positrons are diffusing back to the surface at high implantation energy and consequently no Ps can be formed, but its maximum formation can be obtained when positrons are implanted at low energies and also if high temperatures are applied; the latter desorb surface-bound positrons as Ps.

1.5 Positron Annihilation Spectroscopy

The basic principle of positron annihilation spectroscopy (PAS) is based on the fact that the annihilation γ photons carry information on the electronic environment at which the positron annihilates. Since positrons are attracted to

open-volume crystal defects because of the missing positive nuclei, the electronic environment being sensed is often that of defects in the sample under investigation. In the present section, brief discussion will be given about the basic physics of the three major PAS techniques, namely, Positron Annihilation Lifetime (PAL) spectroscopy, Doppler Broadening of Annihilation Radiation (DBAR) spectroscopy, and Angular Correlation of Annihilation Radiation (ACAR) spectroscopy. Prior to this, the general behaviour of how the positron slows down and traps into an open volume defect is reviewed.

When an energetic positron approaches a solid surface it may be scattered back or penetrate the sample. If it penetrates the material, it will rapidly thermalize within a few ps and slow down to a few tenths of eV. The thermalized positron then diffuses through the sample with a range varying from 10 to 1000 μm [8] depending on the maximum energy of the positron and the density of the sample. Eventually the positron either annihilates freely with one of the surrounding electrons or localizes during its diffusion by a positron trap, such as lattice defects, and then annihilates there, or diffuses back to the surface where it may be trapped in a surface defect or emitted as a free positron. Figure 1.1 summarizes the possibilities that the positron may undergo during its diffusion in the sample.

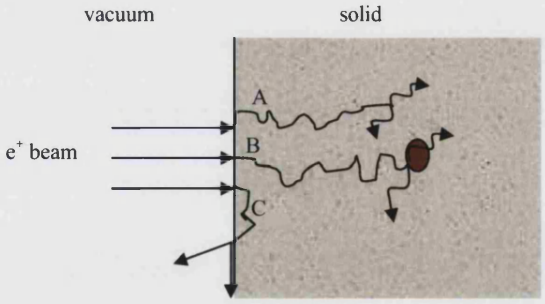

Figure 1.1 Possible interactions of energetic positrons entering a solid. A. Thermalization of implanted positrons, diffusion then annihilation freely from the diffusing state. B. Thermalization, diffusion, trapping in a defect then annihilation from the trapped state. C. Back-diffusion to the surface where emission as a free positron or trapping in a surface localized state may occur.

The three main techniques of PAS can be classified into two categories according to whether they give information about electron density (PAL) or about electron

momentum distribution (DBAR and ACAR). Figure 1.2 illustrates these techniques.

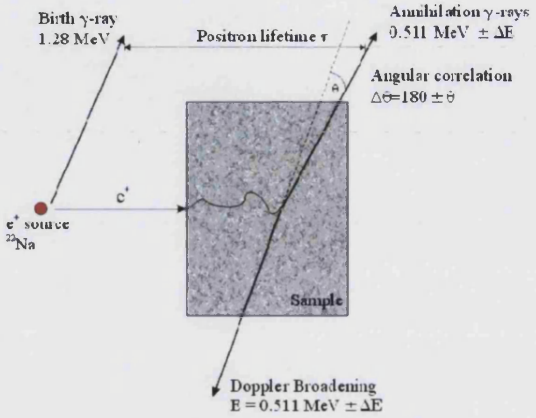

Figure 1.2 Positron annihilation experiments. Reproduced from [9].

1.5.1 Positron Lifetime Technique

Positrons injected into the sample from the most frequently used source, ^{22}Na, are accompanied almost simultaneously by 1.28MeV gamma photons. Hence, in positron lifetime measurements the 1.28MeV γ photon serves as the start signal and the 511keV annihilation γ photon as the stop signal. These photons are detected and the time interval between them is converted into an analogue pulse and lifetime spectrum is measured. Lifetime spectra usually contain a set of exponential components which are extracted by deconvoluting the spectra using an analysis code, e.g POSITRONFIT [10] to find the various lifetimes and their intensities and relate them to different defect states.

The electron density at the positron annihilation site can be directly measured using PAL, where the positron lifetime τ is the inverse of the annihilation rate λ, which in the simplest model is proportional to the electron density n_e by

$$\lambda = \pi r_o^2 c n_e \tag{1.3}$$

where r_o is the classical electron radius, and c is the speed of light.

When positrons are trapped in open-volume defects, such as vacancy, the lifetime increases due to the reduced electron density at the defect site. In general, the longer the positron lifetime, the lower the electron density at the annihilation site.

1.5.2 Momentum Distribution Techniques

DBAR and ACAR, although they are quite different from each other experimentally, are both based on the principle of momentum conservation. As mentioned earlier, the momentum of the annihilating electron-positron pair is conserved in the annihilation quanta. If both the positron and the electron are at rest at the moment of annihilation, the conservation of momentum will cause the two γ photons to be emitted collinearly into opposite directions each with an exact energy of m_oc^2. However, because of the non-zero momentum of the annihilating pairs, the annihilation photons are emitted with an energy deviation ΔE and an angular deviation $\Delta\theta$. The broadening ΔE can be determined by the Doppler broadening of the annihilation radiation spectroscopy (DBAR) and the angular deviation $\Delta\theta$ can be measured by a γ-γ coincidence arrangement known as angular correlation of annihilation radiation (ACAR).

The energy spectra measured using DBAR spectroscopy are sensitive to lattice defects. In the case of trapping of positrons in open-volume defects, such as vacancies, the fraction of valence electrons taking part in the annihilation process increases compared with that of core electrons, and because of the low momentum of those electrons only small shift will be observed in the energy of the annihilation photons. This effect is seen as a small broadening in the 511keV annihilation line in the energy spectrum. In general, the annihilation photo-peak of a defect-rich material is higher and narrower than that of a defect-free material.

The previous three experimental techniques use a radioactive source of positrons. The problem with this is that emitted positrons will have broad energy distribution, up to 0.54MeV for ^{22}Na, which leads to an uncontrollable large penetration depth. Thus these techniques can yield information on the bulk of the material, and study

of surface and near-surface regions is impossible. However, the advent of slow positron beams came to enable physicists to study thin films and depth profile materials. The idea of mono-energetic positron beams was proposed in 1950 by Madanskii and Rasetti [11] when they realized the limitations of PAS with the continuous energy distribution of positrons emitted from standard radioactive sources. Yet positron beams did not appear in laboratories for practical solid state applications until the late seventies when moderators with efficient positron reemission were used by Mills and Lynn [12,13]. The principle of positron beams is outlined in the next section.

1.6 Variable Energy Positron Annihilation Spectroscopy (VEPAS)

In VEPAS, positrons emitted from radioisotopes are moderated in order to get a mono-energetic positron beam. The most commonly used radioisotope is ^{22}Na because of its advantages in having long half-life (2.6 years) and high positron yield (~ 90%), and the most widely used material as a moderator is tungsten, W, because of its high negative positron work function (~ -3 eV) and high efficiency (~ 10^{-3}) [14].

It should be mentioned here that positrons leaving the moderator are accompanied by high-energy positrons. Thus the moderated positrons are separated from the unmoderated ones before transporting them to the target, usually by using an $\underline{E} \times \underline{B}$ filter or in some beams by a bent section in the flight tube. The moderated positrons are then accelerated to the desired energy, typically in the range of 0-30keV, and then transported to the target through a guiding magnetic field. Once hitting the sample, the positrons are rapidly thermalized (within a few ps), diffuse into the material with a mean implantation depth of up to a few μm and eventually annihilate.

As for the measurements that can be performed using positron beams, all the techniques described earlier using conventional radioactive sources can be carried out. However, because of the difficulty in obtaining the signal of positron entry into the sample and the complexity of constructing a 'timed beam', only few

beams perform positron lifetime measurements [15,16] while most of the beams in the world rely on the DBAR technique to obtain defect depth profiling. In beam-based DBAR spectroscopy, the Doppler broadening of the annihilation line caused by the non-zero electron momentum is monitored by measuring the annihilation photons' energies using a high purity Ge detector. The signal from the detector is amplified, digitized and then characterized by some parameters to get information on the annihilation sites.

1.7 Positron Depth Profiling

As stated earlier, variable-energy slow positron beams can provide a depth-profiling tool to obtain information on open volume defects in the sample, such as vacancies, voids, etc., up to depths of a few μm. The implantation profile *P(z,E)* of mono-energetic positrons with energy *E* is a Makhovian profile [17] given by;

$$P(z,E)=\frac{mz^{m-1}}{z_0^m}\exp\left[-\left(\frac{z}{z_0}\right)^m\right] \tag{1.4}$$

where z denotes the depth into the solid from the surface, m is known as a shape parameter and it is believed to be a function of both the atomic number Z of the material under study and the incident positron energy [18]. z_0 depends on the incident positron energy and is related to the mean implantation depth, $\overline{z}$, by

$$z_0=\frac{\overline{z}}{\Gamma\left(\frac{1}{m}+1\right)} \tag{1.5}$$

where Γ is the gamma function, and the mean depth, $\overline{z}$ in Å, is related to the incident positron energy by;

$$\overline{z}=\frac{\alpha}{\rho}E^n \tag{1.6}$$

where ρ is the density of the material, α and n are empirical parameters. Widely used values are $n = 1.6$, and $\alpha = 4.0$ μg cm^{-2} keV^{-n} [19].

Figure 1.3 shows the positron profile in Si for three different energies. It is clear that at lower energies the profiles are sharper and better depth resolution is achieved.

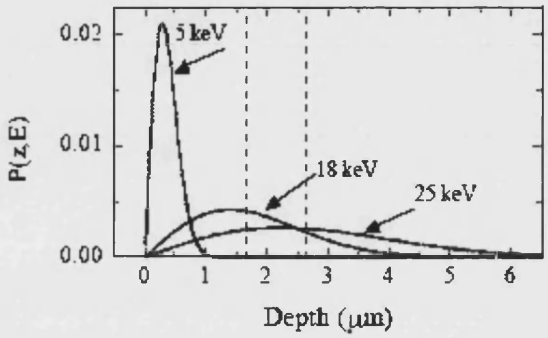

Figure 1.3 Makhov profile *P(z, E)* for positrons in Si at three incident energies, 5, 18, and 25keV.

1.8 Positron Diffusion and Trapping

The movement of thermalized positrons can be characterized, similar to holes in semiconductor, by a diffusivity D_+ and a mobility μ, which are related to each other by;

$$eD_+ = k_B T \mu \tag{1.7}$$

where k_B is Boltzmann's constant and e is the elementary charge (1.60×10^{-19} C).

The diffusion length of the positron L_+ during its lifetime τ_b in a defect free material is given by;

$$L_+ = \sqrt{D_+ \tau_b} \tag{1.8}$$

The measured values for the positron diffusivity in crystalline silicon at 300 K range from 2.7×10^{-4} m^2s^{-1} to 3.1×10^{-4} m^2s^{-1} [20,21], while the lifetime of free positrons in silicon is 217 ps [22], yields to $L_+ = 250 \pm 10$ nm.

If neutral or negatively charged open volume defects exist in the lattice, the thermalized positrons have a probability of getting trapped during their diffusion by the potential well that forms as a result of the absent repulsive ion core. Positrons are normally bound with an energy of ~1eV and then annihilates from the localized state. The effective positron diffusion length L_{eff} is given by;

$$L_{eff} = \sqrt{\frac{D_+}{\lambda_b + \kappa}} \tag{1.9}$$

where λ_b is the positron annihilation rate in bulk material, and κ is the positron trapping rate.

The rate of positron trapping into different kinds of open volume defects can be modelled by two different approaches, namely diffusion limited trapping and transition limit trapping. Diffusion limited trapping is applicable for positron-trapping centres having a large trapping cross section (e.g., voids) and thus the trapping rate is dominantly determined by positron diffusion to the defects rather than by their transition to the bound state related to the defects. In either case, however, the trapping rate κ is proportional to the defect concentration C_d [23], $\kappa = \nu C_d$ or $\kappa = 4\pi r D_+ C_d$ for the transition-limited trapping or diffusion-limited trapping respectively. ν is the specific positron trapping rate for a certain defect, and r is the radius of the defect.

1.9 Applications of Positron Annihilation Spectroscopy

Ever since the discovery of the positron over 70 years ago, physicists have attempted to explore more about this new discovery. Then after the realization of

the non-collinearity of the two γ-quanta arising from the annihilation of a positron and an electron pair by DeBenedetti and co-workers [24] a new field, positron physics, was born and positron physicists have contributed to its rapid growth.

Now, PAS is considered as one of the most effective methods for studying the microstructure and the electronic structure of matter. This is because of its unique properties, where it is a non-destructive probe because valuable information is provided about the material just by the detection of the annihilation radiation.

As a result of these incomparable characteristics, PAS has a wide range of applications in atomic and condensed matter physics, chemistry, biology, medicine and industry. The main areas of PAS applications in condensed matter physics and materials science are:

i. Electronic structure. Here PAS yields important information on electron momentum distribution and Fermi surface in metals and alloys [25,26].
ii. Defect studies. PAS is widely used in the studies of lattice defects due to the ability of positrons to trap or localize in open-volume defects, such as vacancies, voids, dislocations, etc., and eventually annihilate with annihilation parameters that are sensitive to the lattice imperfections. This phenomenon of positron trapping in defects was first demonstrated by Mackenzie and co-workers in 1967 [27].

Chapter 2

Open-Volume Defects in Semiconductors

2.1 Introduction

The study of defects in semiconductors has never been independent of the development of semiconductor technology. With the rapid progress in semiconductor device industry, novel types of defects and new subjects in the basic study of defects have often arisen. Great progress in device production technology has always been achieved on the basis of the knowledge obtained in basic studies.

The present chapter presents an array of subjects, ranging from the basic aspects of ion implantation, the well-established doping technique in device fabrication, to an overview of the defects induced by implantation and their role in some important phenomena related to device production engineering. Among these practically vital phenomena is the transient-enhanced diffusion (TED) of boron and impurity gettering in silicon.

2.2 Ion Implantation

Most of the samples used in the studies carried out in this thesis were implanted, for different purposes, with a variety of ions at different energies and doses. Hence, the

rest of this section will give a brief description of the ion implantation process and the type of defects induced by this process.

In ion implantation, dopant atoms are injected into a crystal by accelerating the atoms to a high velocity and implanting them into the solid. This process is routinely used in device fabrication to introduce precisely controlled quantities of dopant atoms into specified regions of a semiconductor wafer, principally to change the electrical properties of the substrate. Selection of dopants' concentration and depth profile is possible by choosing the appropriate ion mass, dose and energy. Typical ion energies are between 30 and 300keV, and typical doses vary from 10^{11} to 10^{16} ions/cm^2 [28].

A schematic diagram of a typical ion implantation system is shown in figure 2.1. In the ion source, the atoms of the dopants are ionized and a fine beam is extracted then analyzed by a magnet which has a field chosen so that only ions with the desired charge to mass ratio can pass through to the accelerator where they are accelerated to the required implantation energy. The accelerated ions are then passed through vertical and horizontal scanners and then implanted into the sample.

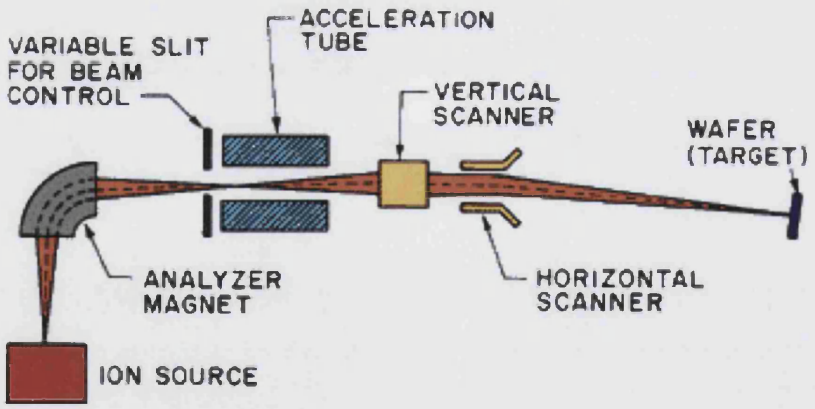

Figure 2.1 Schematic of a typical ion implantation system [28].

2.2.1 Distribution and Range of Implanted Ions

When energetic ions enter the material they lose their energy through collisions with the target atoms until they finally come to rest. The total distance an ion travels in coming to rest is called the *range R*, and the projection of this distance along the axis of the ion incidence is called the *projected range* R_p. Those two ranges are illustrated in figure 2.2. As the number of collisions per unit distance and the energy lost per collision are random variables, there will be a spatial distribution of ions having the same mass and the same initial energy. The statistical fluctuation in the projected range is called the *projected straggle* ΔR_p, whereas the fluctuation along the axis perpendicular to the incidence axis is known as the *lateral straggle* $\Delta R_\perp$.

The profile of the implanted ions along the incidence axis can be approximated by a Gaussian distribution function [28];

$$n(x) = \frac{S}{\sqrt{2\pi}\Delta R_P} \exp\left[-\frac{(x-R_P)^2}{2\Delta R_P^2}\right] \tag{2.1}$$

where S is the ion dose per unit area.

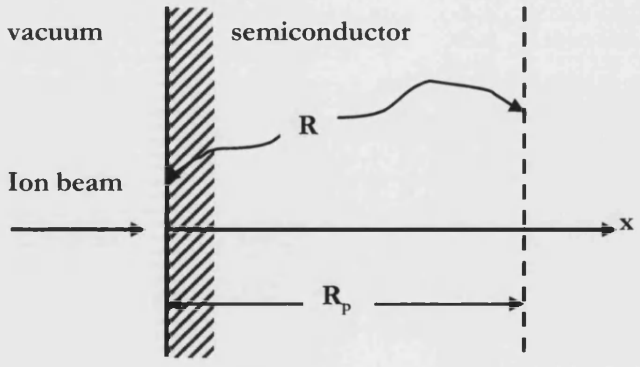

Figure 2.2 Schematic of the ion range *R* and projected range R_P. Reproduced from [28].

2.2.2 Implantation Damage

As stated previously, when energetic ions enter a substrate, they slow down and their kinetic energy is dissipated to electronic excitation and to elastic atomic or nuclear collisions until they finally come to rest. Nuclear collisions are responsible for atomic displacements of the atoms from their lattice sites. The displaced atoms can in turn cause cascades displacements in the lattice if they have enough energy, producing damage or lattice disorder [29]. Thus ion implantation, besides introducing foreign atoms, creates lattice defects in the material.

The depth distribution of the implanted ions and the profile of the generated defects can be simulated using a Monte Carlo code, TRIM (transport of ions in matter) [30]. Figure 2.3 shows the simulation of 100keV B^+ ions implanted in Si. It can be seen that the distribution of the ions is approximately a Gaussian profile while the damage distribution has a peak-like shape extending with a tail towards the surface. It should be mentioned here that TRIM simulation of the defects produced by ion implantation is not so accurate as it does not consider defects-impurities interaction or vacancies-interstitials recombination that occur with increasing the temperature.

Because of the damage and lattice disorder resulting from ion implantation, material's parameters such as mobility are severely degraded. In addition, most of implanted ions are not incorporated in the lattice, i.e. are not electrically active. Hence, annealing to an appropriate temperature and time is usually carried out in order to activate the implanted ions and to restore mobility, crystallinity and other material's parameters. Rapid thermal annealing (RTA) is usually applied for short times to activate the dopants.

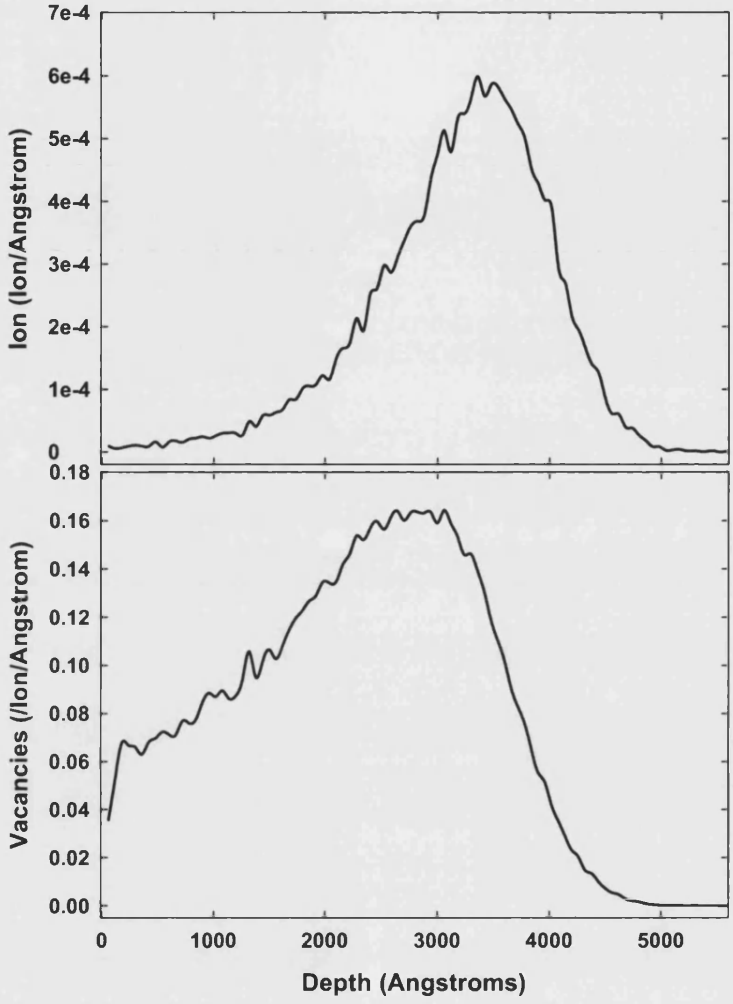

Figure 2.3 Simulation of (a) the distribution of 100keV B^+ ions implanted in Si and (b) the produced vacancy profile, obtained using TRIM code.

Defects appearing in semiconductors after ion implantation has been extensively studied, with special interest in the microscopic description of those emerging in Si. Of the many type of defects identified in ion-implanted materials, vacancies, their clusters and complexes, are singled out here for particular attention. A brief review of some studies performed to investigate these ion-implantation-associated defects will be given in the next section.

2.3 Ion-Implantation-Induced Defects

A commonly-used method for the characterization of ion-implanted materials is Rutherford backscattering (RBS). It is sensitive to interstitial and lattice distortions but not to vacancy-type defects [9]. However, PAS as a well-known excellent probe for a large variety of defects provides a powerful complementary method for studying such open-volume defects induced by ion implantation. Extensive studies have been performed on investigating defects after implantation with a range of ions starting from H^+ to heavy ions and their subsequent evolution. The first papers describing the application of PAS to defects caused by ion implantation appeared in mid 1980's [9]. Since that time, an extensive number of studies on defects induced by ion implantation in semiconductors has been performed with a main aim of deriving depth profile of the induced defects. One of the studies using VEPAS is the work carried out by Hautojärvi et al. [31]. In their study, vacancy-type defects induced by implantation with 50keV BF_2 have been observed up to 100nm with a mean depth close to the peak of the implanted ions profile. Because of the broad depth distribution of the incident mono-energetic positrons, the real defect profile cannot be unambiguously obtained in positron studies. Hence, a certain defect profile is usually assumed, e.g. a block profile, in order to fit the measured data and determine the damage depth and the defect concentration.

2.3.1 Vacancies

Vacancies are the simplest and most important traps of positrons in semiconductors. They are known to occur at pronounced concentrations after irradiation with high energetic particles (electrons, neutrons, ions, etc.). Positron annihilation parameters, e.g. the positron lifetime and the lineshape *S* parameter, change when positrons get trapped in a vacancy. The trapping process is based on an attractive potential for the positrons originating from the missing repulsing force of the absent atoms.

Vacancies usually introduce energy levels deep in the band gap which have influence on the electrical properties of the material. Vacancy-type defects can exhibit different charge states in semiconductors, for instance, divacancies (V_2), the most fundamental type of vacancies, can appear in four different charge states; positive (V^+), neutral (V^0), negative (V^-), and double negative (V^{-2}) [32]. The energy levels of those various charge states of V_2 in the bandgap of silicon are shown in figure 2.4. The levels of the different charge states of monovacancies, vacancy-phosphorus (*E* centres), and vacancy-oxygen (*A* centres) are also shown in the figure.

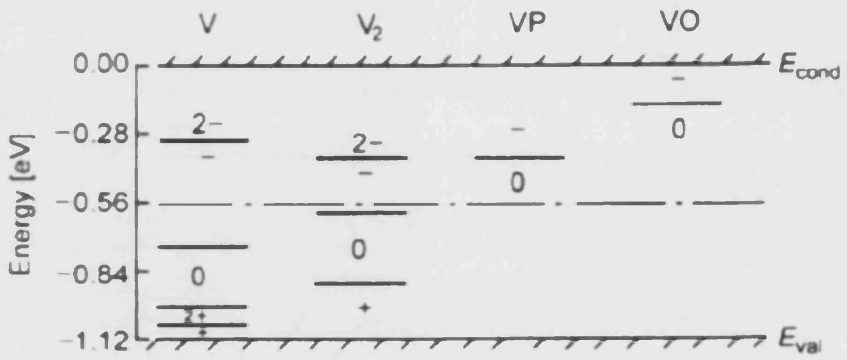

Figure 2.4 Energy level scheme for the various charge states of monovacancies, divacancies, vacancy-phosphorus pairs (*E* centres), and vacancy-oxygen pairs (*A* centres) in the bandgap of Si. E_{val} and E_{cond} are the edges of the valence and conduction bands, respectively [9].

At room temperature and up to ~200°C, V_2 are known to be immobile; however, it has been found in an early EPR study by Watkins and Corbett [32] that beyond this temperature V_2 can migrate with a thermal activation energy (E_a) of ≈ 1.3eV. During their migration, V_2 can interact with impurities in the lattice forming complexes. Oxygen (O) atoms, in particular, are thought to be effective traps for V_2 and V_2-O interactions have been suggested to be the main mechanism of V_2 elimination upon annealing in Cz-grown Si [32-34]. VO complexes have been also observed in Si and it is believed that they, together with V_2, are the most prominent type of vacancy-related defects after ion implantation at RT (e.g. [35]).

2.3.2 Vacancy complexes

As said in the above paragraph, vacancies could undergo interaction with interstitial and impurity atoms, especially O, forming vacancy complexes. Divacancy-oxygen (V_2O) complexes are the most basic form of vacancy-oxygen complexes that can be formed in Si after room-temperature ion implantation. Signals associated with V_2 annealing and V_2O formation have been identified in a study using deep level transient spectroscopy (DLTS) [36]. It is believed that V_2O are to a large extent involved in the mechanisms of impurity-assisted annealing of V_2 in Si [36,37]. This could explain the high stability of V_2 in float-zone (FZ) Si compared to Czochralski (Cz) Si. It is suggested that two competing mechanisms for the annealing of V_2 exist, namely direct dissociation (with activation energy of ~1.6eV) or migration with impurities (with ~1.3eV activation energy). Since FZ-Si contains relatively small amounts of impurities, V_2 are stable up to the temperature of dissociation. In contrast, in Cz-Si with relatively high concentrations of impurities, most of V_2 are annealed away by the migration mechanism and perhaps form V_2O complexes [38,39].

Several types of vacancy-oxygen complexes showing different annealing behaviour have been detected by Uedono et al. using positrons [40]. In another PAS study of oxygen-implanted Si, multivacancy-oxygen complexes have been observed [41] and annealing to ~600°C was found to cause transformation of those clusters into multivacancy-multioxygen ones. Vacancy-impurity complexes were also observed beside V_2 in self-implanted Si samples [42].

Other vacancy complexes, such as fluorine-vacancy (FV) complexes, have been also detected in Si. FV complexes induced by fluorine implantation have been the target of various studies aiming for understanding their effect on the boron TED in Si (e.g. [43,44])

2.3.3 Vacancy clusters

Vacancies can also agglomerate with each other forming clusters or voids. According to theoretical calculations [45], the agglomeration of vacancies leads to an increase in positron trapping coefficient. For i ($i \leq 5$) vacancies forming the vacancy cluster, the specific positron trapping coefficient of the cluster ν_{iv} is usually assumed to be proportional to i,

$$\nu_{iv} = i\nu_v \tag{2.2}$$

Where ν_v is the specific trapping coefficient of a monovacancy.

A distinct change in the positron annihilation parameters is expected during agglomeration of vacancies into clusters. The positron lifetime as well as the lineshape S parameter would increase significantly.

Clustering of V_2 was observed by Fujinami et al. [46] and Nielsen et al. [47] with annealing in the range between 200 and 300°C, while further annealing up to 675°C was found to be necessary to remove those clusters [46,47]. Clustering of implantation-induced vacancies to larger clusters was also observed in various studies [48,49]. Clusters of the size of hexavacancies (V_6) were found in 2 MeV self-implanted Si upon annealing to high temperatures (~600°C) [50].

V_6 with a closed-ring structure have been theoretically proposed to have significantly more stability than other types of vacancy clusters [51]. Further calculations have concluded that smaller clusters could have the most stable configurations when vacancies are removed by atoms going into the V_6 ring rather than being removed from it [52]. This is because V_6 are known to be efficient traps for various impurities [53] and therefore they are expected to be good traps for interstitials as well. Hence,

penta-, tetra-, and trivacancies could be formed by combination of hexavacancies with one, two, or three interstitials, respectively.

2.4 Applications of Ion-implanted induced Vacancy-type Defects

Although the term defects implies a deleterious effect on the material, and thus that they should be removed, it is known that some vacancy-type defects are vital in materials processing, especially semiconducting materials because of their importance in the microelectronics industry. Defects introduced by ion implantation are of great significance in such device manufacturing where they can be controlled in a specific way to provide the desired properties of the materials.

An example of the technological importance of defects is their role in TED of dopants, especially B. On one hand, it is well-known that upon annealing at elevated temperatures the implantation-induced defects will interact with the dopants and will cause TED. This results in changes of the junction depth and hence lead to degradation of the performance of the devices. On the other hand, further implantation of such devices with other implants, e.g. F, is a cure for the problem where it would result in retarding or even suppressing the TED. Numerous works have concentrated on the phenomenon of B TED and the role of F in retarding TED to face the device miniaturization challenge [43,44,54]. It has been proposed that FV complexes are formed after ion implantation and they have significant effect on reducing B TED by acting as traps for interstitials released from the end-of-range (EOR) of the defects which are responsible for TED.

Another example of the usefulness of vacancy-type defects generated by ion implantation is their use in impurity gettering in Si. Here, as a consequence of MeV implantation and subsequent annealing of the wafer, a distinct layer of vacancy-type defects is formed and acts as an efficient trap for unwanted metal impurities, such as

Fe and Cu, and therefore removes them from the active region of the wafer [55,56]. High-energy ion implantation is also used for providing a quantitative profile of defects in Si by Au labelling [57].

Therefore, it is clear that the study of defects following ion implantation is of great importance for understanding their interactions with dopants and impurities and hence obtain the knowledge required to make use of them. Indeed, open-volume defects play a critical role in many other aspects of front-end processing such as silicon-on-insulator (SOI) structures, which provide the basis of ultra-large-scale integration (ULSI) device manufacturing. One technique used for fabricating high quality SOI structures is the Smart-Cut technology [58]. In this method, implantation of Si crystal with high doses of H^+ ions followed by annealing is performed, resulting in wafer separation by a layer of microvoids formed during the process.

Implantation induced defects have further applications in compound semiconductors devices. They are used to improve the performance of heterostructure bipolar transistors (HBT) and improve the properties of GaN for generating blue LEDs and lasers [55]. In all these applications the role of vacancies cannot be ignored.

Chapter 3

Positron Beam System and Data Analysis

In this chapter a general description will be given for the University of Bath positron beam system which has been used in performing the measurements carried out in this thesis. The parameters used in analysing the data and the fitting program will also be introduced.

3.1 Introduction

A photograph of the writer with the University of Bath slow positron beam is shown in figure 3.1 and a schematic drawing for the beam is presented in figure 3.2. Positrons are emitted from a ^{22}Na source, moderated using a tungsten mesh, then accelerated and guided by six Helmholtz coils towards the sample chamber where they annihilate. The annihilation events are detected by a High Purity Ge (HPGe) detector and recorded on a Multi-Channel Analyser (MCA). A detailed description of the beam can be found in [59].

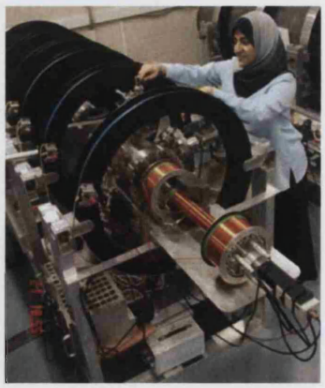

Figure 3.1 Photograph of the writer with the University of Bath positron beam.

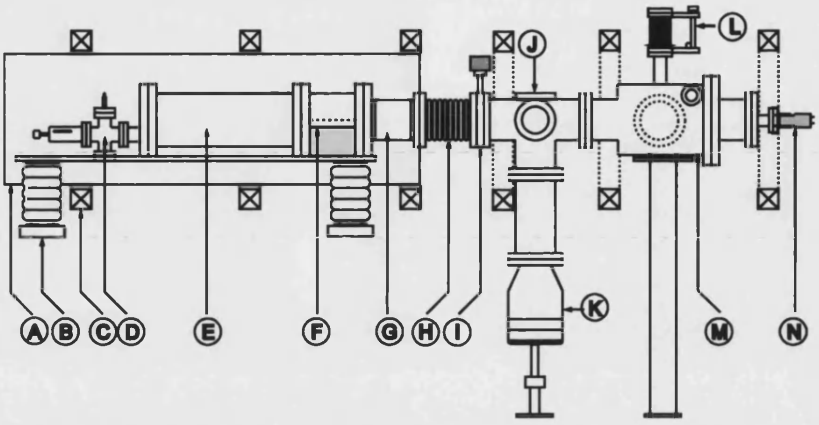

Figure 3.2 Schematic drawing for the University of Bath slow positron beam. (A) earthed shield, (B) Ceramic high-voltage insulator, (C) Coils for magnetic field, (D) source/moderator assembly, (E) *ExB* plates, (F) slow positron transport tube, (G) 0-30 keV accelerator, (H) bellows, (I) gate valve, (J) fine control coils, (K) turbo-molecular pump, (L) sample manipulator, (M) sample chamber with re-entrant port for Ge detector, (N) CEMA/phosphor detector assembly [59].

3.2 General Description of the Beam

3.2.1 Positron Source and Moderator

The positron source, mounted on a linear drive and positioned in vacuum in the source/moderator chamber, is a ^{22}Na β^+ emitter source with a half life of ~ 2.6 years and initial activity of 50mCi (1.85GBq). As mentioned in chapter 1, positrons emitted from this source have a broad energy distribution up to 0.54 MeV, which leads to a relatively high penetration depths, making them unsuitable for surface and near-surface studies. Hence the emitted positrons are decelerated to a few eV using a tungsten mesh moderator which is placed 1 mm in front of the source window and at a potential of 10 V less than that of the source. An *in-situ* annealing of the moderator is occasionally performed to maintain its efficiency and it is carried out by passing a current through the mesh for about 30 seconds, heating to a temperature close to 2000°C.

3.2.2 Beam Filtering

After passing through the tungsten moderator, a beam consists of both moderated slow positrons and some fast positrons, which have emerged through the mesh without moderation, will be produced. Hence, the beam is filtered by passing through two parallel E×B velocity filters, whose parallel plates produce an electrostatic field that is perpendicular to that of the axial magnetic field and can remove the fast positrons from the beam.

3.2.3 Positron Acceleration and Transportation

The slow positrons are then transported by a uniform magnetic field of 1×10^{-2} T provided by six coils wounded with 2 mm diameter insulated copper wire. The current required to pass through the coils to provide this field is 5 A.

The positrons are then accelerated to the required energy of up to 30 keV. The acceleration is achieved by creating a uniform potential gradient using an accelerator which consists of a set of ten metal discs separated by 40 MΩ resistors.

3.2.4 Sample Holder and Beam Alignment

The sample can be moved by a manipulator mounted on top of the sample chamber. The manipulator allows the sample to be correctly placed in the chamber and allows multiple samples to be mounted on the holder at the same time.

Beam alignment can be checked using a Channel Electron Multiplier Array (CEMA) coupled with a phosphor screen. This CEMA/phosphor assembly provides a method for positioning the beam at a desired position by enabling one to 'see' the positrons, using a CCD TV camera, as the electrons leaving the CEMA strike the phosphor screen.

3.3 Beam Control and Data Acquisition

3.3.1 Electronics

A typical DBAR system using a variable energy positron beam is sketched in figure 3.3. The Doppler broadening of the annihilation line caused by the non-zero electron momentum is monitored by measuring the annihilation photons' energies using a high purity Ge detector. The signal from the detector is amplified, digitized using an Analogue-to-Digital Converter (ADC), and then sent, after being stabilised, to a Multi-Channel Analyser (MCA) board on a computer.

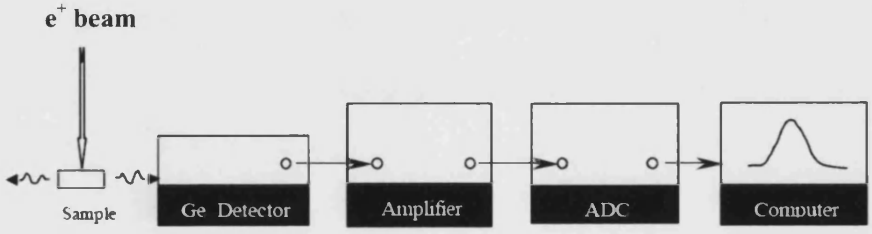

Figure 3.3 Schematic diagram of beam-based Doppler broadening spectrometer.

3.3.2 Control Program

The positron beam control and the data acquisition are performed using a program written in Visual basic. With this program the position and the energy of the beam can be controlled by varying the accelerating voltage and the voltages on the horizontal and vertical magnetic coils. The program also controls the MCA for collecting, storing the data and making some necessary calculations.

The basic operating principle of beam-based Doppler-broadening spectroscopy is increasing the positron beam energy and collecting the gamma energy spectrum at each energy. This can be done using the control program where it is fed with a setup file with the required energies and accelerating voltages as well as beam position at each energy. The collected spectra are then analysed and the annihilation lines are characterised by calculating some parameters as it will be described in the next section.

3.4 Data Analysis

A typical annihilation spectrum as obtained from the MCA is shown in figure 3.4. The higher energy peak is due to the 1.28MeV photons emitted from ^{22}Na nearly simultaneously with the positron birth and is greatly reduced in intensity in a positron beam system, where the detector is far away from the source. The lower peak results from the 511keV photons emitted in the two-photon annihilation process. The three photon annihilations are counted at lower energies in Compton region. The region which contains the 511keV peak is the important region for calculating the Doppler broadening parameters.

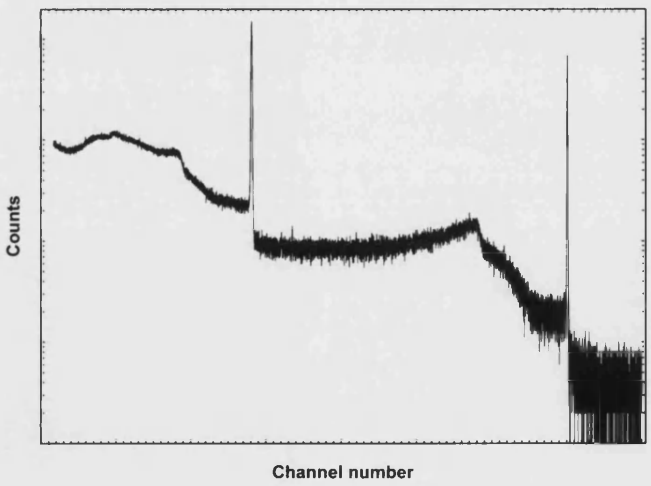

Figure 3.4 A typical annihilation spectrum of ^{22}Na obtained using a HPGe detector. Note that the vertical scale is logarithmic.

3.4.1 The Lineshape Parameters

3.4.1.1 *S* Parameter

The Doppler broadening of the annihilation line is determined by calculating a parameter called the *S* (sharpness) parameter. The *S* parameter was introduced by Mackenzie et al. in 1970 [60], and it is defined as the ratio of the number of counts in a defined area under the peak centroid to the total number of counts of the area under the entire peak.

Figure 3.5 shows the 511keV peak divided up into three regions. If A_c is the peak centroid area, A_l and A_r are chosen areas in the left and the right wings of the peak, and A is the total area under the peak, then S can be expressed mathematically as;

$$S = \frac{A_c}{A} \tag{3.1}$$

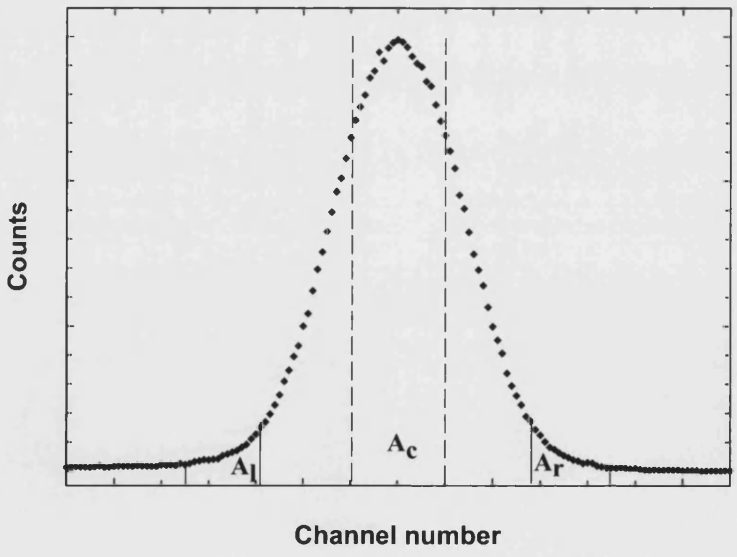

Figure 3.5 The 511keV annihilation peak with the regions used in defining the lineshape parameters.

If various modes of annihilation occur with different characteristic S parameter, then the observed S will be a linear combination of the value of each mode.

The S parameter is sensitive to changes in the lineshape width; its value decreases as the peak becomes wider, which is reflecting changes in the momentum of the electrons annihilating with trapped positrons; the higher their momentum, the broader the 511keV peak and hence the lower the value of the S parameter.

3.4.1.2 W Parameter

Another parameter used for describing the annihilation line is the W (wing) parameter, which is defined as the sum of the two symmetrical wings in the low and high energy sides of the annihilation peak over the total area of the peak;

$$W = \frac{A_l + A_r}{A} \tag{3.2}$$

It is clear that if the peak broadens, the S parameter will decrease and the W parameter will increase, and vice-versa.

The S parameter is sensitive to momentum of the valence electrons annihilating with the trapped positrons, while W is sensitive to core electron annihilation and thus to the chemical environment at which positrons annihilate.

3.4.2 The Relation between the Lineshape Parameters and Material Properties

Free or untrapped positrons can annihilate with both core and valence electrons, whereas positrons trapped in vacancies are more likely to annihilate with valence electrons, which have lower momentum, because their wave function will have small overlap with core electrons. Relating this to Doppler broadening, annihilation with low-momentum valance electrons led to small broadening and

hence narrower annihilation peak which means higher S parameter, while annihilations with high-momentum core electrons results in a broader peak or a lower S parameter value. Thus, in general, a high value of S signals the presence of open-volume defects, whereas a defect-free sample will show a low value of the S parameter.

It should be noted here that the absolute value of S and W parameters have no physical meaning since they depend on the chosen limits for their determination, which is different in different experimental arrangements. Thus, the two parameters are usually normalized to reference values (as it will be seen in all the graphs presented in chapters 4-6), corresponding to the defect-free values of the material under study, in order to obtain the relative change in their values which conveys information about the annihilation sites.

3.4.3 *S-W* Plots

Both S and W parameters are sensitive to the type of the defect in the material under study. The combination of the two parameters graphically in the so called *S-W* plots can be used in identifying the different annihilation sites in the sample as well as the type of any defect present in the material [9,61]. That is by studying the linearity between the two parameters; if there is only a single type of defect in the sample, S and W depend linearly on each other and a straight line will be obtained between the distinct annihilation sites, for example the surface and the vacancy sites or the bulk and the vacancy sites, on the other hand, if a number of defects are present then special points corresponding to the predominant annihilation sites will be distinguished with straight lines connecting these dominant points. Examples of *S-W* plots will be seen in chapter 4.

3.5 Defect Concentration

The measured S parameter can be used to calculate the concentration of defects C_d (per atom) as follows,

$$F_d = \frac{\nu C_d}{\lambda_b + \nu C_d} \tag{3.3}$$

where ν and λ_b are the positron trapping rate in defect and the annihilation rate in bulk material respectively. F_d is the fraction of positrons that become trapped in defect sites and in the case of the presence of one defect type it can be determined from;

$$S = F_d S_d + (1 - F_d) S_b \tag{3.4}$$

where S_d and S_b are the characteristic S parameter in the defect site and in the bulk respectively.

In some cases the value of S is saturated, which means that all the implanted positrons have been annihilated at defects and there is no change in S anymore even if the defect concentration continues to increase. Here the defect concentration can be obtained using the value of the effective positron diffusion length (L_{eff}) in defect site;

$$C_d = \frac{\lambda_b}{\nu}\left[\left(\frac{L_+}{L_{eff}}\right)^2 - 1\right] \tag{3.5}$$

where L_+ is the diffusion length of positrons in defect-free material.

3.6 Fitting of Data

The values observed for S and W may be approximated as resulting from positrons annihilating in a number of damaged blocks (regions). That is;

$$X(E) = \sum_{i=1}^{N} F_i(E) X_i \tag{3.6}$$

where X can either refer to S or W, and X_i are the values of S and W for each block (normally, surface, defected layer, and bulk). $F_i(E)$ are the fraction of positrons annihilating in each block. Computer codes such as VEPFIT [62] have been developed to extract X_i from the $X(E)$ spectrum.

VEPFIT is based on solving the one-dimensional diffusion model of positrons which is expressed by;

$$D_+ \frac{d^2 n(z)}{dz^2} - \kappa_{eff}\, n(z) + \mathrm{P}(z, E) = 0 \tag{3.7}$$

where D_+ is the diffusion coefficient of positrons, $n(z)$ is the probability density of positrons at a distance z from the surface, κ_{eff} is the effective escape rate of positrons from the diffusion process, and $P(z, E)$ is the implantation profile of positrons with energy E at a certain depth z. κ_{eff} is related to the lifetime of positron annihilated in defect free state τ_f by $\kappa_{eff} = 1/\tau_f$. The relationship between the diffusion length of positrons L_+ and κ_{eff} is given by

$$L_+ = \sqrt{D_+ / \kappa_{eff}} \tag{3.8}$$

$P(z, E)$ is expressed by the so-called Makhovian distribution as in (1.4) formula. Using equations (3.7) and (1.4), the fraction of positrons diffusing in each block $F_i(X)$ can be calculated and VEPFIT fits the measured $X(E)$ curves to (3.6) attempting to find an optimum fit in order to extract $X_i(E)$ as well as L_+ in each block.

Experimental data is needed to be fed into VEPFIT and a suitable fitting model should be selected in order to enable VEPFIT to perform the fitting process. The fitting models can either be a Gaussian distribution of defects or a simple layered structure with a constant defect concentration in each layer. Example of fitting an

S(E) curve for a Si sample implanted with 2MeV Si^+ ions and annealed at 600°C for 30 min assuming a structure of four layers, surface, two different defected layers and bulk, is shown in figure 3.6.

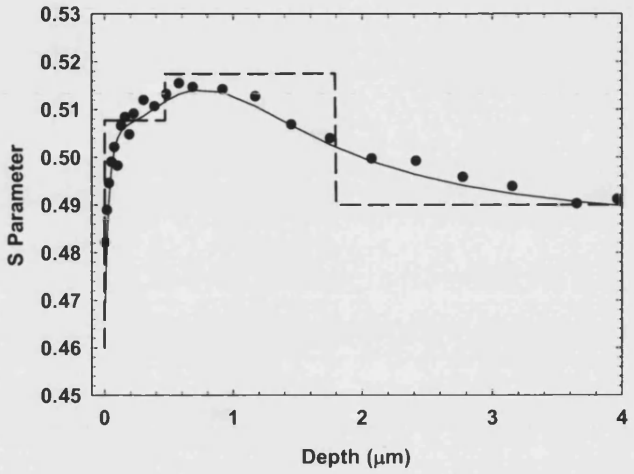

Figure 3.6 S parameter versus implantation depth for Si sample implanted with 2MeV Si^+ ions and annealed at 600°C for 30min. fitting of the curve was obtained by VEPFIT assuming a four layer structure model. The solid line is the best fit achieved using this model.

It should be mentioned here that in order to get reliable output from VEPFIT, careful application is required, with the need to provide all the known parameters in the input file to start fitting with a minimum number of free parameters. One should also check, whenever possible, for internal consistency of the fitted parameters – for example, *S* parameter and diffusion length are linked in layers uniformly filled with one type of defect.

Chapter 4

Evolution of Vacancy-type Defects in Si and SiGe

In this chapter, studies on the evolution of vacancy-like defects in various systems are reported. The first section summarizes and compares the annealing behaviour of defects introduced by low-energy self-implantation in Czochralski (Cz)- and epitaxial (epi)-grown Si wafers, while the second section concentrates on the behaviour of defects generated in high-energy self-implanted Cz-Si. Simple method for estimating room-temperature (RT) diffusion of vacancy-like defects in Si is described in section 3. A flavour of the annealing mechanism of open-volume defects in Si-Ge upon thermal oxidation in different ambient is given in the last section.

4.1 Evolution of Near-surface Vacancy-type Defects in Cz- and epi-Si

The evolution of implantation-induced, near-surface, vacancy-type defects has been investigated in this study. Vacancy-like defects were introduced by 50keV Si^+ ions at $5x10^{13}$ cm^{-2} in Cz- and epi-grown Si wafers, and their evolution was monitored by measuring at-temperature positron response using VEPAS. Obtained results suggest that annealing at low-temperatures (300-500°C) causes migration and as a result clustering of the implantation-induced vacancies with activation energies of ~2eV in epi and ~2.7eV in Cz, while annealing at higher temperatures (>500-640°C) rapidly

anneals those clusters away with activation energies of ~3.3 and 4eV in Cz and epi, respectively. Difference between the two types of Si has been observed in the annealing rate of the defects; faster in Cz especially in the low temperature range, which is probably due to the presence of impurities in this type enhancing the clustering process.

4.1.1. Introduction

Ion implantation, as a fundamental tool in Si microelectronic technology, motivates a continuing interest in studying defects associated with its subsequent damage, due to their significant importance in device performance. Divacancies (V_2) are well-known as the dominant type of defects formed during room temperature ion implantation; probably as a consequence of the recombination of monovacancies, which are mobile at room temperature. However, at temperatures in the range between ~125 and 350°C, various studies using electron paramagnetic resonance (EPR) [32], deep-level transient spectroscopy (DLTS) [35], and infrared spectroscopy (IR) [49,63] have shown disappearance of V_2 with a well-established migration energy of ~1.3eV. On the other hand, agglomeration of V_2 forming vacancy clusters is likely to occur upon annealing at higher temperatures. Such vacancy clusters have been detected by PAS in several studies (for example [48-50,63]) and their formation has been proposed as one of the annealing mechanisms of V_2 [48].

The evolution of ion implantation induced defects upon thermal annealing has been the target of several studies. Various systems have been investigated using a wide range of defect characterisation techniques. The rest of this introduction is a review of examples of those studies. The author has studied 2 MeV self-implanted Cz Si using variable-energy PAS (reported below in section 4.2). Agglomeration of the implantation-induced defects has been observed upon annealing at high temperatures (600°C) forming clusters of the size of hexavacancies, and then annealing away or break up of the clusters with annealing for longer times at 600°C or at higher temperatures [50]. Si^+ ions at energies of 0.54, 3 and 5 MeV implanted in float-zone

(FZ) Si samples has been examined in an early work by Simpson and co workers [49]. In their study, using PAS and IR, the positron response to the defects was constant up to ~600°C; in contrast, IR measurements showed that 300°C is sufficient to remove the 1.8μm absorption peak associated with V_2. This discrepancy between IR and PAS measurements was explained to be due to vacancy aggregation, thereby vacancy agglomerates are formed at the temperature at which V_2 become mobile, and those agglomerates are positron detectable but no longer optically active. The binding energy of vacancies to vacancy clusters formed upon annealing in Si implanted with MeV Si^+ is believed to be high but their formation energy is low as they are formed quickly at low temperatures but last for long times or to high temperatures. A value of 3.2±0.2eV has been reported by Kalyanaraman et al. for the binding energy of vacancy clusters in a 1.8μm thick Si top layer of Si-on-insulator structure implanted with 2MeV Si^+ ions and annealed at temperatures between 800 and 900°C [64].

In a work employing positronium formation spectroscopy to monitor the annealing behaviour of near-surface (within ~100 nm below the surface) defects induced by 50keV and $5x10^{13}$ Si^+/cm^2 in FZ Si, Coleman, Malik and Knights have found that there is only one major annealing step at 550±50°C, and it is believed to be the annealing temperature of divacancies-impurity complexes as it is higher than the reported value for divacancies [65]. In another study of near-surface defects induced by 100keV self-implantation of Cz-Si, using PAS and Rutherford backscattering spectroscopy (RBS), evidence of a strong dependence of defect annealing behaviour on the implantation dose has been shown. It was found that if the dose is below the critical value of amorphization ($2\text{-}3x10^{14}$ cm^{-2}), implantation-induced divacancies form clusters by annealing at 300°C which are stable up to 500°C but anneal out at ~800°C. On the other hand, when the implantation dose is higher than the amorphization value, two steps have been noticed; transformation of the amorphous zone into crystalline at 600°C followed by vacancy cluster formation at higher temperatures and then cluster annealing stage at 900°C [46].

Annealing of defects introduced into Si by implantation of other (than Si) ions has been also investigated. Examples include implantation with lighter than Si ions like F^+ and O^+. In both cases, vacancy clustering forming FV or OV has been observed upon annealing to high temperatures (600-800°C) (for example, [66,67]). Implantation of Cz and Fz Si with B^+ ions has also been examined by means of different techniques. IR showed relatively constant concentration of V_2 in all samples, whereas PAS showed an increase in the defect characteristic parameters [63]. The authors of ref. [63] concluded that vacancy clusters of three or four vacancies must exist in the samples beside divacancies, and their assumption was supported by the thermal stability of those defects up to ~450°C, which can not be the case for divacancies as they are well-known to anneal out at ~200°C [63]. Implantation with heavier ions has also been considered. As an example of this, Dannefaer and co-workers study of Fz-Si implanted with 245MeV Kr^+ ions [48]. The introduced damage was found to be mainly in the form of four-vacancy clusters with only small fraction of divacancies. Isothermal annealing at various temperatures between 125 and 500°C exhibited an initial fast decrease in V_2 concentration followed by a slow process of vacancy agglomeration. In Cz-grown samples, no initial decrease in V_2 concentration or vacancy agglomeration was observed; however, vacancy-dopant complexes, acquiring oxygen impurities as annealing progressed, have shown to be formed and survive annealing at 500°C for many hours.

Dannefaer and co-workers have also studied the annealing mechanisms of vacancies produced by proton and electron irradiation. Measurements of 8MeV proton-irradiated FZ samples using EPR, Fourier transform IR and PAS have given evidence of a divacancy annealing stage at 160°C. Nevertheless, a discrepancy between IR and PAS has arisen again at 250°C where IR shows a rapid decrease of the 1.8μm absorption band intensity but the PAS response remains constant. An increase of the positron lifetime and decrease of the positron trapping rate have been noticed above 500°C, indicating clustering of the divacancy-like defects and decreasing of their concentration, and complete annealing has been shown after 30 min at 575°C. This disagreement between IR and PAS was explained as a result of divacancies

associating with each other without yet forming larger defects, therefore, not having a significant effect on positrons, but because of the perturbation in the electronic structure of the defects, the 1.8μm absorption band is removed [48,68]. For FZ samples irradiated with 10MeV electrons, PAS measurements have confirmed that annealing above 515°C is necessary for the formation of vacancy clusters, following an intermediate step of loose vacancy complexes created upon lower temperature annealing between 150 and 300°C. A discrepancy between IR and positron results has been seen here also, where the 1.8μm absorption band disappears upon annealing above 150°C, indicating annealing of V_2, while the positron lifetime stays constant to up to ~515°C and did not increase with annealing above 150°C, as would expected following vacancy agglomeration. Furthermore, the lineshape parameter decreases rather than increases. This was explained in the study by the formation of 'loose' clusters, i.e. not complete coalesced vacancies, upon divacancy migration above ~150°C, which coalesce completely only at high temperatures. Thus, the disappearance of the 1.8μm absorption band is a consequence of divacancies distortion when becoming part of the loose clusters, so they look rather like individual monovacancies and accordingly decrease the line-shape parameter [69].

Herein we report some positron results, obtained using variable-energy PAS, of fundamental measurements on Cz and epi Si wafers to investigate the annealing and the evolution behaviour of ion implantation induced defects.

4.1.2. Experimental Procedure

Samples used in this work were cut from two Si wafers, Czochralski and epitaxially grown, implanted with 50keV Si^+ ions at $5x10^{13}$ cm^{-2}. *In situ* annealing of the samples was carried out over a temperature range from 300 to 640°C and changes in the positron response were measured at each temperature with annealing time. Because annealing was performed *in-situ* using an electron beam heater stage, it is expected that the Ge detector used to collect the annihilation photons will get warm which affects its energy resolution and stabilization. Also, some of the electrons will escape

the heater assembly and are guided and then accelerated back towards the positron source, draining the battery attached to the moderator and reducing the positron signal. To overcome those two problems, the Ge detector was cooled by an air circulation and a potential of -800V was applied on a mesh mounted in the beam line to prevent escaping electrons from reaching the source end.

The projected range (R_p) of 50keV Si^+ in Si, as calculated by TRIM [30], is ~ 75nm with a straggle of ~ 28nm, giving vacancy-type damage at depth of ~ 100nm, which corresponds to the mean depth (z) penetrated by positrons with 3keV energy (E) as $z \approx 17.2E^{1.6} nm$. Therefore, to monitor the evolution of defects with annealing time, the positron response at the energy corresponding to the peak of the defected region (~3.5keV in this case, as can be seen in the positron response of as-implanted sample, for example in figure 4.3) was measured as the time elapsed at each temperature. So, measurements were performed continuously with 3.5keV positrons implanted into the sample which is set at the desired temperature. Measurement time was 600s (shorter for the highest temperatures, 600-640°C), i.e. every point was collected in a time of 600s. The response at 1 and 24keV was also measured frequently, to get an idea of any changes in the near-surface and the bulk states with annealing.

What is meant by the 'positron response' in the above paragraph is the conventional line-shape parameter, S, which characterizes the Doppler broadening of the annihilation line with 511keV γ-photons resulting from the annihilation of the positrons with the surrounding electrons. S, as usual, is defined as the ratio of counts in a central region of the annihilation line to that in the whole line, and, in general, increases for positrons trapped in vacancies.

After each at-temperature measurement, samples were cooled down and the S parameter was measured at RT to get $S(E)$ curves, with the entire range of positron energy E from 0.5 to 30keV, for comparison with the sample behaviour in the as-implanted case or at earlier stages of its annealing history.

4.1.3. Results and Discussion

The variation of the S parameter with the incident positron energy or positron mean penetration depth of as-implanted samples, as -for example- the curves shown in figures 4.3 and 4.4, shows that implantation with 50keV Si^+ ions introduces defects in the near-surface region (up to a mean depth of ~100nm). The defects in this region, which has a measured S varying in the range between 1.028 and $1.04S_b$ for the different pieces of the implanted wafers, are most probably in the form of divacancies. S_b is the measured S for the bulk material, normalized in all graphs presented here to be unity. The variation of the measured S values could be due to the inhomogeneous distribution of ions on the wafer during the implantation process.

4.1.3.1 Epitaxially-grown Si Samples

Figures 4.1 and 4.2 show the variation of the S parameter with annealing time in two of the samples from the epitaxially-grown wafer. The S(t) curves shown in figure 4.1 are for sample annealed at 470°C (a) and then after leaving it in air for about 5 weeks annealed again at 580°C (b). Figure 4.2 shows similar curves for a sample that has been annealed at 350°C then 600°C after 5 weeks in air. It can be seen that the S parameter at both 3.5 and 1keV is decreasing with annealing time, which would suggest that defects are being annealed out if it is assumed that it is only the concentration of defects that is changing and not their size. In those figures, two annealing stages at the two annealing temperatures in panels (a) and (b) can be easily distinguished. In figure 4.1, the first stage at the lower temperature starts from a value about that measured in the as-implanted case and ends after about 20h of annealing to reach its equilibrium at ~1.00, where no more change is observed. The second stage starts from the point where the first one ends, or slightly higher, and stops changing at ~0.98 after ~30h at 580°C.

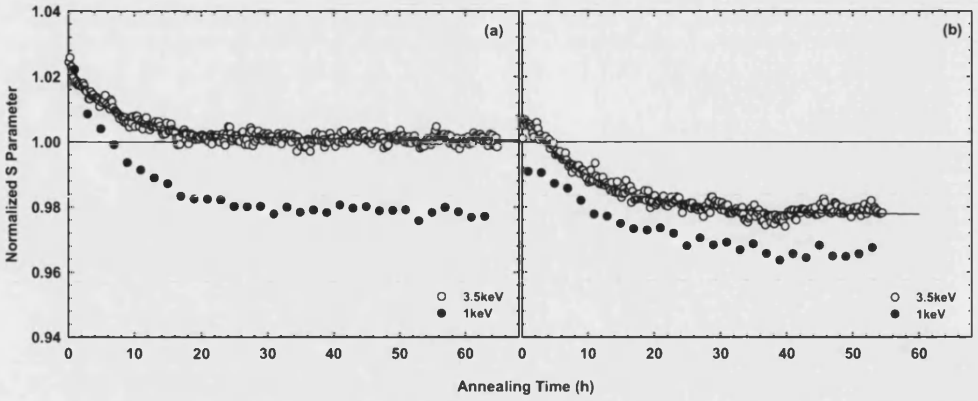

Figure 4.1 The variation of the *S* parameter at 3.5 and 1keV with annealing time at (a) 470°C and (b) 580°C. The solid lines through the points are exponential fits for the curves. The horizontal solid line indicates the bulk level measured with 24keV positrons.

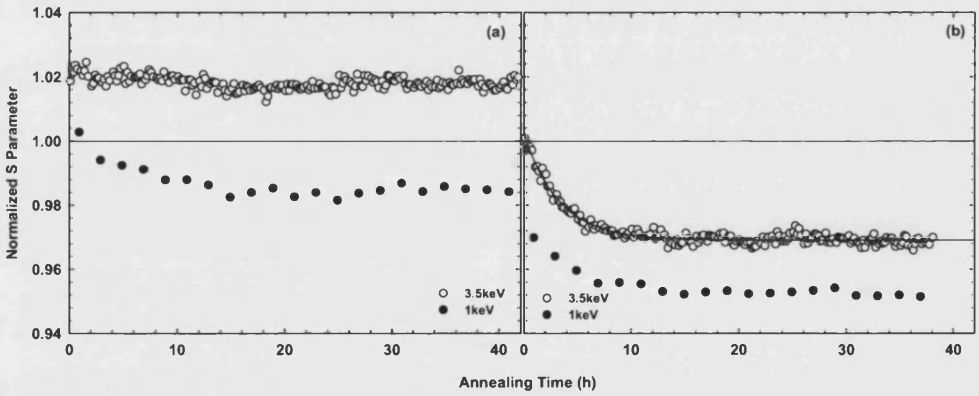

Figure 4.2 The variation of the *S* parameter at 3.5 and 1keV with annealing time at (a) 350°C and (b) 600°C. The solid line through the points in (b) is exponential fit for the curve. The horizontal solid line indicates the bulk level measured with 24keV positrons.

Figure 4.3 shows *S(E)* curves measured at RT after annealing at 470 and 580°C in comparison with that of the as-implanted case. The effect of the two annealing stages can clearly be seen; the first one at the low temperature (470°C) is showing a 'half-way' change which is believed to be associated with the formation of vacancy-clusters by the migration of smaller ones that has already been formed, perhaps at the beginning of the annealing where divacancies, which can not be found isolated at such

a temperature, attach to each other, as well as annealing out or break up of some of those clusters.

The second stage at the higher temperature (580°C) is enough to remove all the remaining defects. Similar observations of clustering of divacancies at intermediate temperatures in the range between 300 and 500°C and complete annealing at higher temperatures have been reported earlier in low-energy self-implanted Cz-Si [46] and also in high MeV implantation with heavier ions in FZ samples [48]. However, one can see that the interpretation of the results at the low temperature range as being solely due to vacancy agglomeration or clustering is inconsistent with the decrease observed in the *S* parameter, as *S* would be expected to exhibit an increase with clustering instead of a decrease.

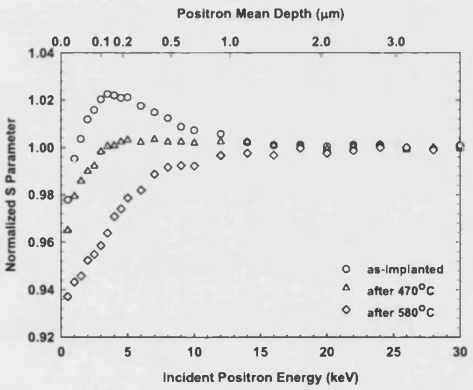

Figure 4.3 *S* parameter as a function of incident positron energy for one of the epi-Si samples; as-implanted and after annealing at 470 and 580°C.

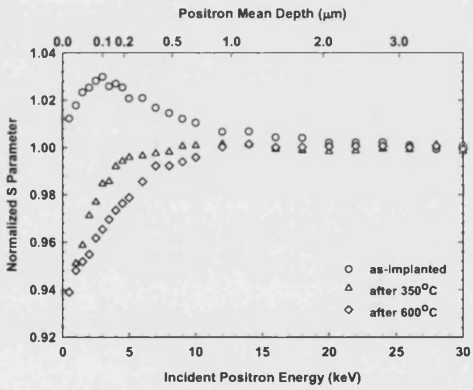

Figure 4.4 *S* parameter as a function of incident positron energy for one of the epi-Si samples; as-implanted and after annealing at 350 and 600°C.

Avalos and Dannefaer have observed similar behaviour in FZ samples irradiated with 10MeV electrons, where positron lifetime and *S* parameter did not show an increase upon annealing at high temperature up to 500°C as one would suppose due to vacancy clustering; the *S* parameter rather decreases. In their study, a model of loose clusters has been suggested to explain the unexpected results, where migrating divacancies initially form clusters but in rather a loose form as individual vacancies have not

coalesced completely and the clusters are perhaps viewed as individual monovacancies [69]. This cluster structure could be the one formed here in epi and Cz Si implanted with 50keV Si^+ ions.

Alternatively, the *S* parameter at 3.5keV may be simply a measure of the change in the defect concentration and not their size, so the decrease we observe is reflecting the decrease in the concentration of the vacancy-type defects forming the clusters.

The behaviour of the sample shown in figure 4.2 is similar but it reaches a lower equilibrium level (~0.97) after annealing at 600°C and starts from unity which is much lower than the level after annealing at 350°C. This is possibly because the temperature has been raised, immediately after the measurement at 350°C, to 450°C for a few hours (not shown here). However, the few hours annealing (~6h) at 450°C did not bring the *S* parameter to the starting level shown in (b), thus, the low starting value of the *S* parameter could be a direct result of annealing at such a high temperature (600°C) which is enough to decrease *S* by ~0.02 within the first ten minutes during accumulating the first point.

In panel (a) in the figure, 350°C seems to have no effect on the annealing of the defects, nevertheless, the *S*(E) curve in figure 4.4 measured after annealing at 350°C (and also 450°C for a few hours) shows a noticeable decrease in the *S* parameter after the annealing. This raises the question of whether the decrease we observe in *S* at 3.5keV is real, and due to migration of defects, or just because of the change in the *S* parameter at the surface (S_s) because of the change in its condition with temperature.

The change observed in *S* at 1keV (in this case and all other cases shown in figures 4.1 and 4.2), as well as the low *S* in *S*(E) curves in figures 4.3 and 4.4, may intensify this doubt. To investigate this, a simple method was carried out employing the VEPFIT program [62] to construct *S*(E) curves for the as-implanted sample with low surface *S* (i.e. by fixing S_s in the fitting model to that measured for the sample after annealing at 350°C) and vice versa -i.e., constructing a *S*(E) curve for the sample after annealing at

350°C with high S_s (the value measured for the as-implanted case). The result of this method, as presented in figure 4.5, shows that the surface change does not have much of a pronounced effect on the 3.5keV point as that on the 1keV point. In other words, the measured S parameter at 3.5keV, with a negligible effect of the surface change, can be directly utilized as a measure of the defect annealing, while that at 1keV is mirroring the change in the surface with only small fraction affected by the annealing of defects.

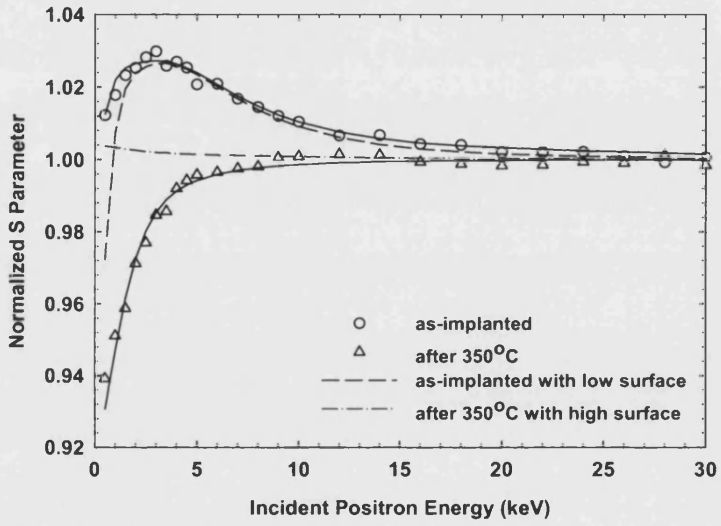

Figure 4.5 VEPFIT results for epi-Si sample; as-implanted and after annealing at 350°C, with different S parameter at the surface.

The curves shown in figure 4.3 after heating the sample to 470 and 580°C were also fitted to check for the effect of surface change and the results are shown in figure 4.6. The curve for the as-implanted case was fitted with S_s fixed to that measured after annealing at 470°C or 580°C and, inversely, the two curves after annealing were fitted with S_s fixed to that of as-implanted one. Again, as can be seen in the figure, the change in the surface has little effect on the 3.5keV points, implying that the changes we see in S at 3.5keV in figure 4.1 are due to clustering and annealing of the defects at 470 and 580°C, respectively.

It should be mentioned here that the *S* parameter value measured at RT after annealing all the measured samples in the temperature range between 300-500°C is always ~1.00S_b, and ~0.97S_b after annealing at the higher temperature range (>500-640°C). This confirms the observations reported earlier about the stability of such vacancy-clusters up to ~500°C and their annealing beyond it [46,49,69].

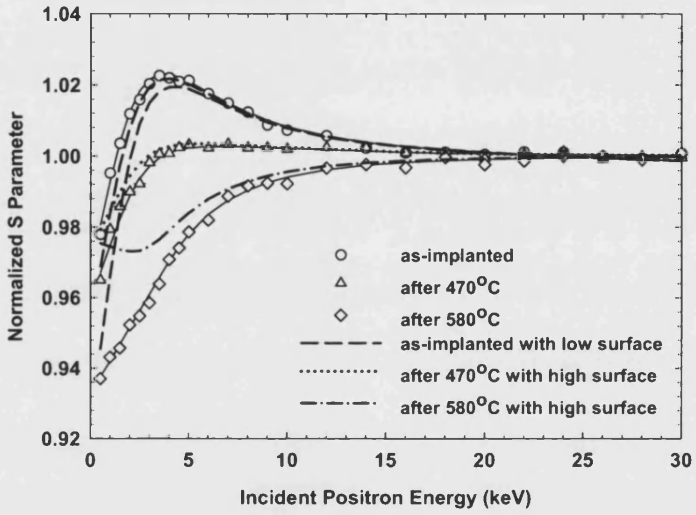

Figure 4.6 VEPFIT results for one of the epi-Si samples; as-implanted and after annealing at 470 and 580°C, with different *S* parameter at the surface.

As the change in *S* is falling nearly exponentially with annealing time *t*, attempts to fit the *S*(*t*) curves with an exponential decay function of the form of $S(t) = S_0 + ae^{-\lambda t}$ have been performed on the curves obtained for all annealing temperatures *T*. *S*(*t*) is *S* at any time *t*, S_0 is the equilibrium value of *S*, and λ is the decay rate. Such exponential decay fittings gave sensible fits with realistic decay rates that are consistent at the different annealing temperatures, where λ becomes shorter with increasing *T* implying that the annealing (at the high temperature range) or the clustering process (at the low temperature range) are, as one would imagine, getting faster as the temperature is increased. To obtain the activation energy (E_a) for each process, the clustering and the annealing of the defects, the values of λ were fitted to an Arrhenius relation

$$\lambda(T) = \lambda_0 e^{(-E_a/k_B T)} \tag{4.1}$$

where k_B is the Boltzmann's constant.

The fit results are shown in figure 4.7. Two separate lines were obtained, suggesting that there are two thermal processes happening at different range of temperatures. E_a of ~ 2eV has been obtained for the low temperature range which is proposed to be the energy required for vacancy clustering by the migration of smaller vacancies, whereas ~ 4eV seems to be necessary for annealing out those clusters at higher temperatures (>500°C). It should be declared that the values of E_a given here were obtained, as mentioned above, from the measured S parameter assuming that it is reflecting the change in the concentration of defects C. A value of 3.2±0.2 eV has been reported for the binding energy of vacancies to vacancy clusters [64]. This implies that dissociation of the clusters into smaller ones might be involved in the annealing process of the clusters.

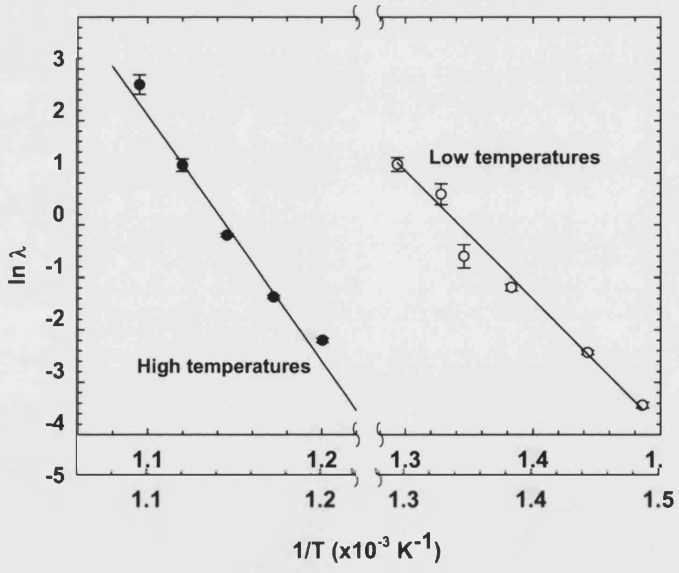

Figure 4.7 Arrhenius plots for epitaxial-grown samples annealed at temperatures in the range between 300 and 640°C. The open circles (○) are points obtained for the low temperature range (400-500°C) giving E_a of 2.11±0.66 eV, while the closed circles (●) are the points obtained for the high temperature range (560-640°C) giving E_a of 4.06±1.41 eV.

4.1.3.2 Czochralski-grown Si Samples

Measurements, analogous to the ones carried out on the epi-Si samples reported in the previous section, have been performed on Cz-Si samples and representative results are presented here. The two panels in figure 4.8 show the variation of the S parameter with annealing time for one of the measured samples annealed at (a) 420°C and (b) 580°C. The decrease observed at 420°C stabilizing after ~20h is followed by further decrease upon increasing the temperature to 580°C. The change in S parameter after those two stages of annealing compared with that of the as-implanted case is shown in figure 4.10. Again, as in the epi-Si results, the first annealing stage at the low temperatures is probably associated with the formation of vacancy clusters by the migration of vacancies, and the second stage at the high temperatures is certainly annealing out of those clusters. The possibility of any effect of surface change has been checked here also using the same method of modelling $S(E)$ curves with different possible S_s. The results, as can be seen in figure 4.12, are clearly showing that the surface change has only slight effect on the 3.5keV points.

Another example showing the annealing behaviour at higher temperatures is presented in figure 4.9. The sample in this case was annealed at 500°C then followed by a second stage at 640°C after leaving it in air for about three months. An intermediate annealing, most likely related to vacancy clustering, can be observed after the first stage annealing at 500°C (see $S(E)$ curve after 500°C in figure 4.11), while a rapid fall is exhibited in $S(t)$ at 640°C which is almost certainly due to the fast annealing of all the vacancy clusters, bringing the sample, as can be seen in figure 4.11, to a nearly defect-free piece of Cz-Si.

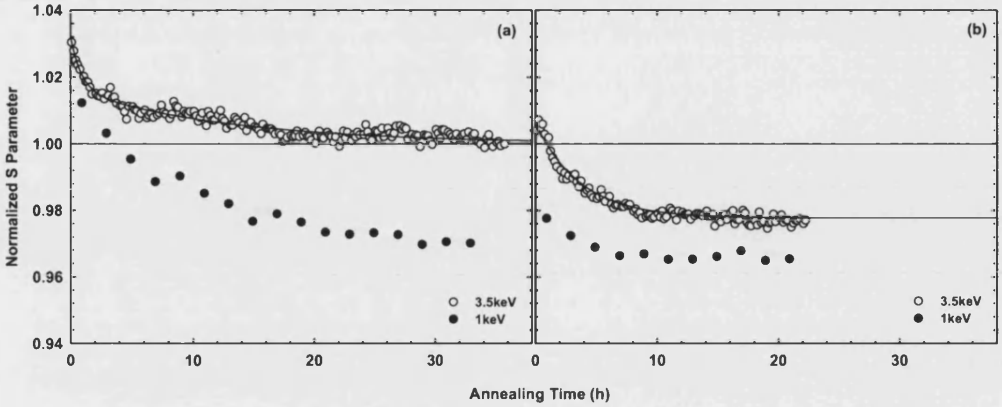

Figure 4.8 The variation of the *S* parameter at 3.5 and 1keV with annealing time at (a) 420°C and (b) 580°C. The solid lines through the points are exponential fits for the curves. The horizontal solid line indicates the bulk level measured with 24keV positrons.

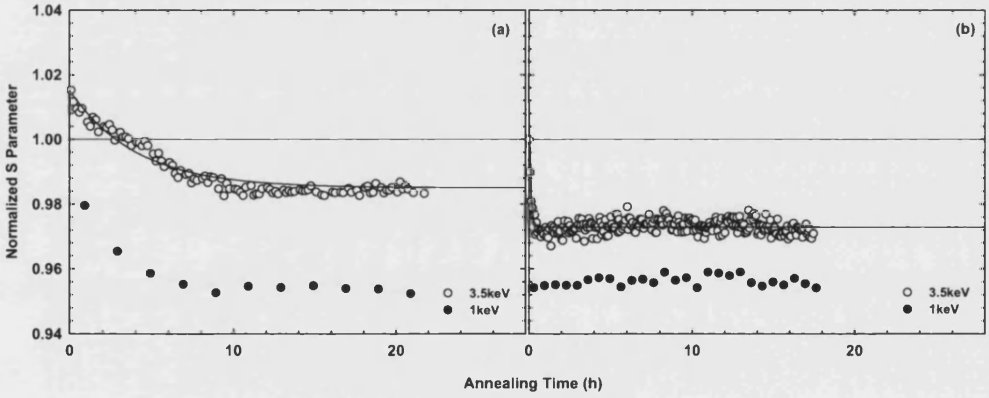

Figure 4.9 The variation of the *S* parameter at 3.5 and 1keV with annealing time at (a) 500°C and (b) 640°C. The solid lines through the points are exponential fits for the curves. The horizontal solid line indicates the bulk level measured with 24keV positrons.

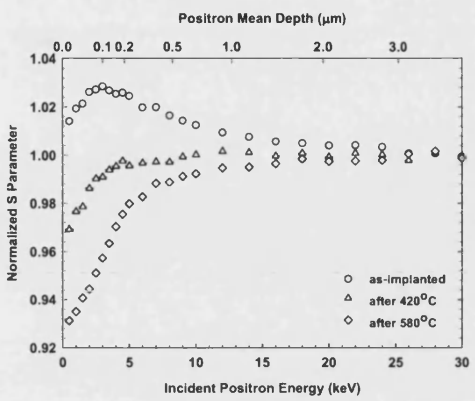

Figure 4.10 *S* parameter as a function of incident positron energy for one of the Cz-Si samples; as-implanted and after annealing at 420 and 580°C.

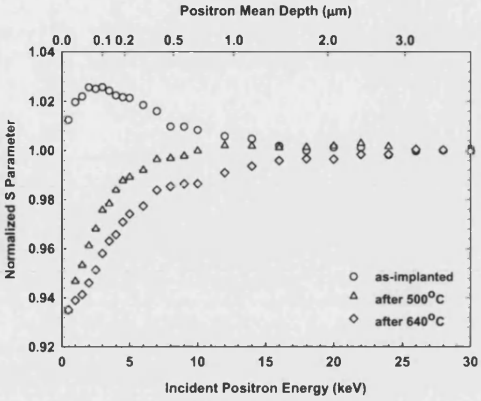

Figure 4.11 *S* parameter as a function of incident positron energy for one of the Cz-Si samples; as-implanted and after annealing at 500 and 640°C.

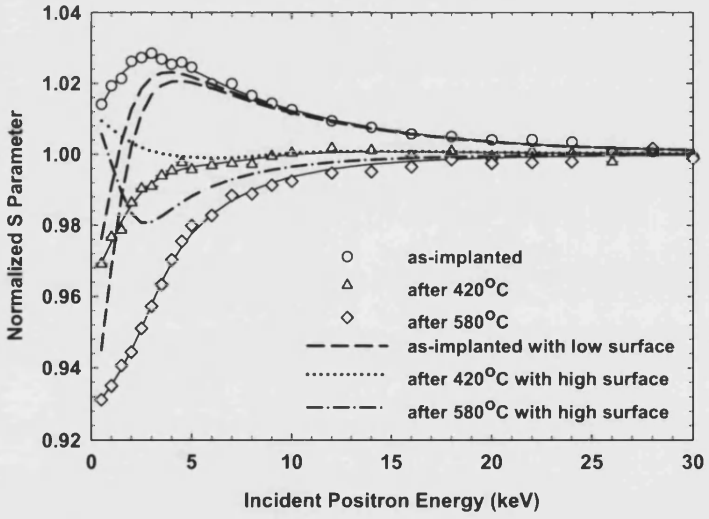

Figure 4.12 VEPFIT results for one of the Cz-Si samples; as-implanted and after annealing at 420 and 580°C, with different *S* parameter at the surface.

As the procedure followed for the epi-Si samples described in the previous section, all $S(t)$ curves obtained at the various annealing temperatures were fitted with an exponential decay function and the natural logarithm of the exponents was plotted versus the reciprocal of the temperature (in K^{-1}) as shown in figure 4.13, assuming that the decay rates are exhibiting an Arrhenius dependence. Again one can see two ranges of temperatures giving two separate lines with gradients giving E_a of ~2.7 and 3.3eV, where the former is resulting from the low temperatures (400-500°C) and associated with the migration of vacancies forming vacancy clusters, and the latter from the higher temperatures (>500 – 640°C) and it is apparently required for the complete annealing of the clusters.

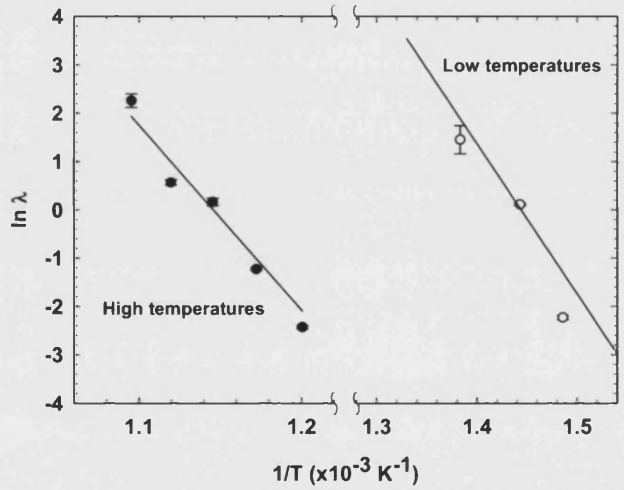

Figure 4.13 Arrhenius plots for Czochralski-grown samples annealed at temperatures in the range between 300 and 640°C. The open circles (○) are points obtained for the low temperature range (400-500°C) giving E_a of 2.68±0.02 eV, while the closed circles (●) are the points obtained for the high temperature range (560-640°C) giving E_a of 3.31±1.36 eV.

It should be mentioned here that the exponents plotted in figure 4.13 for the low temperature range were obtained by fitting the S(t) curves with a double-exponential function, as they could not be fitted reasonably with a single-exponent like the epi-Si samples. This is possibly because the Cz-Si samples annealed at temperatures in the low range have been etched chemically before starting any thermal treatment, which

means that the native oxide layer has been removed from the samples' surface, thus the surface is expected to become oxidized easily upon thermal treatment. Therefore, in our double-exponential fit we get a slow exponent which is probably related to the change in the surface state and a fast exponent which is believed to be associated with the rapid process of the formation and the migration of vacancy clusters. Hence, this fast component is used here in the Arrhenius plot to get the activation energy of the clustering of vacancies. In the case of epi-Si where the samples were unetched with native oxide layer on the surface, not much change is taking place at the surface with thermal treatment, and so the single-exponential fit gave sensible and self-consistent results for the decay rates and as a result the activation energy of the clustering process, as shown in figure 4.7.

4.1.3.3 Comparison between epi- and Cz-Si

Comparing the activation energies of epi- and Cz-Si samples as shown in figure 4.14, it is revealed that Cz-Si samples generally exhibit faster annealing rate than in epi-Si; much faster in the low temperature range between 400 and 500°C but only slightly higher in the high temperature range between 560 and 640°C. In the low temperature range, this means that at the same annealing temperature the vacancy clustering process is quicker in Cz-Si compared with epi-Si, where the equilibrium state of the clustering -i.e., when it can not progress more- is reached faster.

This can be understood in terms of the number of steps needed to reach the equilibrium state; it can be concluded that fewer steps are needed in Cz-Si than in epi-Si, possibly because of the difference in the impurity content between those two types of Si. In Cz-Si, more impurities exist and it is believed that those impurities can act as seeds for the clusters and hence enhancing the clustering process and making it happen and complete faster than in epi-Si. On the other hand, in high-purity epi-Si material, more steps are needed to reach the equilibrium state of clustering because there are no impurities to aid the developing process; hence the decay rates are slower.

The activation energy is slightly higher in Cz compared with epi, implying that vacancy clustering process in the presence of impurities needs shorter time because of the developing of the process by the impurities, once the vacancies found them, but higher energy to get the vacancies to find each other and get attached, whereas in epi-Si without impurities, vacancies take longer time to get clustered but with lower energy perhaps because in this case there is no impurities interfering with the vacancies and holding them up from finding each other.

In the high temperature range, not much difference in the decay rates can be observed between the two materials. A slightly longer time is needed for the annealing of the clusters in epi-Si compared with Cz-Si but with higher activation energy. This is possibly because, as it is stated earlier, vacancy clusters are formed in Cz with the aid of impurities so one would expect that it is easier and require less energy to break up or anneal out those clusters compared with the ones that are formed independently as in epi. As pointed out earlier, it should be mentioned here that the complete annealing of the vacancy clusters could be preceded by dissociation of the clusters into smaller ones with lower activation energy.

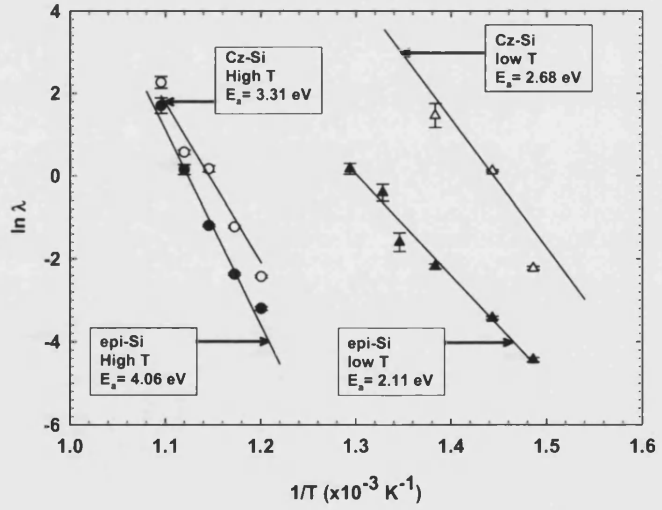

Figure 4.14 Arrhenius plots for epi and Cz-Si samples obtained for two ranges of temperatures; low range between 400 and 500°C and high range between 560 and 640°C. The activation energies obtained for the two types of samples at the two ranges of annealing temperatures are given in the figure.

4.1.3.4 Positronium Fraction Parameter

Another parameter that has been measured with annealing time at all temperatures, simultaneously with the *S* parameter, is the *F* parameter. This parameter is a direct measure of the fraction of positrons that forms positronium (Ps). It is the ratio of counts in the 511keV peak to that in the valley region of the annihilation spectra. 75% of the Ps formed is in the triplet (*ortho-*) state, *o*-Ps, this predominantly decays with the emission of three gamma photos, which appear mainly in the valley region with a negligible number in the 511keV photopeak. Conversely, the 25% of Ps formed in the singlet (*para-*) state, *p*-Ps, decays with the emission of two 511keV photons which appear in the 511keV photopeak. Therefore, if more *o*-Ps is formed, *F* parameter decreases.

As reported in the literature, Ps is expected to be formed above the surface of semiconductors at high temperatures where positrons trapped in the surface potential well are desorbed as Ps [70]. However, our measurements have shown different behaviour for the *F* parameter in samples annealed at a range of high temperatures. Examples of those behaviours are shown in figure 4.15.

With an exception of the curve shown in panel (b), it can be said that in general *F* shows an increase in the first few hours of annealing until it becomes constant by reaching the bulk value. The behaviour shown in (b) for epi sample while it is annealed at 600°C exhibits almost constant *F* parameter except a slight increase in the first hour. This could be because the sample has been etched before starting any measurements and it also has been annealed to 350°C before going to 600°C. The etching and cleaning of the surface by removing the oxidized layer may have an effect on increasing the number of positrons getting back to the surface and form Ps there. This has been seen in some etched samples (not shown here). However, what is seen here is to the contrary and it could be understood as positrons getting back to a clean surface are probably annihilating freely with no chance to form Ps. The behaviour of *F*

with annealing at 350°C (not shown here) is almost similar to the one shown here with annealing at 600°C.

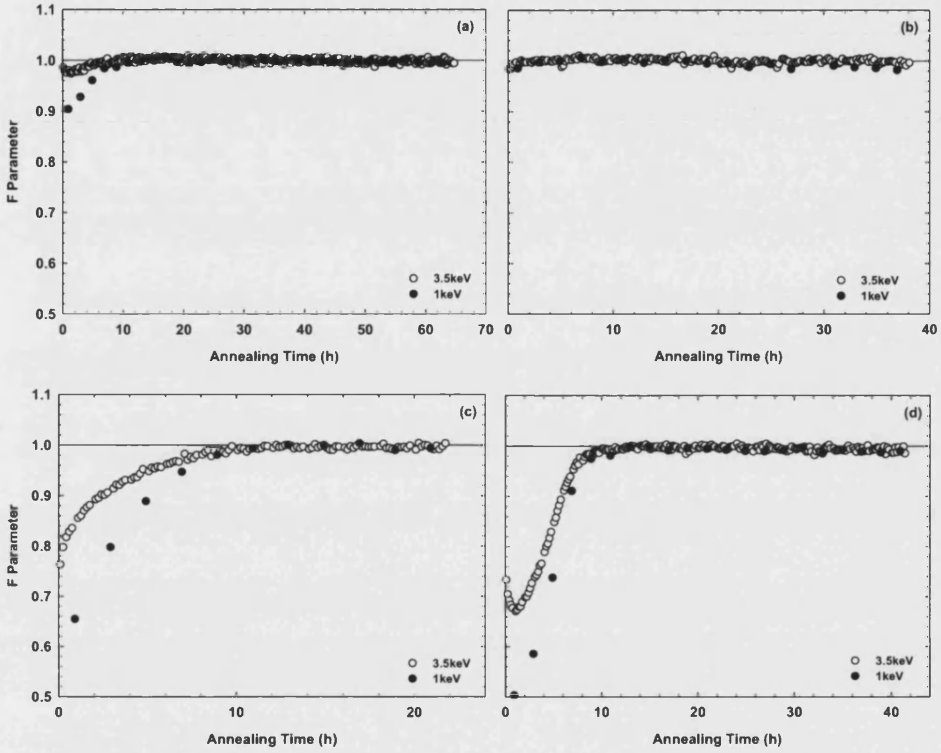

Figure 4.15 Examples of the change in *F* parameter at 3.5 and 1keV with annealing time in different samples (a) epi-Si annealed at 470°C, (b) epi-Si annealed at 600°C, (c) Cz-Si annealed at 500°C, and (d) Cz-Si annealed at 600°C. The horizontal solid line indicates the bulk level measured with 24keV positrons.

Coming back to the main point of the increase in *F* parameter in the first few hours of annealing displayed by most of the samples; this increase means that Ps formation starts at the beginning of the annealing and then decreases with increasing annealing time. Over the same period of annealing the *S* parameter exhibits a decrease; hence, the change observed in *F* can be linked with that seen in *S* as the increase in *F* means that less Ps are formed with increasing the annealing time, and hence the number of counts in the 511keV annihilation peak will decrease which means that *S* will decrease as well. However, the decrease seen in *S* always shows a higher change than that in *F* and it also persists for a longer period. This verifies that the change measured in *S* is

mostly due to changes in the defects, either clustering by migration or annealing away, with only a small fraction related to the change in surface which includes Ps formation.

An interesting behaviour like the one shown in panel (d) in the figure below has been observed in some of the samples. It shows an initial decrease in the *F* parameter within the first hour of annealing then an increase in the next few hours until it reaches the bulk value, which means that Ps formation is increasing in the first hour and then gradually decreasing upon continuing annealing. Further investigations are needed to explain this behaviour and to get clarification and better understanding for the relation between the change in the Ps fraction and the *S* parameter with annealing at high temperatures.

4.1.4 Conclusion

In this work we have reported some findings on the behaviour of defect migration, clustering and annealing in Si, both Cz and epi-grown. At-temperature measurements of the Doppler-broadened annihilation peak have been performed to follow the evolution of the defects upon annealing in the range between 300 and 640°C. Our results revealed that low temperatures (300–500°C) cause clustering of the implantation-induced defects, while higher temperatures (>500-640°C) are necessary to anneal away those clusters. Faster annealing rates in the low temperature range have been observed in Cz compared with epi, which has been attributed to the presence of impurities in Cz facilitating the defect clustering process. Annealing in the high temperature range showed slight difference between the two types of the material and again faster annealing in Cz.

4.2 Evolution of Vacancy-type Defects in MeV Self-implanted Cz-Si

To add more details to the picture of the evolution of vacancy-like defects drawn in the previous section, we studied here the behaviour of deep defects introduced by MeV Si^+ ions in Cz-Si. Besides generating deep damage in the samples, high-energy ion implantation causes separation of the vacancy-rich and interstitial-rich regions produced upon the implantation. With the defects well deep inside the samples, the effect of the change in the surface on the measured parameters would be eliminated. The measurements here involve isochronal, rather than isothermal, annealing. The rest of this section is reporting the observations of vacancy clusters formed in Cz-Si after high energy ion implantation.

Vacancy clusters were created by 2 MeV Si ion implantation of 1×10^{15} ions/cm^2 and after annealing between 600 and 650°C. Doppler broadening measurements using a slow positron beam have been performed on the self-implanted Si samples, both as-implanted and after annealing between 200 and 700°C for time intervals ranging from 15 to 120 min. No change in the *S* parameter was noted after the thermal treatment up to 500°C. However, the divacancies (V_2) created as a consequence of the implantation were found to start agglomerating at 600°C, forming vacancy clusters in two distinct layers below the surface; the first layer is up to 0.5 μm and the second layer is up to 2 μm. The *S-W* plots of the data suggest that clusters of the size of hexavacancies (V_6) could be formed in both layers after annealing for up to an hour at 600°C or half an hour at 650°C. After annealing for longer times, it is expected that vacancies are a mixture of V_6 and V_2, with V_6 most probably dominating in the first layer. Further annealing for longer times or higher temperatures breaks up the vacancy clusters or anneals them away.

4.2.1 Introduction

Although the technological and industrial demands focus on the use of low-energy ion implantation for shallow junction formation, high-energy (MeV) ion implantation has also many potential applications in different areas. Examples of these applications are the production of buried dielectric layers and impurity gettering. For forming a dielectrically isolated Si layer, oxygen is usually implanted at high energy and high dose into a silicon substrate to form silicon on insulator (SOI) structure for use in fabricating ICs. Another, more recent, technique for producing buried dielectric isolated layers has been introduced. In this Smart-Cut technique, high dose of H implantation is used and the thickness of the Si layer is controlled by the energy of the implanted ions [71]. For impurity gettering, high-energy ion implantation, with H or He ions, is used to form a layer of cavities to be used as a getter layer for impurities in Si [55]. High-energy ion implantation is also used to quantitatively profile vacancies by Au labelling [57,72].

Knowledge about formation and evolution of vacancies upon annealing of ion-implanted silicon is of great importance for the understanding of their applications. As mentioned in the previous section, the appearance of vacancies and their agglomeration to form vacancy clusters during annealing of ion-implanted Si has been widely studied using different techniques. For example, Fujinami et al. [46] studied the behaviour of vacancy-clusters formed in low-energy self-implanted Cz-Si using VEPAS and RBS. The annealing characteristics of two doses, one above and one under the critical value for amorphization, have been investigated in their study. Simulation of clustering of vacancies and their diffusion in ion-implanted Si during annealing has been performed by Gilmer et al. [73] using molecular dynamic methods, and quantitative study for the evolution of point defects into clusters upon annealing of ion-implanted Si has been provided by Benton et al. [74] using DLTS.

In this work, the formation of vacancy clusters and their evolution following annealing at different temperatures and times of Cz-Si implanted with 2MeV Si^+ ions is studied using VEPAS.

4.2.2 Experimental Procedure

Four identical pieces of Cz-grown Si with resistivity of 40 Ω.cm were used in this work. The samples were implanted with 2 MeV Si^+ ions at 1×10^{15} cm^{-2} dose. *In-situ* annealing of the samples was carried out over a temperature range from 200 to 700°C for time intervals between 15 and 120 min. All annealing was done using an electron beam heater that heats the sample, which is electrically isolated from the heater, by radiation. The sample is attached to a thermocouple to monitor its temperature. The heater together with the thermocouple is connected to an electron beam power supply with a temperature controller on which the required temperature is set. The set temperature of the sample was usually reached within 2 min from the beginning of the heating process. The procedure followed in annealing the samples was to start by heating one of the samples to 200°C for different time intervals (15, 30, and 60 min), if no change is noticed after 60 min, annealing is carried on to the next higher temperature (300°C) and etc. until a change is observed, then a new piece is used for the next annealing temperature.

Doppler Broadening measurements start after cooling the sample to room temperature. All measurements were carried out using a mono-energetic, magnetically-guided, positron beam where positrons in an energy range of 0.5 to 30 keV were implanted into the samples and Doppler broadening of the 511 keV annihilation γ rays was measured at room temperature using a liquid nitrogen-cooled HP Ge detector with a resolution of 1.44 keV.

For data analysis, the conventional *S* and *W* parameters were used, where *S* is defined as the ratio of counts in the central region of the 511 keV annihilation line to the total number of counts in the line, while *W* is the ratio of counts in the wing regions of the

line to that in the whole line. The two parameters are sensitive to the presence of vacancy-type defects and every type of defects has a characteristic *S* and *W* value. In general, in the presence of open-volume defects, the *S* parameter is higher than the bulk value, whereas the *W* parameter is lower.

4.2.3 Results and Discussion

Measurements of the *S* parameter after annealing the samples in the temperature range from 200 to 500°C, as can be seen in figure 4.16, did not show a noticeable change from that of the as-implanted sample. However, the sample annealed to 600°C shows a significant increase in the *S* parameter. Figure 4.17 shows the variation of the *S* parameter after annealing for different time intervals at 600°C and 650°C. The *S* parameter increases after heating for 15 and 30 min and then decreases gradually with increasing the annealing time. The behaviour of the as-implanted sample is shown as a reference mark. The abrupt increase in the *S* parameter after 15 and 30 min annealing is attributed to annealing-enhanced agglomeration of the defects created by the implantation, forming vacancy clusters which are then broken up or annealed away with further annealing for longer times.

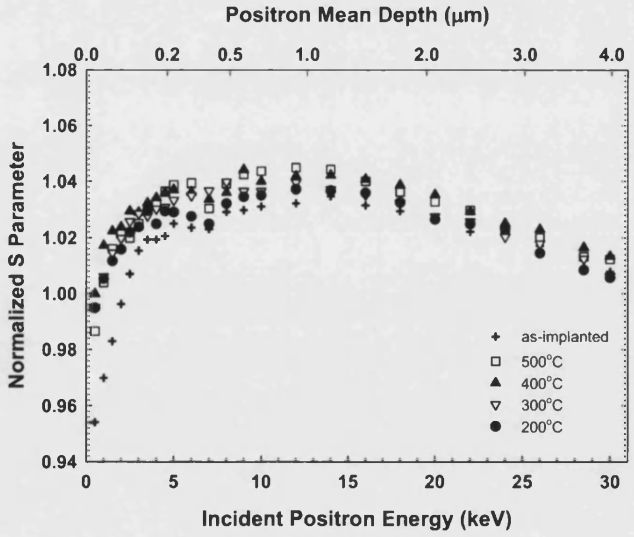

Figure 4.16 Normalized *S* parameter versus positron beam energy (keV) for the sample implanted with 2 MeV, 1×10^{15} Si^+/cm^2 after annealing for 30 min at 500°C, 400°C, 300°C, and 200°C.

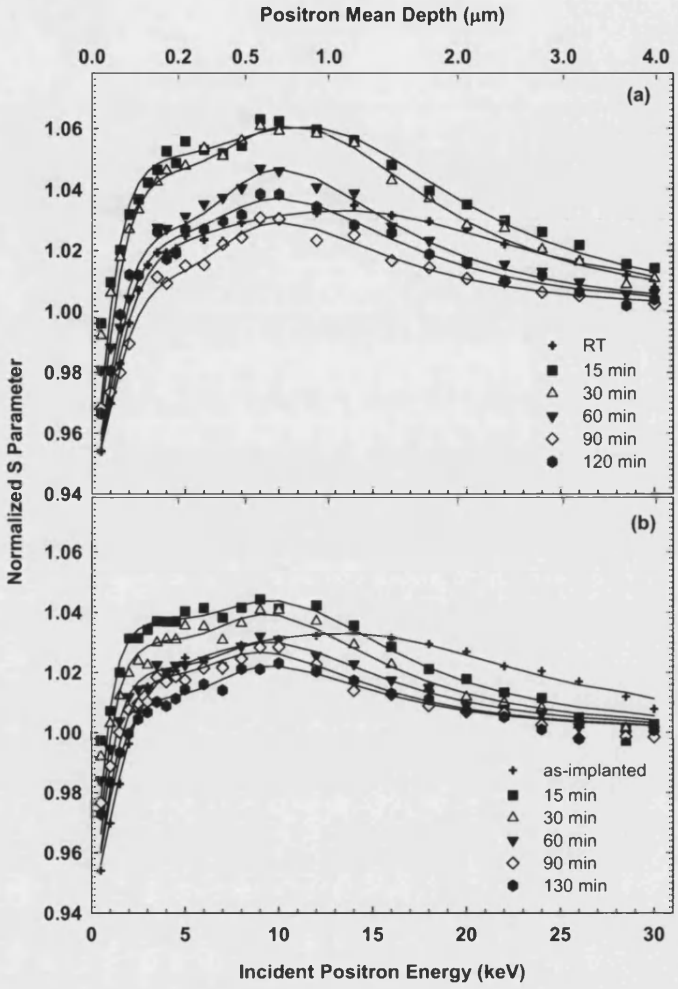

Figure 4.17 Normalized *S* parameter versus positron beam energy (keV) for the sample implanted with 2 MeV, 1×10^{15} Si^{+}/cm^{2} after annealing at (a) 600°C (b) 650°C for different time intervals. The solid lines are the fitting results using VEPFIT.

All the data collected at different temperatures and times were fitted using the fitting program VEPFIT [62]. As two regions (0-0.5μm and 0.5-~2μm) can clearly be distinguished from the raw data, an input model consisting of two defected layers has been assumed for this set of data. The variation of the fitted *S* parameter in the two defected layers with annealing time is shown in figure 4.18 for the samples annealed at 600 and 605°C. As can be seen, for the sample annealed at 600°C, the *S* parameter increases to reach its maximum (S_d =1.07S_b) after annealing for 30 minutes, indicating

that clustering of defects has been formed, then it declines with annealing for longer times, which means that the clusters have been broken-up or annealed away. The sample annealed at 650°C followed the same manner but with lower *S* values. An anomalous behaviour has been noticed upon annealing the sample for 120 min at 600°C, where the *S* parameter increases again implying a possible re-clustering for the vacancies after long time annealing, or it can be explained in terms of vacancies released from vacancy-oxygen (VO) complexes, which are usually formed in Cz-Si, during thermal treatment for long times at elevated temperatures [75]. A similar behaviour has been observed earlier in studying VO complexes in Cz-Si implanted with 1 MeV and 1×10^{16} cm^{-2} Si after annealing at 950°C for 10 seconds [76], and it was attributed to VO dissociation at this temperature. However, further work is needed to investigate this behaviour.

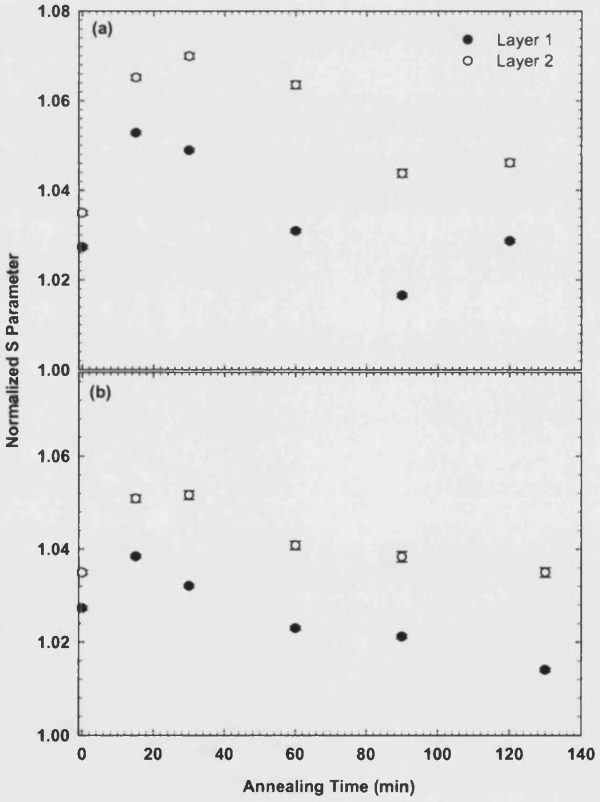

Figure 4.18 Normalized *S* parameter in the two defected layers as a function of annealing time. The two graphs are for the samples implanted with 2 MeV, 1×10^{15} Si^{+}/cm^{2} after annealing at (a) 600°C and (b) 650°C.

For the sample annealed to 700°C, very low *S* parameter values (with an average of ~ 1.014 S_b) have been measured in the two layers after 15 min annealing time, implying that a very short annealing time (< 15 min) is needed for forming and breaking up vacancy clusters at this temperature. Figure 4.19 shows these low *S* parameter values after annealing the sample at 700°C.

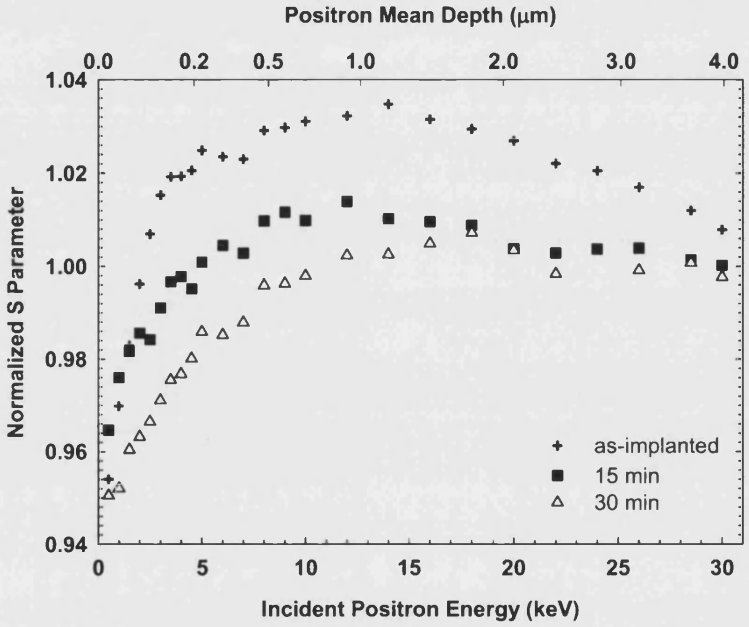

Figure 4.19 Normalized *S* parameter versus positron beam energy (keV) for the sample implanted with 2 MeV, 1×10^{15} Si^+/cm^2 after annealing at 700°C for 15 and 30 min. The as-implanted sample is shown as a reference.

To determine the nature of the defects in the two layers, the characteristic *S* parameter of the two layers (S_{Vx}) was calculated. This calculation was based on the fact that divacancies (V_2) are the most dominate type of defects formed in Si after ion implantation [77], and on an assumption that there is a saturation of V_2 in the two layers in the as-implanted (before annealing) sample. Hence, using a value of 1.04 for S_{V2}, the trapping rate of defects (F_d) was found to be 65% and 85% in the first and second layer respectively. If the same trapping rates were assumed in the two defected

layers after annealing the samples, then the characteristic S parameter (S_{Vx}) in the defected layers can be found using the formula

$$F_d = \left(S - S_b\right) / \left(S_{V_x} - S_b\right) \tag{4.2}$$

where S and S_b are the measured S parameter and the value of S in bulk Si respectively. Our calculations, based on this formula, gave an average value of 1.0764 for S_{Vx}. According to the characteristic values of S_{Vx} for X = 2 to 5 for measurements taken using university of Bath system with a spectrometer of 1.44 keV resolution [78] and extrapolating to S_{Vx}/S_b = 1.0764, as shown in figure 4.20, it can be deduced that the defects are most likely hexavacancy clusters (V_6).

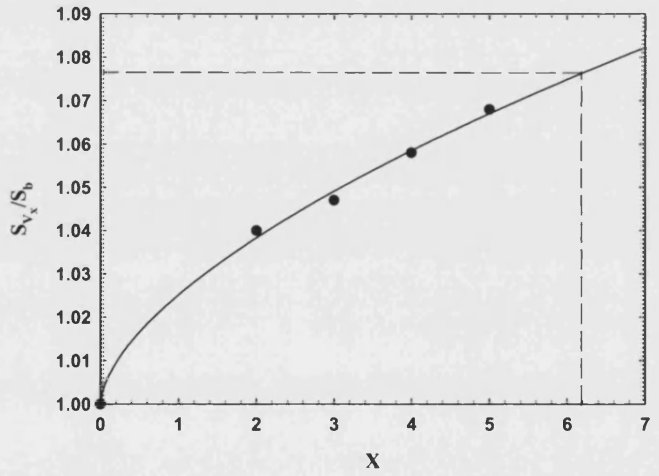

Figure 4.20 The characteristic S value (S_{Vx}) for different size of vacancies, showing that $S_{V6} \cong 1.0764$

However, it is not certain that the vacancies are all V_6 in the two defected layers; there may be a mixture of V_6 and V_2 or other smaller vacancies. Hence, an alternative approach to identify the type of defects has been pursued, namely, S-W plots of the raw data. A careful look at these plots reveals that various states can exist in these samples; samples annealed at 600 and 650°C for short times (15 and 30 min) show an evidence for an existence of annihilation site at the characteristic (W,S) point of V_6, the same samples after annealing for longer times show a sign for an existence of a

mixture of annihilation sites indicating that there is a combination of different size vacancies which are most likely V_6 and V_2, and lastly, a state where there is only a single defect annihilation site is exhibited by samples annealed for longer times or higher temperature. Examples of these three cases are shown in figure 4.21.

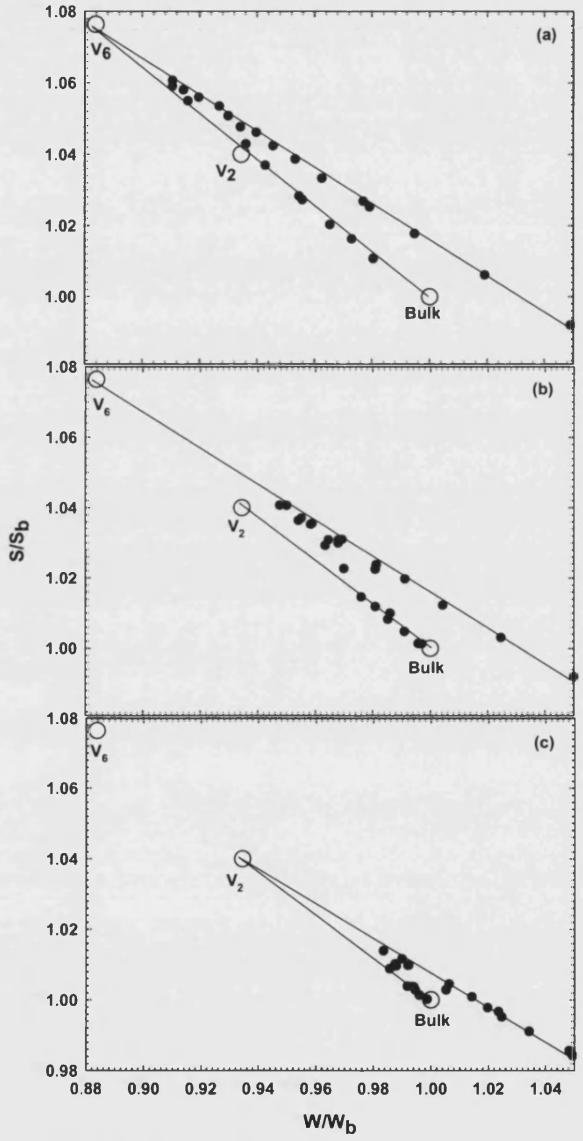

Figure 4.21 *S-W* plots for samples implanted with 2 MeV Si ions at 1×10^{15} cm^{-2} dose after annealing at (a) 600°C for 30 min, (b) 650°C for 60 min and (c) 700°C for 15 min. The circles are the dominate annihilation sites for positrons.

Attempts to determine the activation energy (E_a) needed for V_6 to anneal away or break up into smaller vacancies have been performed. But, since a combination of V_6 and some other smaller vacancies, most probably V_2, can be existed sometimes, difficulties have been faced to get certain value for E_a. However, if just cases where all the vacancies are assumed to be V_6 at 600 and 650°C have been taken into account, then the activation energy can be calculated. Defect concentration C_d is assumed to exhibit Arrhenius behaviour

$$C_d = C_o e^{(-E_a/k_B T)} \tag{4.3}$$

where C_o is the defect concentration at $t = 0$, k_B is Boltzmann's constant and T is the absolute temperature.

C_d depends on the fraction of positrons that trapped in defects (F_d) as

$$F_d = \frac{\nu C_d}{\tau^{-1} + \nu C_d} \tag{4.4}$$

where τ is the positron lifetime in bulk Si, and ν is the defect-specific positron trapping-rate. The trapped fraction of positrons depends on the value of the S parameter as

$$S = F_d S_d + (1 - F_d) S_b \tag{4.5}$$

where S_d and S_b are the characteristic values of the S parameter for positrons annihilating in defects and in bulk respectively.

Hence, the defect concentrations for the cases where all vacancies are assumed to be V_6 after annealing at 600 and 650°C were calculated and plotted against annealing time. The three points obtained in the case of 600°C annealing temperature is shown in

figure 4.22. The time $t_{1/2}$ (where $t_{1/2} = t_{annealing}$ when $C_d = C_o/2$) was determined in both cases and then $ln\ (t_{1/2})$ is plotted against $1/T$ (K^{-1}) in order to obtain a value for the activation energy. As illustrated in figure 4.23, if both, at T= 600 and 650°C, $t_{1/2}$ points plotted, this requires a value of 29.4 min for $t_{1/2}$ for annealing at 700°C, which can not be the case. However, if we take out the 650°C point, as there is some doubts about the identity of defects exist there, and assume that the maximum value for $t_{1/2}$ after annealing to 700°C is 7.5 min, then the minimum value for the activation energy would be 1.22 eV. This value is smaller than what is expected for V_6 as the reported values for the activation energy of V_2 [35,77] has an average of ~ 1.1 eV, and a value for the binding energy of vacancies to clusters has been reported to be 3.2 ± 0.2 eV [64].

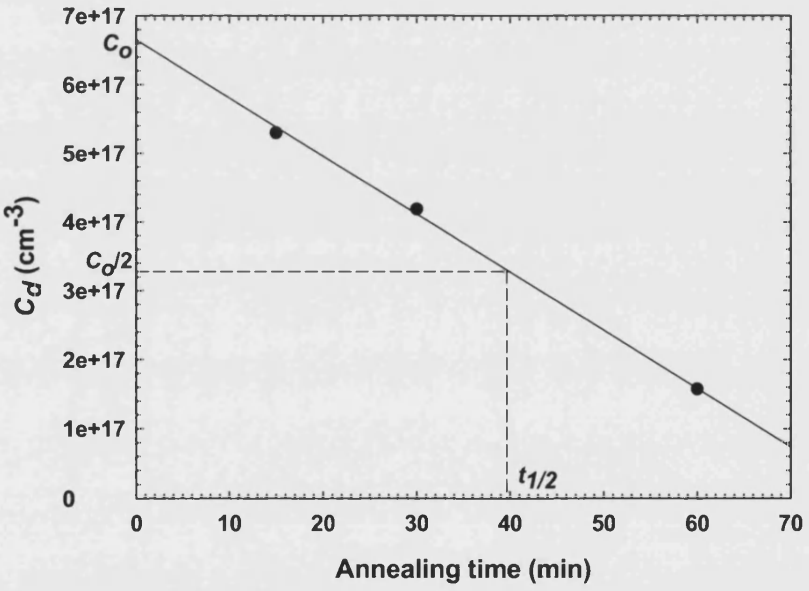

Figure 4.22 Defect concentration C_d (cm^{-3}) versus annealing time (min) for the cases where all the vacancies are assumed to be V_6 after annealing the sample at 600°C. $t_{1/2}$ ~ 40 min.

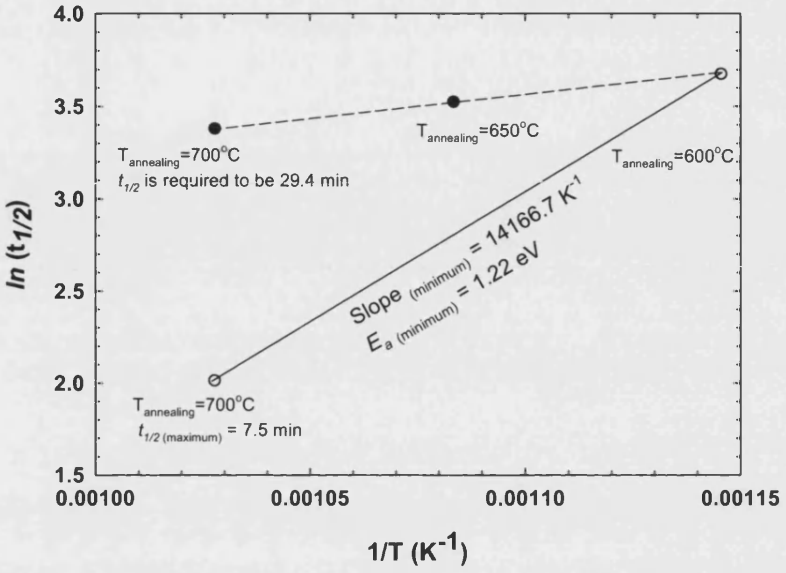

Figure 4.23 *ln* ($t_{1/2}$) versus *1/T* (K^{-1}) assuming all vacancies are V_6 after annealing at 600 and 650°C for short times. The minimum value obtained for the activation energy is 1.22 eV.

4.2.4 Conclusion

It has been shown that vacancy clusters can be formed due to agglomeration of divacancies (V_2) in self-implanted Cz-Si upon annealing at elevated temperatures (600°C), and eventually, after annealing for long times or to higher temperatures, these clusters anneal away or break up into smaller vacancies, probably V_2.

4.3 Room Temperature Diffusion of Vacancy-type Defects in Si

A simple method has been performed in this study to investigate the diffusion of ion-implantation induced defects at RT. This method is based on using specially-prepared samples with specified masked ridges to allow for precise implantation percentage and hence be able to get an estimation of any diffusion of the introduced defects. The

obtained results suggested an average distance of 300nm for defect diffusion; or probably the undercutting of the implanted ions.

4.3.1 Introduction

Knowledge about diffusion and migration of ion-implantation induced defects, at both RT and elevated temperatures, is of importance for the understanding of their behaviour and a large variety of phenomena based on their effect on the electrical and structural properties of the material, such as TED. Numerous studies have focused on RT migration of point defects, interstitials and vacancies, generated by ion implantation as they can freely migrate at RT because of their low migration energy which is <1eV [79]. Example of those studies is an earlier work carried out by Privitera et al to investigate RT diffusion of defects generated by 40keV Si implants and their interaction with dopants and native contaminants such as O and C. It has been found that the generated defects undergo trap-limited diffusion and produce dopant deactivation [79,80]. In this section, a simple method to investigate RT diffusion of defects generated by 100keV As^+ ions in Si is discussed.

4.3.2 Experimental Procedure

Five samples of Czochralski-grown Si wafer (p-type, 0-100 Ω.cm, <100>) were prepared for this work. Firstly, striped photoresist masks with specific strip widths and 1:1 aspect ratio were deposited evenly on the Si wafer which has an insulating SiO_2 layer on its surface by A.P. Knights at McMaster University. Then, samples were etched chemically using HF dissolving the masks and the SiO_2 between them but leaving that underneath. After that, 100 keV As^+ ions at $3x10^{14}$ cm^{-2} were implanted and samples were etched again to remove the SiO_2 layers. This procedure of masking and implanting through the masks is to ensure that the implantation through the samples is only 50% of the total percentage. The five samples have masked ridges

with different widths; 50, 10, 5, and 2 μm. A mask-less sample with 100% implantation was also provided as a reference.

Doppler broadening measurements were performed on all samples, and positron annihilation spectra were collected and characterized using the sharpness and the wing, *S* and *W*, parameters.

4.3.3 Results and Discussion

Figure 4.24 shows the variation of the *S* parameter with the incident positron energy for the four masked samples measured a month after the implantation. The behaviour of a 100% implanted mask-less sample is also shown as a reference. It can clearly be seen that the *S* parameter response of the masked samples is about 55% of that of the mask-less one, except for the one with 2 μm ridges where higher response (~70%) is exhibited possibly because diffusion is more pronounced in this thinly-striped sample. All samples have been measured again, a month and two months after the first measurements, to check for any diffusion with time at RT. The obtained results (not shown here) showed more or less the same level for the measured *S* parameter, implying that no diffusion has occurred after the first measurements. This raises the question of whether the extra 5%, in the 50, 10, and 5 μm ridges samples, or the 20%, in the 2 μm ridges sample, measured over the expected 50%, are due to defect diffusion at RT or not. Simulation of the distribution of 100keV As^+ ions in Si and the vacancies produced by the implantation process, using TRIM code [30], showed that the maximum range of the ions is ~0.17 μm and the introduced vacancies will be spread up to ~0.15μm. Thus, any diffusion for the vacancies at RT is not expected to extend a long distance beyond the ridge limits. Optical microscope showed indefinite edges for the implanted ridges suggesting that the implanted ions are probably undercutting the masks giving slightly over 50% implantation. Hence it is believed that the percentage over 50 measured in *S* is not wholly due to defect diffusion and that positrons are sensitive to the extra damage generated by the diffused ions.

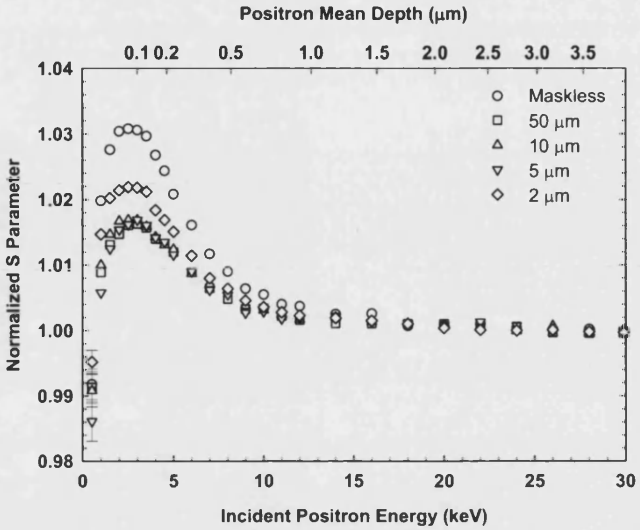

Figure 4.24 *S* parameter versus incident positron energy for the four masked samples with 50, 10, 5, and 2 μm ridges. The behaviour of mask-less sample is also shown for comparison.

S versus *W* plots for the four masked samples as well as the mask-less one are shown in figure 4.25. Three annihilation states (surface, defect, and bulk) for the implanted positrons are defined in the graph. The fraction of those states has been calculated in the different samples and that of the defect state is shown in figure 4.26.

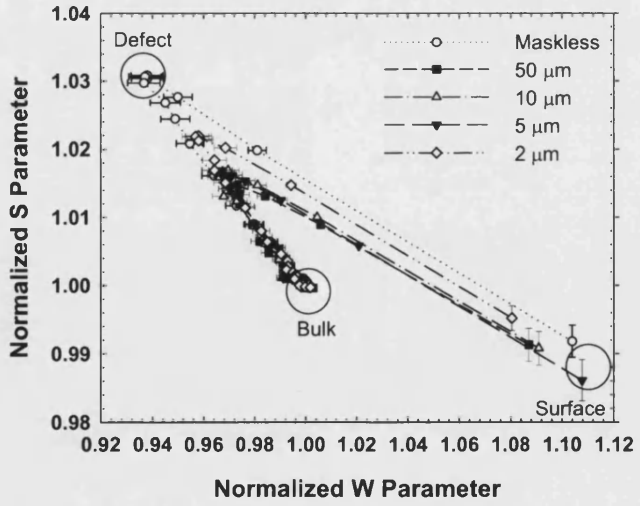

Figure 4.25 *S* versus *W* plots for the four masked samples and also the mask-less one as a reference.

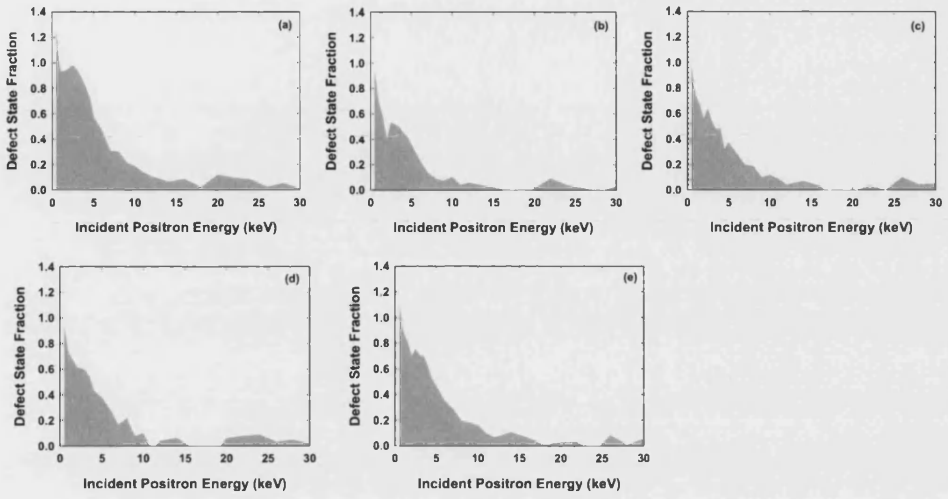

Figure 4.26 The fraction of the defect state in the measured samples (a) mask-less, (b) 50 μm mask, (c) 10 μm mask, (d) 5 μm mask, and (e) 2 μm mask.

The *S* parameter and the fraction of the defect state were fitted using VEPFIT [62] assuming two layer structure, a defected layer and a defect-free bulk layer. In fitting the mask-less sample, the fraction of the defect state was fixed to 100% in the defected layer while the other parameters (positron diffusion length and the upper boundary of the defected layer) were fitted. The obtained fitted values were then fixed in fitting the masked samples in order to get the *S* parameter and the defect state fraction. Fitting results of the *S* parameter and the defect state fraction are tabulated in the second and third columns of table 4.1. As the defects generated by the implanted ions are assumed to be divacancies (V_2), the defect state fraction is called V_2 fraction from this point onward. Both parameters, *S* and V_2 fraction, were then corrected for positron diffusion assuming that a fraction of the implanted positrons (*F*) is diffusing from the unmasked to the masked ridges and vice versa, and that the diffused fraction is proportional to the positron diffusion length (*L*) in each region. Thus if A is a masked ridge and B is unmasked one, then

$$F_{A \Leftrightarrow B} = \alpha L_{A,B} \tag{4.6}$$

where α is a constant equal to the number of positrons per unit length. The corrected *S* parameter and V_2 fraction are given in the third and fourth columns of table 4.1 and compared with the values before correction in figure 4.27. The ridge width in the different samples was corrected for positron diffusion accordingly using both *S* and V_2 fraction as shown in the last column of the table. Comparing the actual given values of the ridge width with the average obtained corrected values, it can be deduced that the mean undercutting distance of the diffused ions is about 300 nm. However, a percentage of this distance could still be due to a real diffusion of the defects.

Table 4.1 Fitting Results

ridge width	*S*	V_2 fraction	corrected *S*	corrected V_2 fraction	corrected ridge width (μm)	
(μm)	(%)	(%)	(%)	(%)	using *S*	using V_2 fraction
50	53.23	51.70	53.07	50.46	53.07	50.46
10	54.84	56.10	54.05	53.88	10.81	10.78
5	56.45	58.40	54.88	54.95	5.49	5.49
2	70.97	72.60	67.05	65.48	2.68	2.62

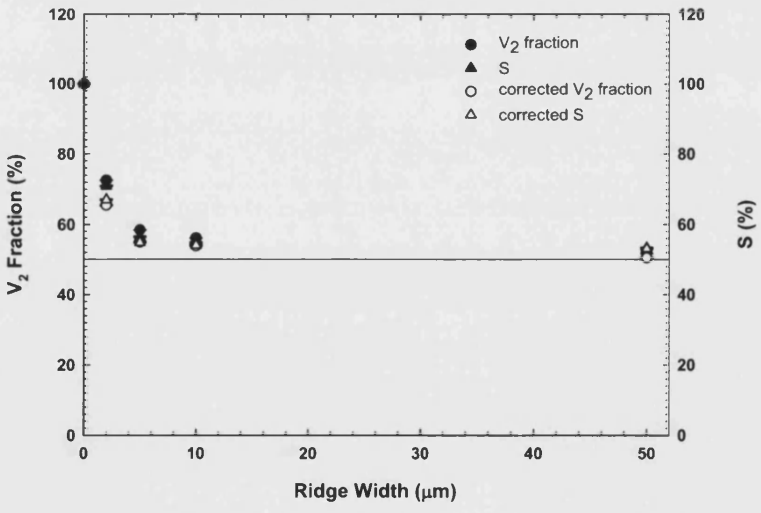

Figure 4.27 *S* parameter and V_2 fraction versus ridge width, before and after correction for positron diffusion. The horizontal line is the level expected for 50% implantation.

4.3.4 Conclusion

A simple method using specified implantation percentage has been proposed for studying the diffusion of vacancy-type defects at RT. The results showed no noticeable diffusion of the defects; however, they suggested an average distance of 300 nm for the undercutting caused by the diffusion of the implanted ions. It is believed that the method can still be valid for studying defect diffusion but perhaps narrower ridges (at least for the example studied here) and more precise masking are needed.

4.4 The Response of Open-Volume Defects in SiGe to annealing in Nitrogen or Oxygen Ambient

While the dynamics of thermal oxidation of Si has been adequately described for over three decades, details of SiGe oxidation are not entirely clear. In particular, the injection into the Si substrate of a super-saturation of interstitial defects during the formation of SiO_2 may not be replicated in the SiGe system. Here the response of relatively stable open-volume defects in a $Si_{092}Ge_{0.08}$ substrate to annealing at 900°C for 30 minutes is described in either an inert (nitrogen) or wet oxidizing ambient. The defects are initialized by He^+ implantation at an energy and dose of 60 keV and $1x10^{16}cm^{-2}$ respectively, followed by annealing in an inert ambient at 800°C for 10 minutes. Confirmation of the creation and thermal evolution of the open-volume defects was provided by beam-based variable-energy positron annihilation spectroscopy. The positron measurements suggest that the defects are considerably reduced in size following the secondary nitrogen annealing step. In comparison, the average size of the open-volume defects is reduced to a significantly smaller degree following secondary oxygen annealing. This result is consistent with a suppression of interstitial formation during oxidation, in contrast with the case for the thermal oxidation of silicon.

4.4.1 Introduction

Because of its superior features over Si, such as carrier mobility, silicon-germanium (SiGe) alloy has become increasingly attractive as a base in high-performance state-of-the-art microelectronic structures and devices, such as CMOS and HBT [81]. Hence, knowledge about the properties of SiGe alloys, particularly the oxidation mechanism, is required.

SiGe oxidation has been investigated recently in several studies. Spadafora et al. [82] and Napolitani et al. [83] examined dry oxidation kinetics of epitaxial SiGe films and SiGe on Si layers and compared the results with that of Si using several techniques, such as Rutherford backscattering spectrometry, transmission electron microscopy, and secondary ion mass spectroscopy. A Ge-rich defect-free layer was observed to be formed underneath the oxide layer, which is made mostly of SiO_2. This layer is believed to play an important role in reducing the interstitial injection during the oxidation process. Oxidation enhanced diffusion (OED) of some dopants such as boron, which is a result of interstitial super-saturation resulting during Si oxidation, was measured in the SiGe films and compared with the case of Si. A strong reduction of OED was observed, with respect to Si, indicating that the interstitials cannot reach the dopant region or are not produced at all, which is attributed again to a Ge-rich layer formed by the segregation of Ge beneath the oxidized layer. This phenomenon of interstitial super-saturation inhibition by Ge is a key element in the control of the electrical junction in many devices required by semiconductor technology.

A number of possible models have been proposed to describe the dynamics of SiGe oxidation [84]. Various parameters that could affect the oxidation process were discussed in these models; these include the comparison of Si-Ge and Si-Si bonds, the flux of Si and Ge at the oxidizing interface, the trapping or the oxidizing of Ge, and the incorporation of GeO_2 in the oxide.

In this study, the response of open-volume defects in $Si_{0.92}Ge_{0.08}$ to annealing in an inert nitrogen and a wet oxidizing ambient is presented.

4.4.2 Experimental Techniques

Samples studied in this work were Czochralski SiGe wafers with approximately 8% Ge ($Si_{0.92}Ge_{0.08}$). All samples were implanted with 60 keV He^+ ions at $1x10^{16}$ cm^{-2}. The mean projected range and the straggle of the He^+ ions, as calculated by TRIM code [30], are 460 and 114 nm, respectively. Samples were then annealed at 800°C in a nitrogen atmosphere for 10 min to create open-volume defects by out-diffusing the He^+ ions. Two of the samples were subjected to further annealing at 900°C for 30 min, one in nitrogen and the other one in wet oxidizing ambient.

Using variable-energy positron beam, positrons emitted from ^{22}Na radioactive source were moderated by a tungsten mesh, then accelerated and magnetically guided to be implanted into the sample with energies ranging from 0.1-30 keV. After the implantation, positrons thermalize and diffuse through the sample; a fraction is efficiently trapped by any vacancies present or at the sample surface. The positrons, whether trapped or freely diffusing, eventually annihilate with surrounding electrons, predominantly emitting two 511 keV γ-rays. The energy spectra of the annihilation γ-quanta, which are Doppler-broadened around 511 keV as a result of the movement of the electron-positron annihilating pair, are collected at each incident positron energy using high-purity Ge spectrometer.

As a result of the low average electron density in vacancies compared with that of perfect material, positrons are sensitive to their presence. Thus, in Doppler-broadening spectroscopy the change in electron momentum distribution, caused by the presence of vacancies, is measured and parameterized by the sharpness and the wing parameters, *S* and *W*. *S* is defined as the ratio between the number of counts in a fixed central region of the annihilation peak and the total number of counts in the whole peak and, likewise, *W* is the ratio of counts in the wings of the peak to that of the whole peak.

Generally, the S (W) parameter increases (decreases) with the presence of vacancy-type defects, as positrons trapped in the defects preferentially annihilate valence electrons, which have low momentum, and therefore a smaller broadening of the annihilation line and higher (lower) S (W) will be observed.

The experimentally-measured S parameter is the weighted average of that for positrons annihilating in the bulk (S_b) and those trapped by vacancy-like defects (S_d), and for one defect type is expressed as

$$S = F_d S_d + (1 - F_d) S_b \tag{4.7}$$

where F_d is the fraction of positrons that are annihilated in the defects, given by

$$F_d = \kappa / (\kappa + \lambda_b) \tag{4.8}$$

where κ is the trapping rate ($\approx i^{2/3} \nu c$, where ν is the specific trapping rate for mono-vacancies in Si = 5×10^{14} s^{-1} [9], i is the number of vacancies forming the vacancy cluster, and c is the number of defects per atom) and λ_b is the positron decay rate in pure defect-free Si (= 4.54×10^9 s^{-1} [9]). The factor $i^{2/3}$ implies that the specific trapping rate is proportional to the cross sectional area of the cluster. κ can be calculated from the positron diffusion length in defected and defect-free materials, L and L_+, respectively, where

$$L = L_+ \sqrt{\lambda_b / (\lambda_b + \kappa)} \tag{4.9}$$

From these expressions the concentration of defects and their characteristic S parameter (S_d) can be determined easily.

4.4.3 Results and Discussion

Figure 4.28(a) shows the variation of the S parameter as a function of incident positron energy (E) for the SiGe sample implanted with 60keV He^+ ions at $1 \times 10^{16} cm^{-2}$, before

and after annealing at 800°C for 10 min in a nitrogen atmosphere. The data for the unimplanted sample are also shown for comparison. All S values are normalized so that the bulk value S_b =1. The mean penetration depth of the positrons in the sample (z) is also shown in the figure where $z = 40E^{1.6}/\rho$ nm, ρ is the material density in g.cm^{-3}, and E is in keV. It is known that He^+ implantation creates vacancy-type defects in the specimen, and this is evidenced here by the increase in the S parameter above the S_b value (unity) for positron energies below ~16 keV. The measured S of 1.024 is lower than the characteristic value of divacancies (V_2), ~1.04, which are the predominant type of defects induced by ion-implantation (see, for example, ref. [77]). This is probably due to the passivation of the vacancies by He^+ ions [85]. Annealing of the defected sample in an inert ambient leads to out-diffusion of the He^+ ions, in-diffusion and agglomeration enhancement of the defects; leading to the formation of vacancy clusters. Small voids having S = 1.064, obtained by fitting the data using the computer program VEPFIT [62], were observed in the case of our sample. This value is associated with hexavacancies (V_6), according to the characteristic S values for vacancy clusters V_X for x = 2 to 5 for measurements taken using a spectrometer with 1.44 keV resolution [78]. Whether the vacancy clusters are really V_6 or are bigger but passivated by interstitials, or decorated by impurities like oxygen, giving S value lower the actual one because of the annihilation events taking place at the internal surfaces of the clusters, is still under debate [86].

The response $S(E)$ to secondary annealing in oxygen or nitrogen of the vacancy clusters induced by He^+ implantation and annealing is presented in Figures 4.28 (b) and (c). The response of the S parameter after etching the oxidized layer, using HF, is also shown in the figures; this had a more significant effect on the nitrogen-annealed data, presumably because a somewhat thicker oxide formed on the oxygen-annealed sample; however, no further etching was carried out because the first etch was sufficient to reveal all the relevant features of the two sets of data. It can be straightforwardly seen that the S parameter decreases slightly upon annealing in oxygen and significantly after annealing in nitrogen, almost reaching the bulk value (unity) in the latter case. This reduction in S could be explained by either a decrease in

the size of the clusters or/and a decrease of their concentration. However, with the aid of the code VEPFIT it was clear that this reduction is definitely a result of shrinkage of the clusters rather than reduction of their concentration.

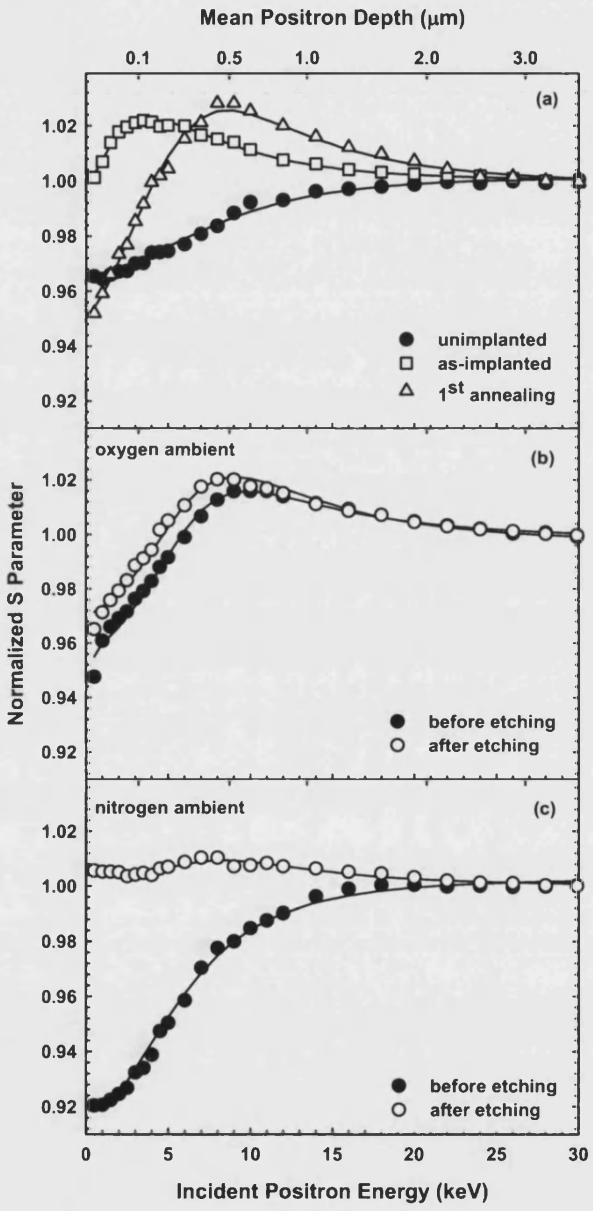

Figure 4.28 *S* parameter versus incident positron energy and mean implantation depth for $Si_{0.92}Ge_{0.08}$ wafers (a) unimplanted, implanted with He^+ at 60 keV and $1x10^{16}$ cm^{-2}, and after annealing at 800°C for 10 min in nitrogen; (b) after secondary annealing at 900°C for 30 min in oxygen ambient, and (c) after secondary annealing at 900°C for 30 min in nitrogen ambient.

The fitting results of the S parameter and the positron diffusion length in the defect layer of the samples annealed in oxygen and nitrogen together with that of post-implantation annealed sample are summarized in table 4.2. Using equations (4.7), (4.8) and (4.9), the characteristic S parameter of the open-volume defects (S_d) formed in each sample and their concentration (C_d) are computed. From the resulting values (shown in table 4.2) it could be inferred that thermal treatment in oxygen or nitrogen ambients leads to a reduction in the size of the vacancy clusters while their concentration stays more or less constant. It is apparent that this effect is much more pronounced after annealing in nitrogen, where the decrease in S parameter from 1.064 to 1.018 corresponds to shrinkage of the clusters' size from V_6 to V_1. The implication that the defect size falls to V_1 must imply that defect exists as some form of complex rather than an isolated monovacancy, which would not survive at room temperature. The consistency between the fitted S parameter and diffusion length (L) in the defected layer was checked according to the relation

$$S = S_d - (S_d - 1)(L / L_+)^2 \tag{4.10}$$

The two parameters showed good consistency, verifying the interpretation of the results and confirming that it is the size of the clusters that is decreasing and not their concentration.

Table 4.2 Fitting results of the S and L parameters of the defect layer in the three SiGe samples; after the first annealing in nitrogen and after the secondary annealing in oxygen and nitrogen. The obtained values for the characteristic S parameter of the defects (S_d) and their concentration (C_d) are also given. Uncertainties: S values ± 0.002, L ± 5nm, C_d ± 2x10^{17} cm^{-3}.

	after 1st annealing in nitrogen	after 2nd annealing in oxygen	after 2nd annealing in nitrogen
S	1.064	1.045	1.018
L (nm)	123	133	177
S_d	1.076	1.055	1.027
C_d (cm^{-3})	7.2x10^{17}	7.9x10^{17}	9.2x10^{17}

As pointed out in the introduction and observed in several studies in Si, Si interstitials are generated at the SiO_2/Si interface during thermal oxidation and injected into the substrate, where they find their way to the voids or clusters, as their internal surfaces act as an efficient sink of the interstitials [87-89]. Therefore, the empty volume of the clusters decreases and lower *S* parameter is measured. This scenario, as stated in various studies (for example [82]), is not applicable in the case of SiGe oxidation in dry ambient, where Si is selectively oxidized leaving Ge behind to pile-up at the SiO_2/SiGe interface, resulting in suppression of interstitial injection and thus little or no reduction in the size of the voids. Our results, showing a much smaller decrease in the size of the voids after wet oxidation compared with annealing in nitrogen, confirm the inapplicability of interstitial injection during the wet oxidation of SiGe. The larger effect after annealing in nitrogen may be associated with the presence of the native oxide on the sample surface.

An alternative VEPAS approach, namely the use of the *S-W* map, was also used to probe the nature of the vacancy clusters [90]. There are points on an *S-W* map associated with specific annihilation states (e.g., pure bulk SiGe, each defect type). Three plots are shown in figure 4.29 for the three annealed samples, after the post-implantation annealing in nitrogen and after the second annealing in oxygen and nitrogen. It can be seen clearly that the three plots lie on three different straight lines connecting the surface and the defect annihilation states and on a single line connecting the defect and the bulk states. This implies that the implanted positrons are annihilating from three different sites with (*S,W*) points characterizing the defect layer. The fitted (*S,W*) points suggest that the V_6 vacancy clusters created after the first annealing in nitrogen shrink after further annealing in nitrogen or oxygen, most likely to V_1 and V_4, respectively. Makhov and Lewis [52] show that the stable vacancy clusters V_3, V_4 and V_5 can result from the combination of V_6 with interstitials.

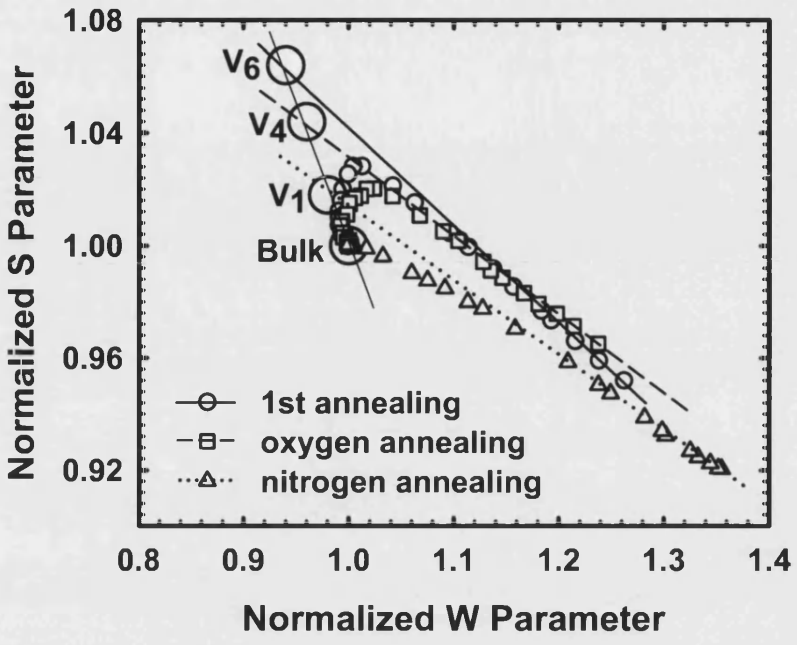

Figure 4.29 *S* versus *W* plots for the SiGe samples after the first annealing in nitrogen and the secondary annealing in oxygen and in nitrogen ambients.

4.4.4 Conclusion

We have studied the response of vacancy clusters in $Si_{0.82}Ge_{0.08}$, induced by He^+ implantation and annealing, to annealing in nitrogen and wet oxidizing ambients. The results showed reduction in void size, probably from V_6 to V_4 after the oxidation process and to V_1 following the annealing in nitrogen ambient. This result is contrary to what is known in pure Si, where oxygen has bigger effect on the shrinkage of the voids as the injected interstitials during oxidation can easily diffuse and fill-up the empty volume of the voids and diminishing their size. The contradiction between the response of voids to annealing in nitrogen or oxygen ambient in SiGe and Si is believed to be due to the presence of Ge and its suppressing effect of the interstitial injection into the substrate.

Chapter 5

Fluorine-Vacancy Complexes in Si and Si-SiGe-Si

This chapter focuses on the formation of fluorine-vacancy (FV) complexes and their role in retarding boron (B) transient enhanced diffusion (TED) in both Si in the first section and Si-SiGe-Si structure in the second section. The capability of positron annihilation spectroscopy in investigating internal electric fields in the depletion regions in semiconductor structures is also discussed in the first section.

5.1 FV Complexes in Ultra-Shallow Boron-Implanted Si

In this study, shallow FV complexes in Si have been directly observed using VEPAS and secondary ion mass spectrometry (SIMS). The FV complexes, introduced to combat the deactivation and transient-enhanced diffusion of ultra-shallow boron, were observed in pre-amorphized Si wafers implanted with 0.5 keV B and 10 keV F ions at a dose of 10^{15} cm^{-2}, and then annealed isothermally at 800°C for times ranging from 1 to 2700 s. The results are in agreement with a model which predicts that the complexes are of the form $F_{3n}V_n$, with n most probably being 1 and/or 2.

Besides the detection of FV complexes, VEPAS has shown ability to monitor changes in internal electric fields in the depletion regions in semiconductor structures.

5.1.1 Introduction

Interest in the beneficial consequences of implanting F ions in Si has grown in recent years as defect engineering has been developed to meet the continuing challenges of device miniaturisation. The application of particular interest here concerns ultra-shallow B implantation into pre-amorphized Si regrown via solid-phase epitaxy (SPE); efficient activation of the B while limiting its diffusion is the key to the formation of ultra-shallow junctions. Recent work by Cowern et al. showed that F in B-implanted Si can form clusters that trap interstitals (I) released from the band of end-of-range (EOR) defects, which in turn both retard the TED of B implants and significantly decrease their deactivation [91]. F co-implantation with B in Si was also examined by Kham et al. to gain better understanding of the mechanism by which F suppresses B TED [54]. In their study, SIMS profile of F shows a peak at half the projected ion range $R_p/2$, attributed to the formation of clusters of F with vacancies in this region, which become smaller and are eventually eliminated after annealing at high temperatures and long times.

The formation of FV complexes has been proposed in other studies as a likely candidate for the physical mechanism through which boron TED is reduced, acting as traps for the Si interstitials which enhance the diffusion. Recent studies have included experimental positron annihilation spectroscopy [92,93] and secondary ion mass spectrometry [91,94,95] as well as *ab initio* calculations [96,97]. Model of ~2-3 F atoms in FV clusters [91,92] was found to be plausible assumptions in explaining experimental results, whilst various F_nV_m (for n=2m+2, with up to 4 vacancies and an F:V ratio between 4 and 2) energetically-favourable configurations were proposed theoretically [96,97].

5.1.2 Experimental Procedure

VEPAS is used here to probe the nature of the complexes formed by the implanted F ions. The technique has been used successfully to identify FV complexes in thermally-treated F-implanted Si [92,93]. VEPAS in the single-detector mode

measures the Doppler broadening of the 511 keV γ-ray annihilation line, whose extent is determined by the average momentum of the electrons at the annihilation site. The broadening is characterized by the line-shape parameter *S*, which is defined as the central fraction of the 511 keV line. *S* for a chosen experimental set-up has a characteristic value for each annihilation site - for example, for pure bulk Si or for each specific vacancy-type defect, the latter being strong positron traps. The mean depth z of positrons implanted with energy E (keV) is determined from the relation $z = 17.2E^{1.6}$ nm. SIMS measurements were performed to determine atomic profiles.

Samples used in the study were n-type ⟨100⟩ Cz Si wafers with a resistivity of 10-20 Ω.cm. All wafers were first pre-amorphized with 30 keV, 10^{15} cm^{-2} Ge ions. Pre-amorphization is used to increase the activation and suppress channeling of dopant ions, especially light ions like B. The amorphized samples were implanted with 0.5 keV B ions at 10^{15} cm^{-2}. A second set of wafers was additionally implanted with F ions at 10 keV and 10^{15} cm^{-2}. This energy places the projected range of the F ions between the B implants and the amorphous-crystalline interface created by the Ge implants. After restoring the amorphous layer to crystallinity via the SPE regrowth process at 650°C, the samples were annealed isothermally using rapid thermal annealing in a N_2 atmosphere at 800°C for a range of times between 1 and 2700 s.

5.1.3 Results and Discussion

Figure 5.1 compares the variation of the *S* parameter, normalized to a value (= S_b) of 1.00 for bulk Si, with the incident positron energy for the samples implanted with B ions only, and with B followed by F ions. In both cases, there is an apparent difference in the *S(E)* curves for the incident positron energy in the range ~ 5 - 20 keV. This is due to the electric field in the depletion region, which extends from the p-type near-surface region, doped by B implantation and annealing, into the bulk of each n-type doped sample. Owing to the low doping level in the wafers used in this experiment (~10^{15} cm^{-3}), the depletion regions extend to quite large depths, between 150-350 nm. Electric field values in this region, extracted using a

linear-graded junction approximation, lie in the range $-9x10^{16}$ to $-3x10^{16}$ Vm^{-1}. Under these conditions, VEPAS data are only weakly sensitive to the B diffusion depth. Thus, although F does significantly influence B diffusion, the main impact of the F implants on our VEPAS results occurs through the introduction of F-related defects.

Before discussing the results from the formation of FV complexes point of view, the investigation of internal electric fields in the samples will be considered first in the next subsection.

5.1.3.1 Investigation of Internal Electric Fields

In addition to the powerful role of VEPAS in the field of defect characterization, it has been employed here to monitor internal electric fields in the depletion regions in semiconductor structures. In studying the samples described above, we have detected depletion regions of widths between 150-350 nm, centred at depths between 250-350 nm, with electric field values in the range $-9x10^{6}$ to $-3x10^{6}$ Vm^{-1}. The depth and width of the depletion regions increase significantly for annealing times greater than 100 s, attributed to B diffusion. The results are consistent with simple theoretical estimates, but the uncertainties on the latter are large.

Because of the importance of acquiring quantitative information on *p-n* junctions and depletion regions for designing and developing submicron sized semiconductor devices, VEPAS has been employed in early studies to investigate electric fields and their influence on positron diffusion. Electric fields applied to Au/Si and Au/GaAs systems [98-100] were shown to drift positrons back to the metal-semiconductor interface. Internal electric fields in Si have been also found to act as barriers against positron diffusion [101]. The effect of internal electric fields on the fraction of positrons drifted to the metal-semiconductor interface in Au, Al and Ni/GaAs systems and annihilated there have been also examined by Shek and co-workers [102]. Moreover, PAS has been applied to study the transients of defect deep levels in the band gap of semiconductors, where the annihilation properties of the positrons are used as a sensor of the transition of the electric field inside the depletion region, resulting from changing of defect charge states [103].

Figure 5.1 (a) shows the influence of internal electric fields on positron diffusion for samples implanted with 0.5 keV and 10^{15} cm^{-2} B ions and annealed at 800°C for different time intervals. Measurements on samples annealed for other times have been performed but are not shown in the figure for clarity. As mentioned earlier, the difference between $S(E)$ curves in the positron energy range 5-20keV is attributed to different electric fields only; where the curves can be fit, using the code VEPFIT [62], with all parameters fixed except the field position and magnitude. It is assumed that any trapping associated with the ultra-shallow B implant has either been annealed or acts as an extended surface region. There is expected to be a field arising from band-bending at the surface which tends to push positrons into the sample; however, fitting the raw data did not require this field to be included, suggesting that it plays a negligible role in determining the positron response. It could be that the field exists over a distance short enough to allow significant tunnelling to the surface, or that the extended-surface model is correct and the surface field merely pushes the positrons back into it. We shall return to this issue below.

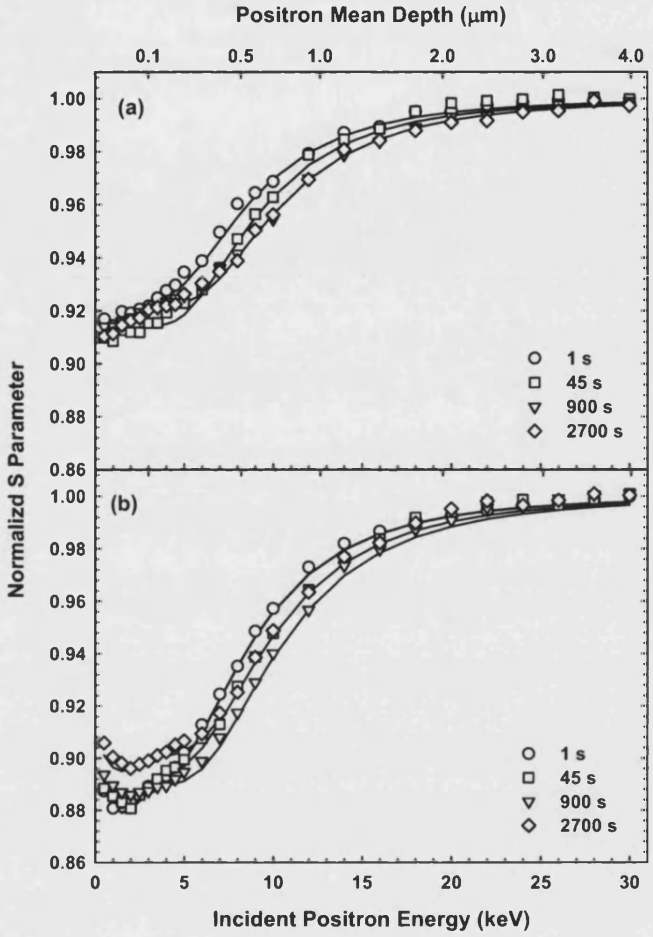

Figure 5.1 (a) Normalized *S* parameter versus incident positron energy and positron mean depth for samples implanted with 0.5 keV, 10^{15} cm^{-3} B ions and annealed at 800°C for different annealing times. (b) Corresponding results for a second set of samples in which F has been co-implanted at 10 keV at 10^{15} cm^{-3}. The solid lines are fits to the data obtained using VEPFIT.

The fitting model (as shown in figure 5.2) assumes a variable linearly-graded junction, with a constant electric field across it, sandwiched in the B-implanted Si wafers between a highly-doped thin layer of 20 nm and a field-free *p*-type region from one side and a field-free *n*-type wafer bulk from the other. The *S* parameter was fixed to the surface value S_s in the first thin layer and to the bulk value $S_b = 1$ in all other layers. The boundaries of the depletion regions were fitted with electric fields varying in the range from $-9x10^6$ to $-3x10^6$ $V.m^{-1}$. These values of electric field were computed using the dopant profile gradients suggested by SIMS [91];

the fitting was relatively insensitive to the size of the field, depending only on the positions and widths of the depletion regions. As it can be seen from the fitting results presented in figure 5.3, the depletion region is widening (extending from ~ 130 to 350 nm), as a result of B diffusion, with increasing annealing time while their centre is almost unchanged at ~ 220 nm for short (<100s) annealing times, stepping up to ~ 300 nm for longer annealing times. While these results are of the same order of magnitude as those suggested by simple theoretical estimates of region centres and widths, both these estimates depend on extensive extrapolation of SIMS data in [91], with consequently large uncertainties.

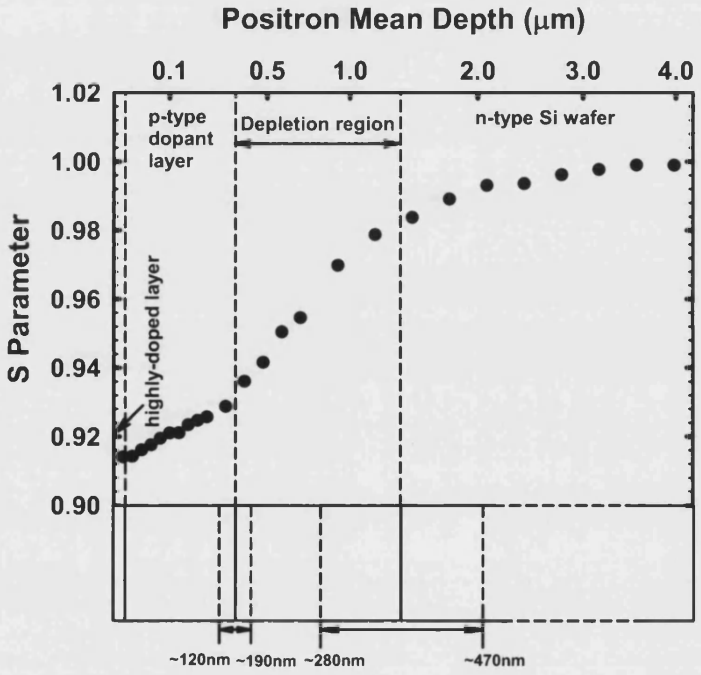

Figure 5.2 Schematic representation of the four regions assumed in the model used for fitting the data.

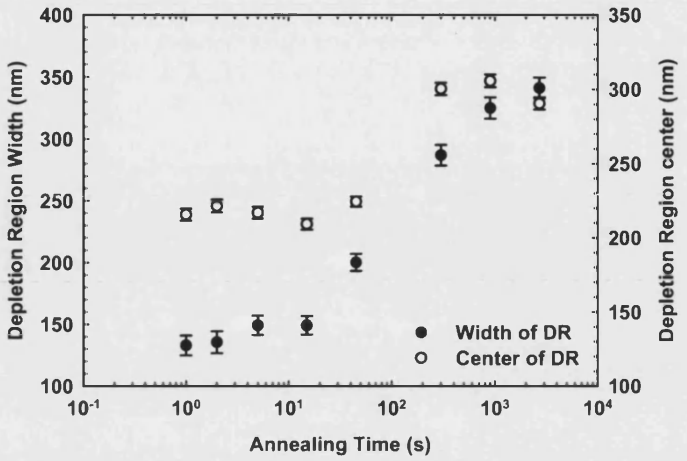

Figure 5.3 Annealing time dependence of the depletion region (DR) properties, width and centre, for samples implanted with B ions only.

The behaviour of the *S* parameter shown in figure 5.1 (a) was compared with that of similar samples additionally implanted with 10 keV F ions at 10^{15} cm^{-2} in figure 5.1 (b). Because of the low background doping level of the substrate (10^{15} cm^{-3}), the effect of F on retarding B diffusion and hence bringing the junction shallower was not observed; and fitting of the data revealed depletion regions with more or less the same properties as in the samples implanted with B ions only. However, the effect of the electric fields on positrons in these samples is observed in drifting them to a vacancy-like defect layer, probably F-vacancy complexes, with $S = S_d < S_s$ rather than to the surface as in the case of the samples without F. The slight variation of the measured *S* in the near surface region in the samples without F is possibly owing to the efficiency of the different electric fields in drifting the positrons to the surface. In the F co-implanted samples, this variance is not seen clearly as the drifted positrons are strongly getting trapped in the defected layer.

The small increase of the *S* parameter observed for some samples at very low implantation energy (< 1keV), both implanted with B ions only and those implanted with B and F ions, is believed to be due to unthermalized positrons diffusing back to the surface (see Figure 5.1 (b)). However, this effect is much reduced because of the electric field in the thin highly-doped near-surface layer arising from band bending at the surface [104]. In the case of the samples without

F (and thus without defect trapping sites), positrons are more likely to have the ability to overcome the potential barrier and reach the surface, whereas in the F co-implanted samples they are confined by the surface and the internal electric fields, directing them to the vacancy-like defect layer. In the latter case, the fraction of positrons reaching the surface increases with increasing annealing time, suggesting a decrease in the vacancy-like defect concentration. This observation is significantly pronounced after annealing for 2700 s.

A noticeable 'kink'-like feature in all the S(E) curves at ~ 4 - 6 keV positron energy (two curves at different annealing times are shown in figure 5.4 as an example). The 'kink' position for each sample, with the aid of VEPFIT, was found to be consistent with the deep boundary of the depletion region. This feature arises from the drifting of the implanted positrons across the depletion regions, by the internal fields, and it could be used as a good indication for the position of the deep boundaries of depletion regions in the wafers.

An arbitrary parameter χ proposed by Knights and Coleman [105] as a measure of the sensitivity of the measured junction depth is calculated here for samples implanted with B ions only and plotted against junction depth in figure 5.6. The junction depth is measured as the constant width of the highly-doped thin layer plus the variable width of the p-type doped layer, and the χ parameter is obtained from the integration of the $S(E)$ curves (Figure 5.1 (a)) in the positron energy range from $E = 0$ to 15 keV with the constant area below $S = 0.91$ subtracted. A linear relationship is shown in the figure for the range of the measured junction depths which agrees with the dependence found in [105].

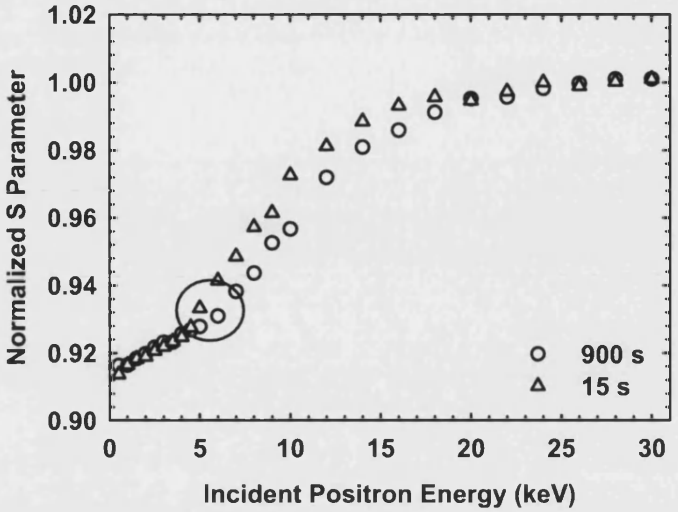

Figure 5.5 Two examples of 'kink'-like feature observed in *S*(E) curves. The feature is consistent with the deep boundary of the depletion region in the samples. The two curves are for samples implanted with B ions and annealed at 800°C for 900 and 15 s.

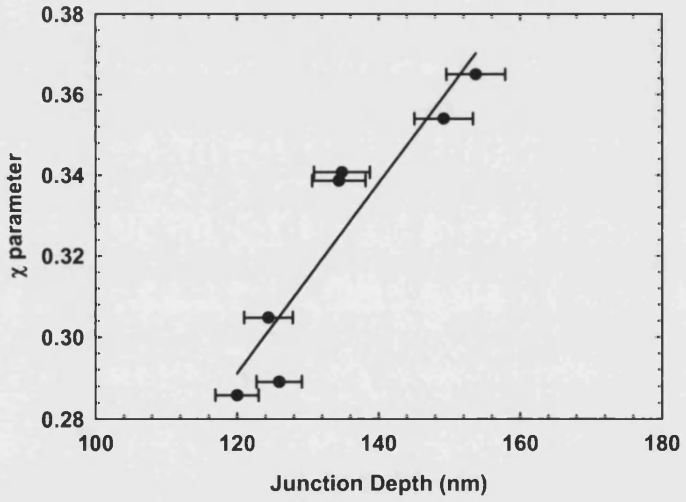

Figure 5.6 χ parameter versus junction depth as an indication of the sensitivity of the measured values of the junction depth. The χ parameter is obtained from the integration of the *S*(E) curves between E= 0 and 15 keV minus the constant area below *S* = 0.91, and the junction depth is the sum of the constant width of the thin highly-doped layer and the changing width of the *p*-doped layer.

5.1.3.2 F-V Complexes

The most significant difference between the *S* parameter behaviour of the sample sets with and without F is seen below a few keV incident positron energy. Figure 5.7 highlights this difference for a pair of samples from the two groups which have both been annealed at 800°C for 900s. In the sample without F, positrons with a few keV energy are drifted back to the surface by the electric field, and most are annihilated there with a low *S* parameter of $S_s \sim 0.91\ S_b$. However, the F co-implanted samples exhibit *S* values at a few keV which are lower than the surface value. This is due to the presence of a layer of FV complexes formed only in these samples, to which positrons are drifted by the internal electric field. The positrons are efficiently trapped by the high concentration of FV defects and so the *S* parameter characteristic of the defected layer S_d ($\approx 0.87\ S_b$, obtained using VEPFIT) will be measured, rather than S_s. The slight variation in the measured near-surface *S* in the samples without F (Figure 5.1 (a)) arises from the different efficiencies of the various internal electric fields in drifting the positrons to the surface. In the F-implanted samples (Figure 5.1 (b)) this small effect is overcome by the stronger effect of trapping in the defect layer with $S = S_d$.

While *S* is usually greater than S_b for vacancy-trapped positrons in Si, the proximity of F here means that the average electron momentum seen by the trapped positrons is higher than in bulk Si, and S_d is consequently lower than S_b. At very low implantation energies some of the positrons - a fraction of which may be unthermalized - will have the ability to diffuse to the surface, evidenced by the small increase in the measured *S* value below ~ 1keV; this fraction is, however, much reduced because of the electric field in the thin highly-doped near-surface layer arising from band bending at the surface [104]. This surface field region is so thin that some positrons are still able to penetrate the potential barrier. In the case of the samples without F, barrier penetration and reaching the surface is more likely because the positrons have longer effective diffusion lengths, in the absence of the FV layer sink, and approach the barrier more often. The electric fields at the

surface and across the depletion region combine to direct positrons towards the FV layer, thereby enhancing the sensitivity of VEPAS to the defected layer.

Pi et al. [93] and Simpson et al. [92] measured *S* parameter values for FV complexes of 0.90 and $0.92S_b$ for samples annealed at 700°C (for 43 h) and 650°C (for 30 min), respectively. These results are consistent with the present value of $0.87S_b$ for samples annealed at 800°C (for 1 – 900 s). The correlation of *S* value and annealing temperature suggested by these results is consistent with the progressive evolution of F_xV_y defect structures towards that observed in the present work, in which the average ratio *x*:*y* is increasing, possibly but not necessarily because of the annealing of co-existing V_y defects.

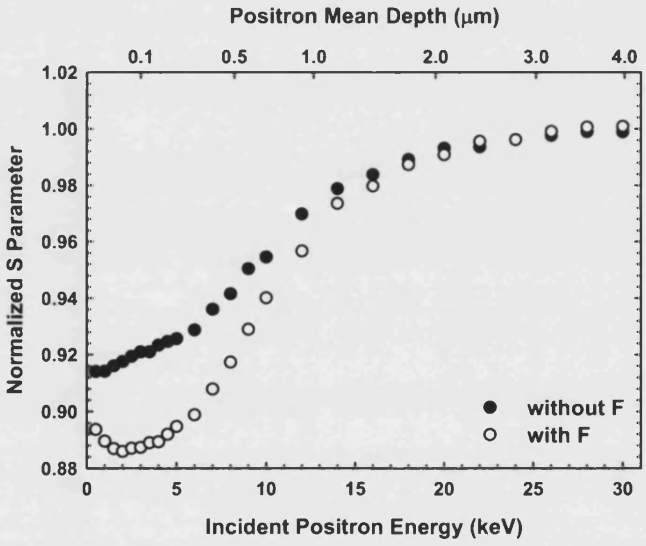

Figure 5.7 Comparison between the *S(E)* curves of two samples, with and without F, annealed at 800°C for 900 s.

As annealing time increases from 1 to 900s in the F co-implanted samples, the measured (fitted) *S* parameter of the defected layer stays almost constant, implying that the FV defect concentration remains high enough to trap all the positrons that are implanted into it with energies of a few keV. However, the low-energy ($E \leq$ 1keV) shapes of *S*(*E*) - as in figure 5.7 - suggest a decrease in the FV concentration with annealing time, as more positrons are able to diffuse to the surface and the

increase in S towards S_s becomes more pronounced. The SIMS profiles in figure 5.8 suggest that the decrease in FV concentration is particularly marked within the first 5nm or so beneath the surface. However, because of the small range of positron energies over which this behaviour is observed, and the complications associated with the non-thermalization of positrons implanted below ~ 1keV, it is not possible to draw quantitative conclusions from these curves.

After annealing for 2700s, the S parameter of the defected layer increases measurably to $0.89S_b$ (Figure 5.1(b)). Although this increase is accompanied by the expected small increase in diffusion to the surface, the latter only occurs at $E <$ 1.5 keV and VEPFIT is able unambiguously to attribute the increase in S to a decrease in defect concentration. Assuming that S_d for the FV defects, deduced from the data for annealing times up to 900 s, is 0.87 S_b, then the fraction of positrons trapped in the FV defect layer after annealing for 2700 s is given by

$$F = (1-0.89)/(1-0.87) = 0.85 \tag{5.1}$$

The trapping rate κ of the positrons in the FV layer in the 2700 s annealed sample is then

$$\kappa = \lambda_b F/(1-F) = 2.6x10^{10} s^{-1} \tag{5.2}$$

where λ_b the positron annihilation rate in pure bulk Si (= 4.54 x 10^9 s^{-1}) [106]. Now $\kappa = \nu C_d$, where ν is the specific positron trapping rate in s^{-1} ($\approx 3n$ x 10^{14} s^{-1}, where n is the number of vacancies in the defect structure [108]) and C_d is the defect concentration per atom. Thus $C_d = \kappa/\nu_1 = (8.6/n)x10^{-5}$ per atom, $\approx (4.3/n)x10^{18}$ cm^{-3}. The uncertainty on this number is ~ ± 25%, mostly arising from the uncertainty in the value of ν, and larger if the assumption that ν for an F_xV_y complex is similar to that for an unattached V_y is invalid. The SIMS profile measurements for F (Figure 5.8) yield an average F concentration in the first 40 nm after annealing for 2700 s of 1.31 x 10^{19} cm^{-3}, which is $3n$ greater than the defect concentration indicated by VEPAS. The defect structure suggested by the combination of VEPAS and SIMS is thus $F_{3n}V_n$. This is in agreement with the

theoretical prediction of Diebel and Dunham [97] and the experimental estimate from the diffusion study of Cowern et al. [91] from which it may be concluded that the most likely value(s) of n are 1 and/or 2.

Figure 5.8 also yields average F concentrations of 13.6 and 7.7×10^{19} cm^{-3} in the first 40 nm after annealing at 800°C to 15 and 120 s, respectively. These would correspond to $F_{3n}V_n$ concentrations $C_d = (4.5/n)$ and $(2.6/n) \times 10^{19}$ cm^{-3}, respectively, which, inserted into equation (5.2), yield trapped fractions F = 98.5 and 98%; this is in line with the assumption in the argument above that at shorter annealing times essentially all the positrons are trapped in the defect layer.

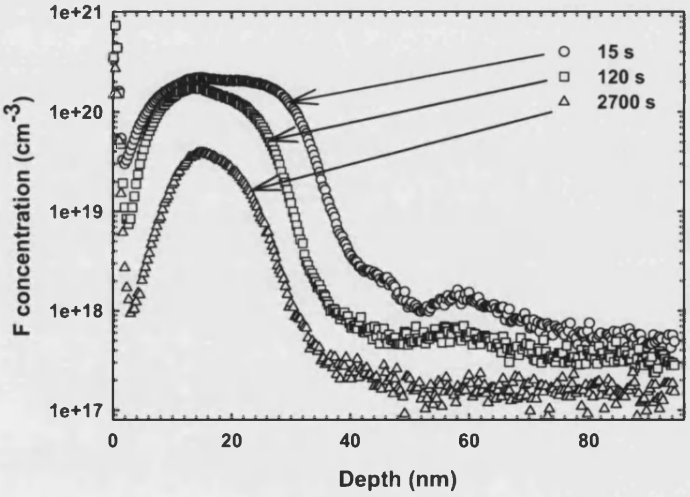

Figure 5.8 SIMS profiles of F in samples implanted with 0.5 keV, 10^{15} cm^{-2} B and 10 keV, 10^{15} cm^{-2} F and annealed at 800°C for 15, 120, and 2700 s.

5.1.4 Conclusion

The results presented in this section provide evidence that the nature of the F-related defects introduced beneath the ultra-shallow B implant is vacancy complex $F_{3n}V_n$, most likely F_3V and/or F_6V_2. The vacancies trapped by the F atoms are in turn able to trap the interstitials migrating from the EOR region and thus significantly reduce the B diffusion, as observed by Cowern et al. [91]. VEPAS

and SIMS results indicate that the concentration of the complexes, to within 25%, decreased from $(4.5/n)$ to $(2.6/n)$ $x10^{19}$ cm^{-3} between 15 and 120 s annealing times at 800°C, but drop significantly to $(4.3/n)x10^{18}$ cm^{-3} after annealing for 2700 s.

Beside the powerful role of VEPAS in detecting FV complexes and providing quantitative details about their nature, we have shown that this technique can also provide quantitative information about the depletion regions in semiconductor structures. However, the results were relatively insensitive to the magnitude of electric fields across these regions.

5.2 FV Complexes in Si-SiGe-Si Structures

In this section, FV complexes have been directly observed in the $Si_{0.94}Ge_{0.06}$ layer in a Si-SiGe-Si structure, using VEPAS. These complexes are linked to the significant reduction of boron diffusion in the SiGe layer via interstitial trapping. Vacancies were introduced into the samples by ion implantation with 185keV F^+ at doses in the range between $9x10^{14}$ and $1x10^{16}cm^{-2}$; the samples were subsequently subjected to rapid annealing in nitrogen ambient at 950°C for 30s. The VEPAS results, in combination with F profiles obtained by SIMS, suggest that the FV complexes associated with the SiGe layer take the form $F_{4n}V_n$ and that they preferentially accumulate at the Si/SiGe interfaces. Their concentration is critically dependent on annealing temperature, decreasing significantly after annealing at 1000°C.

5.2.1 Introduction

As mentioned in the previous section, F as an implant in Si has been the subject of extensive studies [44,54,108,109] because of its effectiveness in retarding the TED of boron, the key for achieving ultra-shallow junctions and consequently miniature Si-based devices. In contrast, there is little knowledge to date on the behaviour of F in SiGe. SiGe is a promising material in microelectronic technology, especially in the fabrication of heterojunction bipolar transistors (HBTs). While some studies

have been performed using PAS to investigate vacancy-type defects and their complexes in SiGe layers [110], none has focussed on F in SiGe structures, to the author's knowledge. In this work we report results on the use of VEPAS to investigate the behaviour of F in a layered structure of Si-SiGe-Si analogous to that used in HBTs.

5.2.2 Experimental Procedure

Low pressure chemical vapour deposition at 850°C (growth A) and 800°C (growth B) was used to grow boron marker layers for monitoring boron diffusion. The growth A samples comprised an undoped silicon layer, a 50nm $Si_{0.94}Ge_{0.06}$ layer with a peak boron concentration of $5x10^{18}$ cm^{-3}, and an undoped silicon cap layer. The growth B samples comprised an n-type silicon layer, a 40nm $Si_{0.94}Ge_{0.11}$ layer with a peak boron concentration of $1.2x10^{19}$ cm^{-3}, and an n-type silicon cap layer. Thus the type A samples form an i-p-i structure, whereas the type B samples form an n-p-n structure. Some of the type A and type B samples were then implanted with P^+ ions at 288keV and $6x10^{13}$ cm^{-2}. Type A samples were implanted with 185keV F^+ ions at a dose of either $9x10^{14}$ or $1.85x10^{15}$ cm^{-2} and type B samples were implanted with 185keV F^+ ions at a dose of either $2.3x10^{15}$ or $1x10^{16}$ cm^{-2}. All samples were then subjected to rapid thermal annealing in a nitrogen ambient at 950°C for 30s. As-implanted and as-grown samples were also produced as controls.

Positrons in the energy range 0.5 - 24keV were implanted into the samples to enable depth profiling from the surface to ~ 2.5μm. As positrons enter the material they rapidly thermalize then diffuse until they either annihilate freely with electrons or are trapped by vacancy-type defects and eventually annihilate via two γ rays in approximately opposite directions and 511keV energy. Doppler broadening of the 511keV annihilation line, resulting from the momentum of the annihilated electrons, is measured with a high-purity Ge detector and characterised by the simple line-shape *S* parameter, defined as the fraction of counts in a central region of the annihilation line.

The concentration depth profiles of ^{74}Ge and ^{19}F were measured using SIMS.

5.2.3 Results and Discussion

Figure 5.9 presents the variation of the *S* parameter, normalized to a value of unity for the bulk material, with the incident positron energy *E* for the four samples implanted with 185keV F^+ ions at $1x10^{16}$ (n-p-n), $2.3x10^{15}$ (n-p-n), $1.85x10^{15}$ (i-p-i), and $9x10^{14}$ cm^{-2} (i-p-i) after annealing at 950°C for 30s. None of the samples had P^+ implants. The behaviour of the as-grown sample (type B) is also shown as a reference. The mean depth (*z*) probed by the positrons with energy *E* (keV) is also shown in the figure, where $z \approx 17.2\ E^{1.6}$ nm. *S*(*E*) curves for the as-implanted samples (see e.g. figures 5.10 and 5.11) show no enhanced vacancy response in the SiGe layer. After annealing, *S* parameters below the bulk value, S_b, were measured in all samples for a mean depth up to ~ 0.9μm, being most marked between ~ 0.06-0.2 μm in the samples implanted with the two highest F doses and deeper (between ~0.2-0.6 μm) in the two lowest-dose samples ($9x10^{14}$ and $1.85x10^{15}$ cm^{-2}). The survival of vacancies after annealing, and the observation of *S* values below unity, is attributed to the accumulation of F_xV_y complexes in specific regions; this behaviour was observed earlier by Pi et al. [93] and was attributed to the presence of F in the vicinity of the vacancies; it is well known that annihilation with F electrons leads to a reduction in the vacancy *S* parameter [67]. El Mubarek et al. linked F_xV_y complexes with the mechanism underlying B thermal diffusion reduction in similar samples [111].

The difference in the position of the dip in *S*(*E*) -3.5 and 6 keV for the samples implanted with the highest and lowest two F doses, respectively- can be understood in terms of the presence of electric fields in the highest-dose samples (both n-p-n structures) and the absence of such fields in the two lowest-dose samples (i-p-i). In the former case the field drifts the diffusing positrons to the SiGe layer from both sides, thereby enhancing the sensitivity of VEPAS to the FV complexes formed there. In the latter case a greater fraction of the implanted positrons sense the damage beneath the SiGe layer and, therefore, a broader response is observed centred at around 6 keV, corresponding to depths close to the

peak of damage caused by 185keV F^+ (~0.3 μm, as calculated by TRIM [30]). In a study of similar samples using SIMS and transmission electron microscopy (TEM), El Mubarek et al. observed deep F peaks in the same range in SIMS profiles and concluded that these were due to F trapping at dislocation loops together with defects at the growth interface [111]. Therefore, in summary, the dip in $S(E)$ at ~ 3.5 keV corresponds to F_xV_y complexes in the SiGe layer, and the broader dip at ~ 6 keV to F_xV_y complexes principally in the Si beneath the SiGe layer.

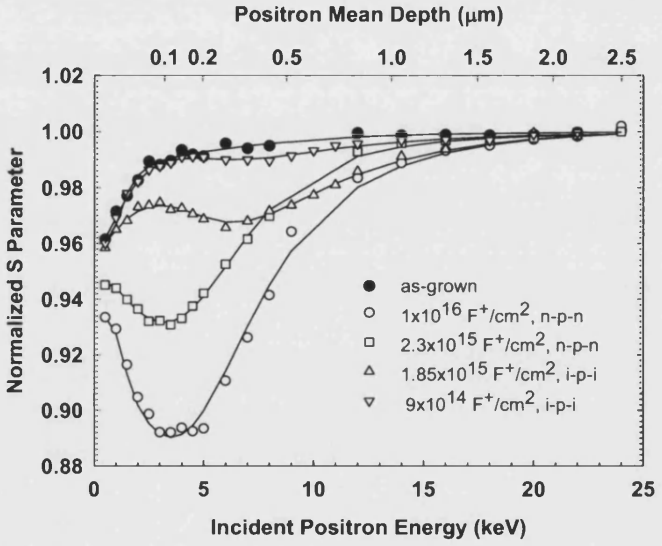

Figure 5.9 *S* parameter versus incident positron energy for samples implanted with 185keV F^+ at $1x10^{16}$, $2.3x10^{15}$, $1.85x10^{15}$, and $9x10^{14}$ cm^{-2}, and annealed at 950°C for 30s. The data for an as-grown sample is also shown. The solid lines are fits obtained using VEPFIT.

$S(E)$ data for two of the samples are shown in figures 5.10 and 5.11 with F^+ implants only and with F^+ and P^+ implants. The n-p-n samples in figure 5.10 were implanted with $2.3x10^{15}$ F^+ cm^{-2} and the i-p-i samples in figure 5.11 with $1.85x10^{15}$ F^+cm^{-2}. In figure 5.10 positrons can detect more FV complexes in the SiGe layer when both F^+ and P^+ are implanted, a lower S parameter being measured in the latter case. The extra complexes are formed because P-implantation introduces additional vacancies and, as there is excess F at this dose, F can associate with them. The fitted layer S parameters for the two data sets shown in figure 5.10 suggest an increase in vacancy concentration in the SiGe layer of approximately

20% when P^+ ions are implanted, a figure which matches well the increase in F concentration in the layer according to SIMS.

For the i-p-i sample implanted with P^+ and $1.85x10^{15}$ F^+cm^{-2}, (figure 5.11), the P-implantation overdopes the intrinsic regions in the i-p-i structure, converting it to an n-p-n structure. This introduces an electric field which makes the positrons less sensitive to the defects in the Si layer beneath the SiGe and consequently more sensitive to those in the SiGe layer, where again the slightly lower *S* value implies that more FV complexes are formed there if P is implanted. Accordingly, it can be inferred that P-implantation increases FV clustering in the SiGe region as well as positron sensitivity to the clusters.

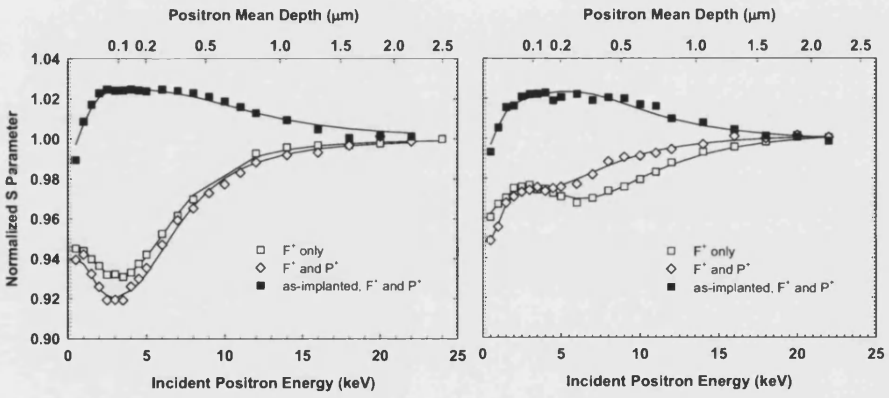

Figure 5.10 Comparison between the behaviour of the n-p-n sample implanted with $2.3x10^{15}$ F^+cm^{-2} with and without P^+ implants. Data for the as-implanted sample (with F and P) is also shown as a reference.

Figure 5.11 Comparison between the behaviour of the i-p-i sample implanted with $1.85x10^{15}$ F^+cm^{-2} with and without P^+ implants. Data for the as-implanted sample (with F and P) is also shown as a reference.

VEPAS data were also recorded for the $1x10^{16}$ F^+ cm^{-2} sample with and without P-implantation (not shown here). Exactly the same *S* parameter was measured, implying saturation positron trapping in the FV defects in both cases, so that the extra vacancies introduced by P^+ implantation resulted in no change in VEPAS response.

The *S*(*E*) data for the as-grown sample in figure 5.9 exhibits an increase from its surface value to the bulk with a notably short diffusion length. This could be

attributed to defects in or at the interfaces of the SiGe layer acting as a barrier against positron diffusion to the surface.

The solid lines behind the data points in the figures are fits obtained using VEPFIT [62]. The samples are modelled as layered structures; electric fields in the near-surface region resulting from band bending and of $+2x10^3$ and $-1x10^3$ Vcm^{-1} in the Si layers on each side of the SiGe layer were incorporated in the model to fit the P-doped samples. While the fitting was relatively insensitive to positron diffusion lengths, sensible self-consistent fits were always achieved. As the F dose increases the S parameter associated with the SiGe layer, S_{SiGe}, decreases from 0.995 to 0.878, as more FV clusters reside there; saturation trapping is believed to be reached for the F dose of $1x10^{16}$ cm^{-2}, so that the S parameter characteristic of the FV complex, S_d, is ~0.88. This is consistent with the author's and others' earlier measurements in Si [43,92,93]. While the cap Si layer could be fitted with bulk (defect-free) Si parameters, the Si layer beneath the SiGe, extending to 0.6 μm could not; a region centred at ~ R_P exhibits fitted S values which imply a combination of F-related defects which could include FV complexes in the vacancy-rich zone, F-interstitial (FI) defects in the I-rich zone beyond R_P, and F agglomerates and precipitates around R_P (as seen in Si in ref. 6). In the i-p-i samples, positrons are not drifted to the SiGe layer and are thus more sensitive to the F-related defects in the underlying Si layer; this explains the observation of a lower S parameter in the raw data for 1.85×10^{15} cm^{-2} F dose than in the data for the higher F dose of 2.35×10^{15} cm^{-2} at ~ 10keV.

In an attempt to achieve an insight into the nature of the FV complexes the vacancy concentration C_v, derived from the VEPAS data, has been compared with the F concentration C_F, derived from SIMS data. C_v (in cm^{-3}) in the SiGe layer was calculated from the fitted S parameter in the layer, S_{SiGe}, as

$$C_v = 5x10^{22}\left[\lambda_b(S_{SiGe}-1)/v(S_d-S_{SiGe})\right] \qquad (5.3)$$

where λ_b is the positron annihilation rate in perfect Si (= 4.54×10^9 s^{-1}) [106] and ν is the specific trapping rate for positrons ($\approx 3n \times 10^{14}$ s^{-1}) in clusters of n vacancies [107].

Let us first consider a model in which the positron trapping sites in the SiGe layer are uniformly distributed throughout the layer. The average C_F over the layer, as obtained by SIMS, is between 20–50 times higher than C_v. This implies that either (a) some of the F may be forming FV complexes, such as the $F_{3n}V_n$ seen in Si [43] and that the rest (perhaps 85-95%) are left isolated or form F agglomerates or precipitates: or (b) all the F in the SiGe layer form precipitates and the positrons are trapped in vacancy-like defects on their surfaces. If all the positron trapping sites formed in the layer were precipitates, then trapping of positrons would become limited by their diffusion to the defect sites, in which case diffusion-limited trapping model would become important [112]. Using this model the concentration of precipitates N, can be estimated; for example, for our sample that is implanted with 2.3×10^{15} F^+/cm^2 $N \approx 10^9$ cm^{-3}, implying $\geq 10^{10}$ F per precipitate. These precipitates would be a few μm in diameter, which is unreasonably large.

As uniform trapping throughout the SiGe layer seems unlikely, we turn to an alternative model. Interrogation of the F SIMS profiles such as that shown in figure 5.12 reveals that F could be accumulating at the two heterojunction interfaces between the SiGe and the Si layers (figure 5.12). The shallow F peaks were shown to be correlated with the reduction of boron thermal diffusion by El-Mubarek et al. [111]. The influence of defects on F profiles after annealing at temperatures above 500°C was observed in an early study of Si implanted with BF_2^+ [113]. In this work, gettering of F was observed in damaged regions and at the interfaces between crystalline and amorphous regions.

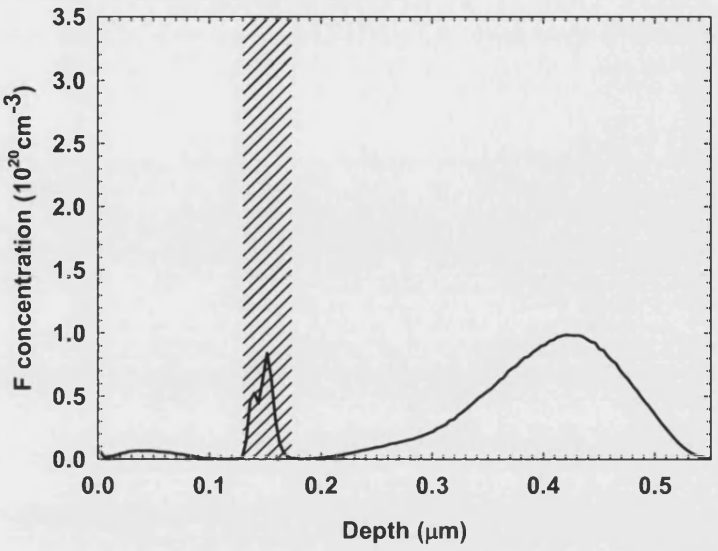

Figure 5.12 SIMS profile of F for the sample implanted with 185keV F^+ at 2.3x10^{15} cm^{-2} and annealed at 950°C for 30s. The shaded region indicates the full-width-at-half-maximum of the Ge SIMS profile, corresponding to the SiGe layer.

In light of these observations, VEPFIT was employed to fit the VEPAS data with the assumption that all of the FV defects associated with the SiGe layer are at the two heterointerfaces on each side of the layer. For the sample implanted with 1.85x10^{15} F cm^{-2}, VEPFIT gave interface S parameters corresponding to a total C_v of 7.5x10^{18} cm^{-3}, approximately one quarter of the total C_F in the two interfaces from SIMS. This is consistent with $F_{4n}V_n$ complexes, not far from the $F_{3n}V_n$ complexes (with n most probably 1 and/or 2) proposed in the previous section [43] and other studies [92,93] in Si structures.

VEPAS and SIMS data for the region above the SiGe layer, and in F-implanted epitaxial Si control samples, suggest preferential migration of F towards the surface. This has been observed by Pi et al. [93] and also earlier by Jeng et al. [114] in samples implanted with 30keV F^+ at doses of 10^{12} and 10^{13} cm^{-2} and annealed for 30 min at temperatures between 300 and 1050°C. Jeng et al. [114] noticed anomalous rapid diffusion of F at temperatures higher than 550°C, and they suggested that this behaviour could be associated with temperature-dependent F complex formation.

Finally, two samples with SiGe layers (not identical to those used above) were implanted with 185keV F^+ at $2.3x10^{15}$ cm^{-2} and 288keV P^+ at $6x10^{13}$ cm^{-2}, then rapid thermal annealed for 30s at (a) 950°C and (b) 1000°C. $S(E)$ is shown in figure 5.13 for these samples as well as, for reference, an as-grown sample. FV complex formation is again evidenced by the low S up to ~0.7 μm. The increase in S after the higher-temperature anneal suggests a reduction in the concentration and/or size of the FV complexes; if one assumes only the former then this corresponds to a 40% reduction in defect concentration.

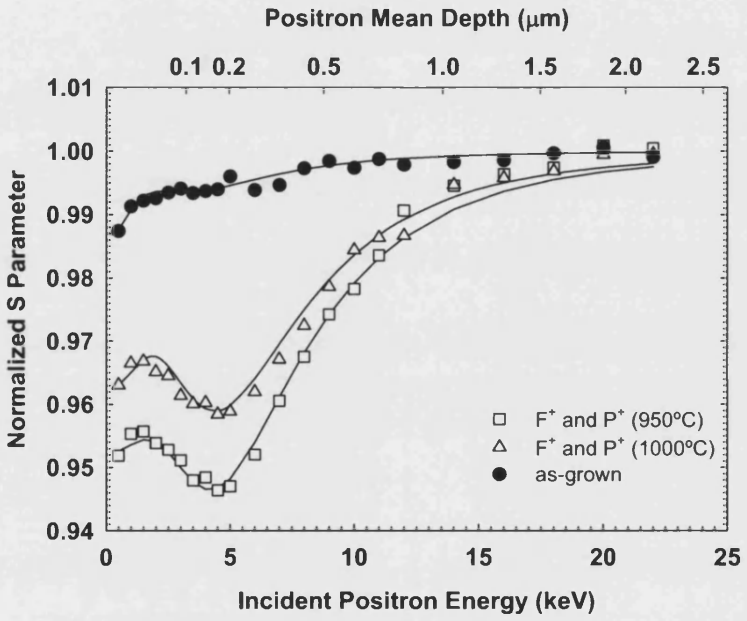

Figure 5.13 $S(E)$ curves for Si-SiGe-Si samples implanted with 185keV F^+ at $2.3x10^{15}$ cm^{-2} and 288keV P^+ at $6x10^{13}$ cm^{-2} annealed at 950°C and 1000°C for 30s. Data for an as-grown sample is shown as a reference.

5.2.4 Conclusion

This work has confirmed that VEPAS can be used directly to observe the formation of FV complexes in SiGe structures where F implantation has been shown to eliminate boron TED and reduce boron thermal diffusion – here, in Si-SiGe-Si structures implanted with F ions (at an energy chosen so that the SiGe layer lies within the vacancy-rich region of the fluorine damage profile) and rapid

thermal annealed. With the aid of SIMS it is suggested that $F_{4n}V_n$ complexes accumulate at the heterojunction interfaces. The VEPAS response to the FV complexes decreases if the annealing temperature is increased from 950 to 1000°C, suggesting that the efficacy of this method for boron diffusion reduction depends critically on annealing temperature.

Chapter 6

Vacancy-type Defects in Compound Semiconductors

The behaviour of open-volume defects in two types of III-V compound semiconductors is considered in this chapter. VEPAS has been employed to investigate the evolution of open-volume defects introduced by He^+ implantation in indium phosphide (InP). The obtained results are discussed in the first section. The second section concentrates on vacancies in gallium nitride (GaN) and the influence of magnesium (Mg) doping on their formation. VEPAS data are presented and compared with photoluminescence (PL) and optically-detected magnetic resonance (ODMR) results.

6.1 Evolution of Vacancy-type Defects in He^+-Implanted InP

The influence of He^+ ion implantation and subsequent annealing of Cz-InP has been investigated in this study using VEPAS. Three samples implanted with $1x10^{16}$, $5x10^{16}$, and $1x10^{17}$ He^+/cm^{-2} were studied in the as-implanted condition as well as after annealing at 640°C for a sequence of 5 minutes intervals. The characteristic line-shape parameter of the implanted region was noted to increase after 5 minutes annealing, then decline gradually with annealing for longer times until it reaches a value close to that of as-grown sample. This shows that vacancy-like defects can be created in InP by He implantation followed by a short time

thermal annealing at T > 600°C. Comparison of the results with a study where cavities observed in He implanted InP has been carried out.

6.1.1 Introduction

InP, being one of the III-V compound semiconductors, has been considered as an important material for the development of optoelectronic devices and, as a substrate material, semi-insulating InP is widely put into use. Because of the major role they play in the development of the III-V semiconductors device technology, defects, both in as-grown materials as well as those introduced by particle irradiation and ion implantation, in compound semiconductors have been an active field of study in recent years.

To the author's knowledge, only a few studies are available on investigating defects introduced by ion implantation in InP using PAS. Wei and co-workers have examined point defects generated by 60-keV Be^+ implantation into InP [115]. An increase in the vacancy-type defects concentration with the implantation dose was observed. Damage created by Si^+ ions, with energy of 0.6 and 3.0 MeV and doses ranging between 10^{11} and 10^{14} m^{-2}, implanted in Zn and S doped InP was investigated by Schultz et al. [116] and Simpson et al. [117] using slow-positron beam and Rutherford backscattering techniques. Reduction in the concentrations of vacancy-type defects after isochronal annealing up to 720 K was noted. Bulk lifetime and Doppler broadening measurements have been also employed to study defects induced by ion implantation of InP, example of these measurements is a study p-type InP crystals implanted with Ne^+ ions [118]. Other techniques, such as Raman scattering [119,120] and SEM [121] have been also used to investigate the effect of H^+ and He^+ implantation on InP.

In this work, VEPAS has been employed to study vacancy-type defects in He^+ implanted samples and compare the results with the work carried out by Chicoine et al. in studying similar samples [122]. In their work, Chicoine et al. studied InP samples implanted with He^+ ions of energy between 25 to 70 keV and doses in the range of $1x10^{16}$ to $9x10^{16}$ cm^{-2} and annealed subsequently at 600 to 750°C for a

time range between 5 and 25 minutes. Their study, using high-resolution x-ray diffraction (HRXRD) and cross-sectional transmission electron microscopy (XTEM) revealed that nanocavities of 4-50 nm diameter can be formed by He^+ implantation and subsequent annealing of the InP samples.

6.1.2 Experimental Procedure

The InP samples used in this study were grown using Czochralski technique and then implanted at low pressure (10^{-4}-10^{-6} Torr) with 70 keV He^+ ions of three different doses, $1x10^{16}$, $5x10^{16}$ and $1x10^{17}$ ions cm^{-2}. The growth and ion implantation of the samples were performed at the Institute of Electronic Material Technology (ITME) in Poland. Positron annihilation spectra of the as-grown sample as well as the as-implanted samples were measured.

The samples were then annealed isothermally at 640°C for between 5 and 40 min in 5-min steps. The annealing temperature of 640°C was chosen as the formation and evolution of a layer of buried cavities was observed at this temperature in Chicoine et al. study. Samples were arranged as a stack of four layers with each sample covered with another one and the top one covered with the as-grown sample, and the whole stack was placed in a ceramic tube inserted in an oven where the annealing process was performed under a flow of N_2 gas. The annealing temperature of 640°C was always reached and adjusted before inserting the samples in the oven. Positron annihilation spectra of the He^+ implanted samples after annealing at 640°C for 5, 10, 15, 20, 25, 30 and 40 min were recorded. Further annealing at 700°C was carried out for 10 and 20 min on the sample implanted with an ion dose of $5x10^{16}$ cm^{-2}.

VEPAS was performed using positrons with energies in the range of 0 to 30 keV in a beam of 8mm diameter.

6.1.3 Results and Discussion

The variation of the *S* parameter, normalized to the bulk value, with the incident positron energy for the three implanted samples before annealing is shown in figure 6.1. The behaviour of virgin (unimplanted) sample is also shown for comparison. As can be seen in the figure, helium implantation creates damage centres or defects which trap positrons and hence gives an *S* parameter value higher than the value of unimplanted bulk InP. An increase in the *S* parameter value for the sample implanted with $1x10^{17}$ He^+/cm^2 compared with the two lower doses samples can be noted. This indicates that more defects are created with increasing the implantation dose as has been observed in other studies [115].

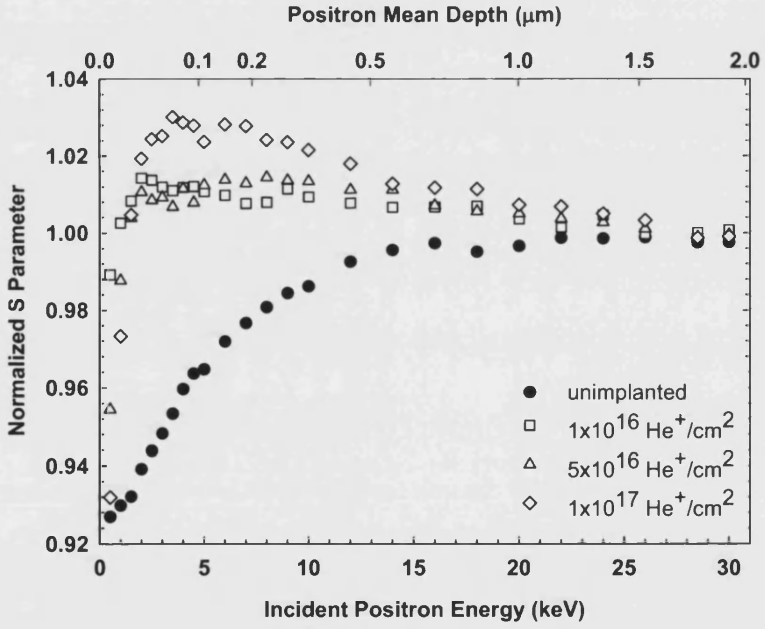

Figure 6.1 Normalized *S* parameter as a function of the incident positron energy for the three InP samples implanted with He^+ ions at $1x10^{16}$, $5x10^{16}$, and $1x10^{17}$ cm^{-2}. The behaviour of unimplanted sample is also shown as a reference.

The three graphs shown in figure 6.2 present the normalized *S* parameter versus incident positron energy for the three implanted samples after annealing for different times at 640°C. The behaviour of the as-implanted samples is also shown

for comparison. As can be seen in panel (a), after the first 5 min annealing of the samples *S* becomes higher than before annealing indicating that the distribution of the vacancy defects has changed in concentration or/and in size, the latter via the formation of vacancy clusters created as a result of the agglomeration of smaller defects during the annealing processes. Further annealing at 640°C results in a progressive reduction in defect's size and/or their concentration until they almost disappear after 45 min annealing at 640°C (or 20 min at 700°C in the case of $5x10^{16}$ cm^{-2} sample). A similar behaviour was observed in the $5x10^{16}$ cm^{-2} sample (panel (b)), but the increase in *S* after 5 min annealing was more pronounced. The annealing of the $1x10^{17}$ cm^{-2} implanted sample as can be seen in panel (c) showed no direct evidence of cluster formation, possibly because the implanted layer has flaked off after this high-dose implantation. According to these observations it can be said that the critical dose for forming large vacancy-type defects in 70 keV He^+-implanted InP is between $1x10^{16}$ and $5x10^{16}$ cm^{-2} with subsequent annealing for 5 min at 640°C. This is in agreement with the observations of Chicoine et al.

Another possible explanation of the increase in the *S* parameter after annealing the samples is the out-diffusion of the He from the defect sites which passivated the defects before annealing, as observed in other positron measurements of He^+-implanted semiconductors [123,85]. In this case, positrons do not see the vacancies created by the implantation as He^+ ions reside inside them, or do see them but annihilate with low *S* parameter because of the He ions' presence, but as samples are thermal treated, He ions out-diffuse from inside the vacancies and higher response in the *S* parameter is seen as more positrons annihilate in these vacancy-like defects.

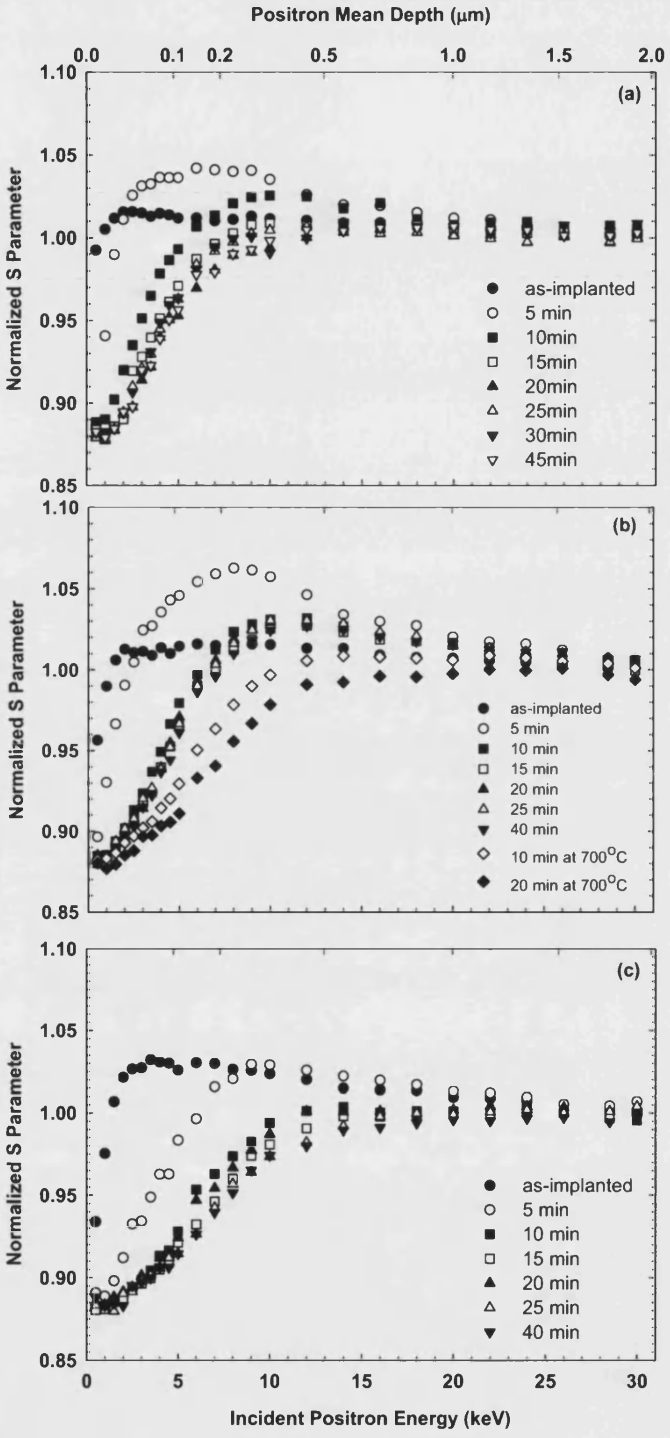

Figure 6.2 Comparison of annealing effect on the three InP samples implanted with 70 keV He^+ ions at (a) $1x10^{16}$, (b) $5x10^{16}$, and (c) $1x10^{17}$ cm^{-2}.

The measured S parameter versus incident positron energy curves were fitted using VEPFIT code [62]. An input model of defect distribution is fed to VEPFIT and used to calculate the fraction of positrons annihilated in different layers in the sample and the S parameter for each layer. S parameter is expressed as a linear combination of weighted contributions from S_s, S_d and S_b, the characteristic values of S for positrons annihilating at the surface, in defected layer, and in the bulk respectively

$$S(E) = S_s f_s + S_d f_d + S_b f_b \tag{6.1}$$

Where f_s, f_d, and f_b are the fractions of positrons annihilating at the surface, in defects and in the bulk, respectively.

A model comprising a defected layer composed of a 300 nm wide layer and a changeable-width buried layer has been assumed for fitting the data shown in figure 6.2. A sketch of this fitting model is shown below in figure 6.3. This fitting model has been chosen for the sake of verifying Chicoine et al. results where a buried layer of large cavities (4-50 nm diameter) was obtained. Their observations of 40 keV He^+-implanted InP have been scaled for 70 keV implanted He^+ ions and used in this model. Values of 0.484 and 112 nm are used here for the S parameter and effective diffusion length of positrons in unimplanted bulk InP.

The results of the as-implanted samples could not be fitted with the assumption of the existence of buried layer, implying that no cavities or large defects can be observed; this agrees well with Chicoine et al. observations. The as-implanted samples are therefore characterized by a single defected layer.

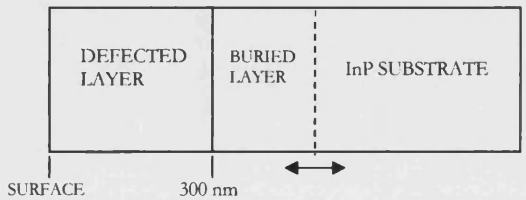

Figure 6.3 Schematic structure for the model used in fitting the data.

After the first 5 min annealing of the samples, the *S* parameter shows a significant increase and then declines with increasing annealing time. This can be explained by a short-time annealing enhancement of vacancy-like defect agglomeration, then as the sample is annealed for longer times the defects become smaller and/or less numerous until they no longer influence the measured *S* parameter value and the bulk InP value is approached. The reduction of defect size with increasing annealing time could be attributed to vacancy collapse after He^+ out-diffusion, which is also the case for the vacancies formed in the buried layer. The diffusion length of the positrons, obtained from VEPFIT, increased with increasing annealing time from ~10 to 90 nm. This increase could be due to an improvement of the near-surface structure after possible damage occurred by the implantation.

Assuming the model in which *S* is correlated with vacancy cluster size, the cluster size in the buried layer increases while the width of the layer decreases as annealing time is increased. This behaviour was also seen by Chicoine et al. for their sample implanted with 40keV He^+ ions at $3x^{16}$ cm^{-2}. For the $1x10^{16}$ He^+/cm^2 sample, the cluster size shows no further increase after the first 5 min annealing but the width of the layer decreased (from 120 to 20 nm) with increasing annealing time. However, the increase of the cluster size for the $5x^{16}cm^{-2}$ sample was more notable, where the maximum effect is after 25 min annealing. The layer width also decreased with increasing annealing time with a very short (~ 10 nm) effective diffusion length of positrons. Figure 6.4 illustrates the variation of the *S* parameter in the defected and buried layer with the annealing time for the samples implanted with $1x10^{16}$ and $5x10^{16}$ He^+/cm^2.

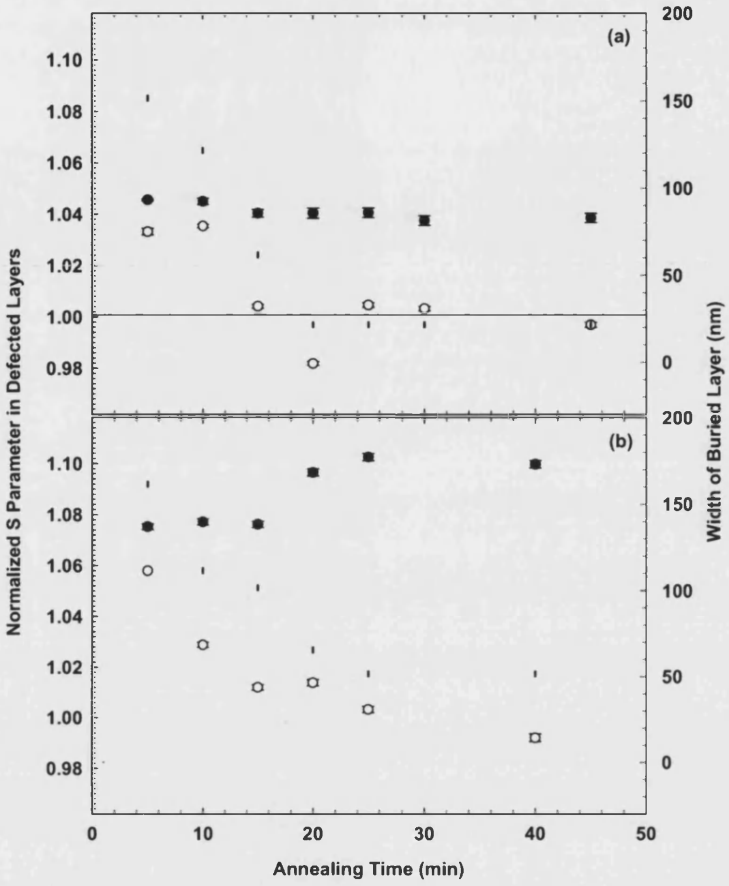

Figure 6.4 Normalized *S* parameter in buried layer (•) and first defected layer (○) as a function of annealing time for samples implanted with (a) $1x10^{16}$ and (b) $5x10^{16}$ He^+/cm^2 at 70 keV. The vertical marks show the variation of the buried layer width with annealing time. The horizontal line in (a) is the average *S* parameter in the first defected layer after 10 min annealing.

Depth profiling of the $5x10^{16}$ cm^{-2} sample, together with distribution of vacancies produced by implantation of 70 keV He^+ ions into InP substrate calculated by SRIM [30] are shown in figure 6.5 It can be noted that the maximum *S*-value coincides with the maximum concentration of vacancies and near the implanted ion range (400 nm). This was also observed by Chicoine et al. for cavities produced in an InP sample implanted with $3x10^{16}$ He^+/cm^2 at 40 keV. The decreasing of the buried layer width with the increasing of the *S* parameter as annealing time is increased can be noticed clearly in this figure.

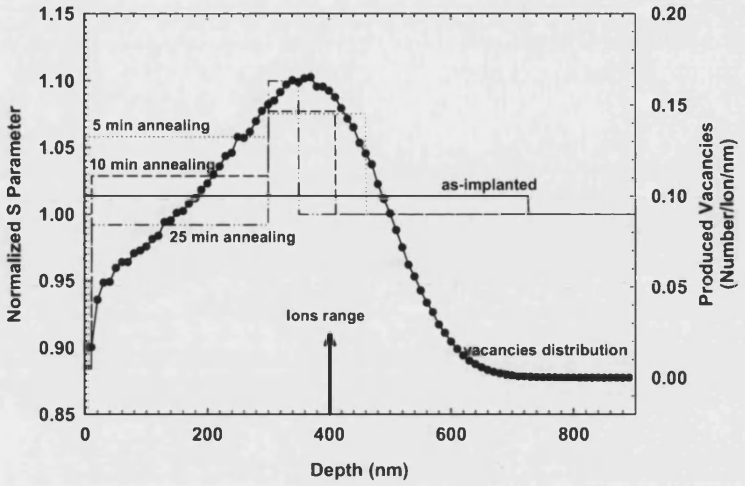

Figure 6.5 Depth profiling of the sample implanted with $5x10^{16}$ cm^{-2} He^+ ions at 70 keV. The arrow indicates the range of the implanted ions obtained using SRIM. Measurements with other annealing times are not shown here for the sack of clarity.

The sample implanted with $1x10^{17}$ He^+/cm^2 did not show a distinct increase in the *S* parameter value of the buried layer, but the width of the layer narrowed with increasing the annealing time. Figure 6.6 shows the variation of the *S* parameter with annealing time in the buried and defected layer.

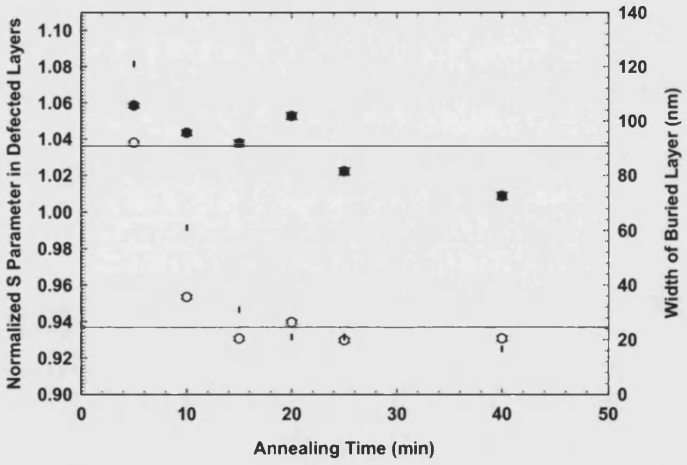

Figure 6.6 Normalized *S* parameter in buried (•) and first defected layer (○) as a function of annealing time for the $1x10^{17}$ He^+/cm^2 sample. The vertical marks show the variation of the buried layer width with annealing time. The horizontal lines are the average value of the *S* parameter in buried and defected layer after 5 min annealing.

From the data of the samples implanted with the three doses, it is clear that an ion dose of $5x10^{16}$ cm^{-2} can be considered as a critical dose for creating large vacancies or vacancy clusters in 70 keV He-implanted InP after annealing for 5 min at 640°C (see figure 6.7).

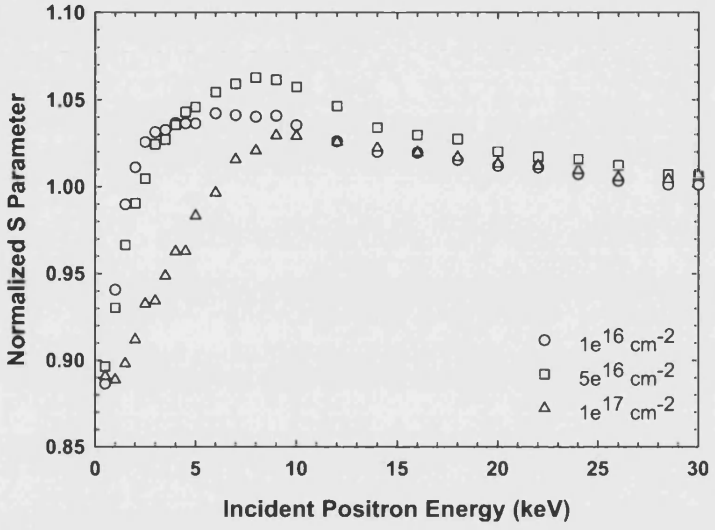

Figure 6.7 Comparison of the variation of the *S* parameter with incident positrons energy in the three samples implanted with $1x10^{16}$, $5x10^{16}$ and $1x10^{17}$ cm^{-2} after annealing for 5 min at 640°C.

Examples of fitted curves of the three He^+-implanted samples using the assumed model of two defected layers are shown in figure 6.8. The fitted *S* parameter was found to show an increase after the first 5 min annealing then a gradual decrease with annealing for longer times. This suggests that annealing the samples for short time leads to the formation of divacancies or larger vacancies, or, as explained earlier, annealing the samples out diffuses the He^+ ions from inside the vacancies so higher response in the *S* parameter is noticed. With increasing annealing time, the vacancy-type defects become smaller, and some of them are eliminated, until a constant low value of defect concentration is reached upon further annealing.

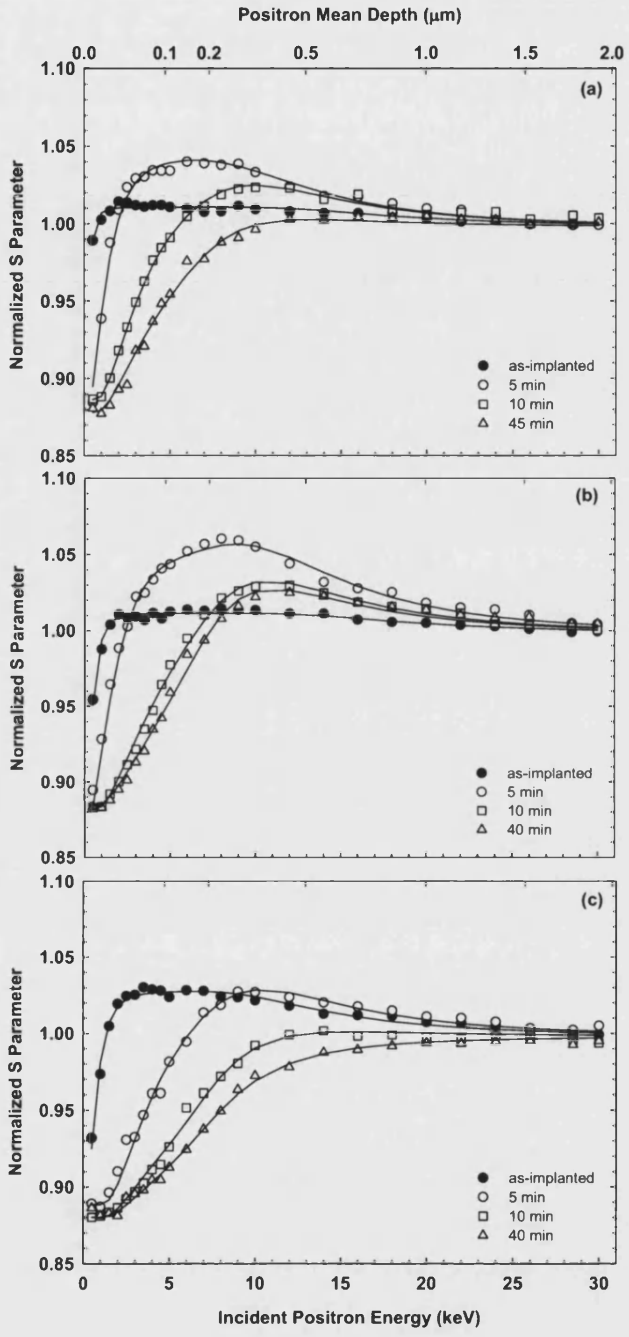

Figure 6.8 Normalized and fitted *S* parameter versus incident positron energy for selected measurements of the three implanted samples, (a) $1x10^{16}$, (b) $5x10^{16}$, (c) $1x10^{17}$ cm^{-2}, after the annealing process. The solid lines are the fit results obtained using VEPFIT. Other points which lie between the presented curves are not shown here for simplification.

The important question concerning Chicoine et al. results and those presented here is whether positrons are sensitive to the buried layer of cavities or whether they are seeing smaller vacancy clusters associated with the cavities. To address this question, attempts to fit the data with a single defected layer, without an existence of a buried layer, were performed. Good fits were achieved with a defected layer S parameter of ~ 1.06. Hence, it can be said that no direct evidence for an existence of a buried layer of cavities or vacancies can be deduced from our data. Insensitivity of positrons to such cavities or even larger pores has been addressed earlier by Potter and Coleman in Si samples implanted with He^+ ions [124]. This has been explained by the possibility that positrons are annihilating at the internal surfaces of the pores and hence near-bulk S parameters are measured rather than a high value associated with the pores.

The S-W plots for the sample implanted with $5x10^{16}$ cm^{-2} dose after annealing for 5 and 40 min at 640°C and for 10 min at 700°C are shown in figure 6.9. From these plots one can in principle determine how many types of defects are present in a sample. All the points on the three plots lie on one of the two straight lines; the line between the surface and the defect sites, or the second line connecting the defect and the lattice sites. Hence, there is no evidence in the S-W plots for the existence of cavity-like defects in the sample. S-W plots for the samples implanted with $1x10^{16}$ and $1x10^{17}$ He^+/cm^2 showed similar behaviour of this one implanted with $5x10^{16}$ cm^{-2}.

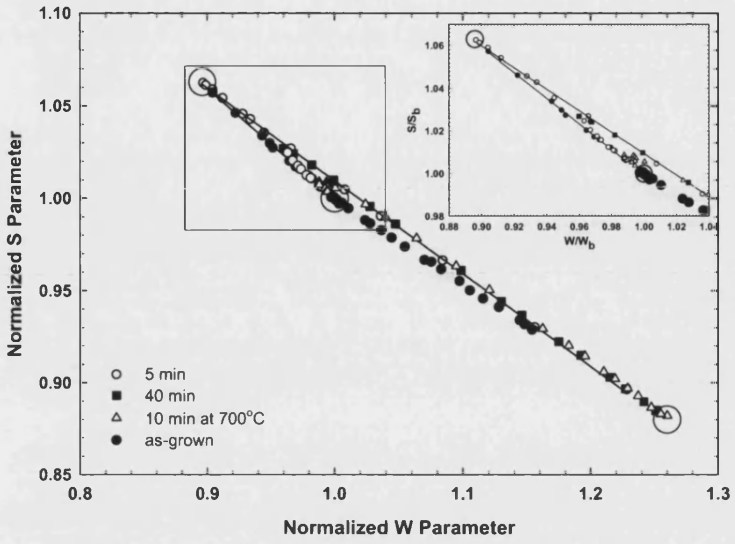

Figure 6.9 *S-W* plots for the sample implanted with $5x10^{16}$ He^+/cm^2 after annealing at 640°C for 5 and 40 min and at 700°C for 10 min. The circles indicate the possible annihilation sites. The square focuses on the defect site and it is enlarged in the top right corner.

Another parameter that has been measured is the peak-to-valley ratio. This is the ratio of the number of counts in the 511 keV annihilation peak to the number of counts in the valley region (approximately 300-500keV), as measured by a Ge detector. This ratio is directly related to the fraction of positrons forming positronium (Ps). The motivation of these measurements was to investigate the possibility that Ps would form in the buried cavity layer seen by Chicoine et al. No such evidence was found; however, this is not sufficient evidence to support the conclusion that no cavities exist, but rather, that they are not visible to positrons or positronium as discussed earlier. Lack of positronium has been also observed by Potter and Coleman in their study of pores in Si [124], from which they believed that positrons are only sensitive to the smaller defects between the pores and not to the pores or their surfaces.

The increase of the peak-to-valley ratio in the three He^+-implanted samples, as can be seen in figure 6.10, compared with the value of the as-grown sample, indicating that less Ps are formed after the He^+ implantation, can be understood by assuming that the as-grown sample has an open structure, enhancing Ps formation; however, as open-volume defects are introduced by He^+ implantation, positron trapping will

compete with Ps formation and hence reduce the amount of Ps and consequently increase the peak-to-valley ratio. Annealing the samples anneals away the positron traps and thus increases the probability of Ps formation until it reaches the level of the as-grown sample with longer annealing time (figure 6.11).

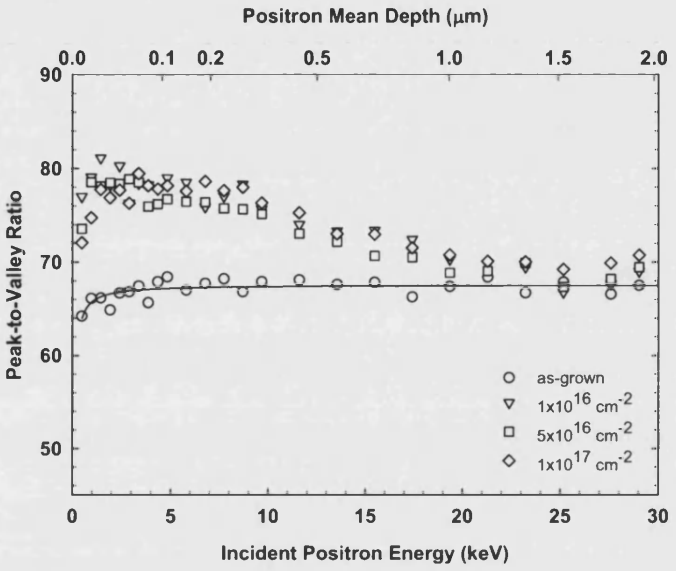

Figure 6.10 The variation of the peak-to-valley ratio with incident positron energy for the three He^+-implanted samples as well as the as-grown sample.

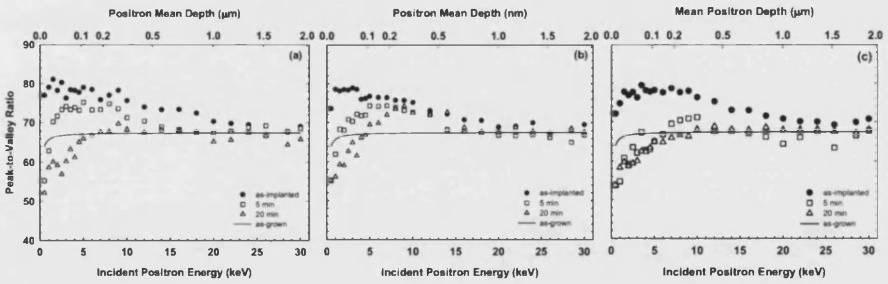

Figure 6.11 Peak-to-valley ratio versus incident positron energy for selected measurements of the three implanted samples, (a) $1x10^{16}$, (b) $5x10^{16}$, (c) $1x10^{17}$ cm^{-2}, in the as-implanted case and after annealing for 5 and 20 min at 640°C. Other measurements with different annealing times are not shown here as they showed behaviour similar to that of 20 min annealing. The solid line indicates the level of the as-grown sample.

6.1.4 Conclusion

PAS has been applied to study the effect of He^+ implantation into InP and the consequence of subsequent annealing. It has been shown that He^+ implantation creates defects in InP which increase in size and/or concentration with increasing implantation dose. A high *S* parameter was observed after annealing the samples for a short time at 640°C. This increase in the *S* parameter is attributed to the clustering of the small defects created by the implantation, or to passivation of these small defects by the implanted He^+ ions in the as-implanted samples which are eliminated by thermal treatment. The measurements suggest that $5x10^{16}$ cm^{-2} dose can be considered as a critical dose for creating vacancy clusters in 70 keV He-implanted InP. As in Si, it appears that VEPAS is not sensitive to the presence of large cavities in InP.

6.2 Vacancy-type Defects in Mg-doped GaN

PAS and optically-detected magnetic resonance (ODMR) techniques have been employed here to study undoped and magnesium (Mg)-doped gallium nitride (GaN). Vacancy-like defects associated with the red photoluminescence at 1.8eV have been detected in the doped samples and a strong correlation between the vacancy concentration and the intensity of the red band has been revealed.

6.2.1 Introduction

The considerable progress in GaN-based semiconductor technology, due to its promising properties such as the high thermal conductivity, during the recent years has led to the fabrication of high power devices and short wavelength light-emitting diodes and laser diodes [125]. Epitaxial GaN layers grown on sapphire substrates usually contain high densities of point defects, resulting from mismatch between the materials, which have a significant influence on the electrical and optical properties of the layer [126]. Doping of GaN with Mg introduces deep

defects, which control improvement of carrier concentration for applications such as laser diodes. Deep defects also play a key role in the performance limits and aging effects of GaN-based light-emitting devices. They also lead to photoluminescence (PL) at energies well below the band-gap. For example, the red (1.8 eV) luminescence band which is often observed in Mg-doped GaN has been suggested by various PL and ODMR studies [127-130] to be related to deep defects and appears due to recombination emission in which vacancy-dopant complexes are involved [127,129]. However, this proposal was based on indirect evidence and on previous experience of II -VI compounds; therefore further experimental confirmation is needed.

In the present study, both PAS and ODMR techniques have been employed on the same set of samples doped with a range of Mg concentration to investigate the influence of Mg doping on the vacancy formation in GaN. A correlation between the ODMR spectra, (obtained by monitoring the red PL) and the PAS results have been established in the study.

PAS, as an effective and non-destructive tool for studying vacancy-type defects in semiconductors, has been employed earlier to study GaN films. Ga vacancies (V_{Ga}) have been found to reduce in concentration when films are doped with Mg [131]. Oila and co-workers have observed high concentrations of V_{Ga} in undoped *n*-type GaN, whereas no V_{Ga} were detected in *p*-type doped with Mg [125,126]. In a study of GaN bulk crystals and epitaxial layers, V_{Ga} with concentrations of 10^{17}-10^{18} cm^{-3} were found in both types [132].

6.2.2 Experimental Procedure

The undoped and Mg-doped GaN samples were grown by metal-organic vapor phase epitaxy (MOVPE) at low pressure on *c*-plane sapphire substrates. The typical V/III ratio is ~ 2000 and the growth rate is ~2.3 μmh^{-1}. The Mg-doped layers were 1.5 μm thick and were grown at a temperature of 1047°C directly onto a thin nucleation layer of GaN grown at 525°C. The Mg concentrations in the layers were not determined directly but are expected to increase monotonically

with the precursor flow rate, which was 75, 100, 200 and 300 sccm. Some of the samples were annealed in a horizontal tube furnace at 850°C for 20 minutes in N_2 atmosphere with 0.5% O_2, after which *p*-type conductivity was exhibited by the samples.

The Mg-doped together with the undoped GaN samples were investigated with Doppler broadening measurements using a variable energy positron beam. Positrons were implanted into the samples at energies in the range 0.1-30 keV, corresponding to mean depths up to 1.5 μm, and the broadening of the 511 keV annihilation line was recorded with a HPGe detector. The annihilation line is characterized by the sharpness (wing), *S* (*W*), parameters, defined as the central (wing) fraction of the line. The value of *S* (*W*) is characteristic of the material under study, but is generally higher (lower) when vacancies are present as positrons trapped in vacancies have higher probability to annihilate with lower momentum electrons, leading to an increase (decrease) in the low (high) momentum *S* (*W*) parameter.

The same samples were also studied using the ODMR technique by the Bath optical spectroscopy group. ODMR is well established as a means of investigating centres involved in recombination processes in semiconductors [130, 128]. Our measurements were performed by detecting microwave-induced changes in spin distribution at magnetic resonance, via monitoring changes in the PL intensity. Microwaves at 14 GHz with ~ 50 mW power were used with the specimen at 2K. The incident microwaves were chopped at frequencies in the range between 300 Hz and 10 kHz and changes in the PL intensity caused by magnetic resonance were monitored as the applied magnetic field was slowly swept.

6.2.3 Results and Discussion

PAS results are presented in figure 6.12. The *S* parameter of the Mg-doped samples, along with that undoped reference sample, is shown as a function of incident positron energy. All *S* parameter values are normalized to the bulk GaN value (S_b). The corresponding mean depths probed by the positrons are also shown.

For the undoped sample, as the incident positron energy increased, the *S* parameter firstly decreases from the specific surface value (i.e., at low energy) and become approximately constant above 3keV, when almost all positrons are annihilated in the GaN film. The slight rise in *S* parameter between 3keV to 18keV is consistent with a previous report [133] which suggested that vacancies prefer to reside alongside dislocations, whose density increases towards the interface of the film and the nucleation layer. Beyond 18 keV, *S* falls towards the value characteristic of the sapphire substrate (measured separately to be $0.392/S_b$). For the Mg-doped samples, beside the decrease of the *S* parameter from its surface value at low energies, it shows a significant increase between ~ 5 and 20 keV (a mean depth of ~ 0.1 to 0.8 μm) after light Mg doping with 75 and 100 sccm. With increasing the Mg concentration, the *S* parameter decreases to reach a level close to that of the undoped sample after doping with 300 sccm. This suggests that Mg doping introduces vacancy-like defects in the GaN layer and their concentration decreases with increasing the Mg concentration.

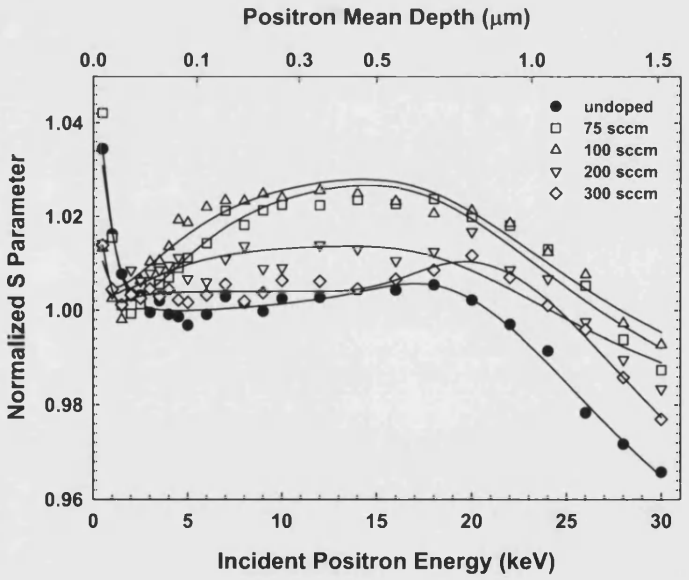

Figure 6.12 Normalized *S* parameter as a function of incident positron energy for four GaN samples doped with Mg at different flow rates. The behaviour of the undped sample is also shown for comparison.

Figure 6.13 shows S_b as a function of Mg concentration, where S_b (and W_b) is taken as the average of the S (W) parameter measured in the energy range from 12keV to 18keV and represents the bulk film value. The highest S_b value is observed for the most lightly-doped sample. With increasing Mg concentration, the S_b value decreases and approaches that of the undoped sample. The dependence of S_b on Mg doping is very similar to that of the red luminescence (shown also in figure 6.13) and of the ODMR signals detected in the red spectral region. This correlation thus provides strong support to the assertion that the red emission is associated with vacancy-type defects. Furthermore, the linear relationship between S_b and W_b shown in figure 6.14 is consistent with the existence of only one type of vacancy-related defect in the films.

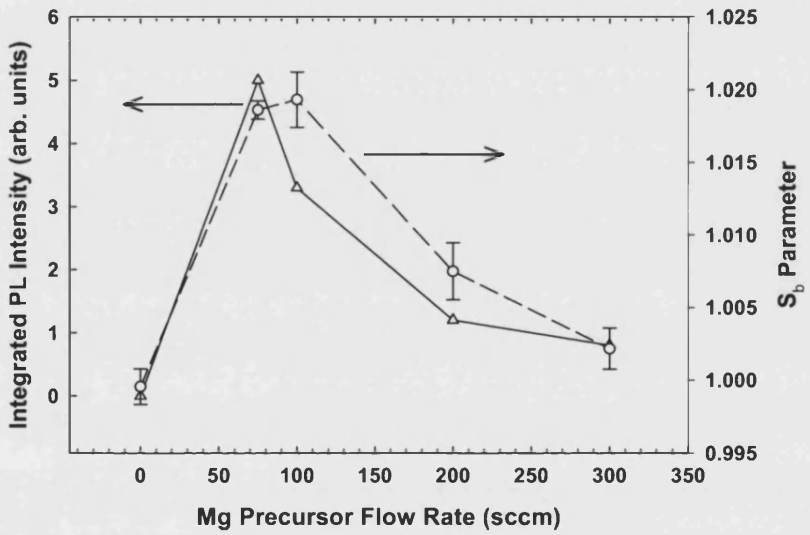

Figure 6.13 the change of S_b parameter (○) and the integrated intensity of the red emission (△) with Mg concentration. The lines are guides to the eyes.

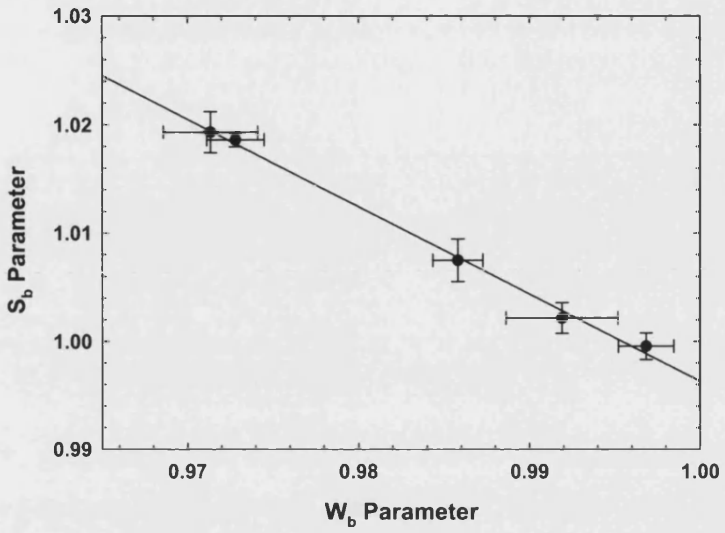

Figure 6.14 S_b versus W_b for the GaN samples doped with Mg at different concentrations as well as undoped sample.

If there is only one type of vacancies in the GaN layer, then their concentration (C_v) can be estimated as;

$$C_v = \frac{N_{at}}{\nu_v \tau_b} \frac{(S/S_b - 1)}{(S_v/S_b - S/S_b)} \tag{6.2}$$

where N_{at} is the atomic density, τ_b = 165 ps is the positron lifetime in bulk GaN [132], ν_v is the positron trapping coefficient at the vacancies = 1 x 10^{15} s^{-1}, and S, S_b, S_v are the measured S parameter and the characteristics S parameter in bulk GaN and in vacancies respectively. Using the above expression, the vacancy concentrations in the GaN layers were found to be in the range between 6x10^{16} and 1x10^{18} cm^{-3}, decreasing with increasing the Mg concentration in a trend similar to that of the S_b parameter shown in figure 6.13.

Reduction in the S parameter, indicating reduction of the vacancy concentration, has been observed after annealing in both the lightly (75 sccm) and the heavily (300 sccm) doped samples. The change in the $S(E)$ curves before and after annealing is shown in figure 6.15. It can clearly be seen that the effect is more

significant in the case of the lightly doped sample; the reason of this is not clear at the moment. A noticeable feature also is that the annealing leads to a decrease in the *S* parameter to a level slightly lower than that of the undoped GaN. This is probably indicates that some of the defects that are originally present in the undoped sample are removed at this stage.

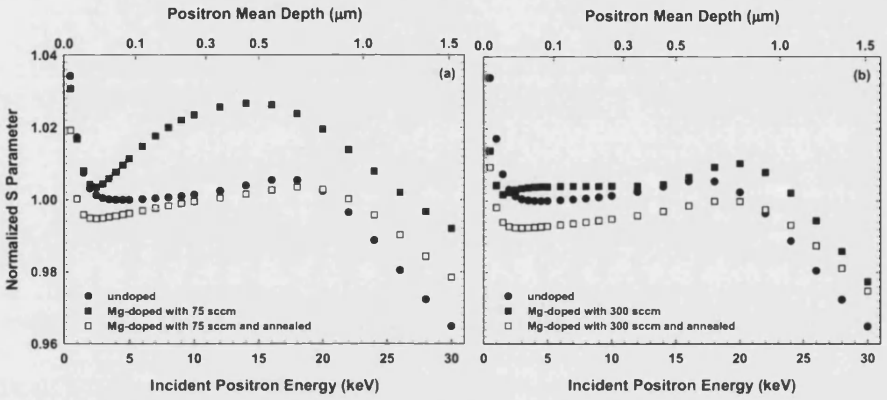

Figure 6.15 *S* parameter as a function of incident positron energy for (a) lightly Mg-doped GaN sample and (b) heavily Mg-doped GaN sample before and after annealing. The behaviour of the undoped sample is also shown for comparison.

PL measurements showed a broad red luminescence band peaked at ~ 1.8 eV, strongest in the lightly doped sample and becoming weaker as the Mg concentration is increased and vanishing after annealing. The ODMR signals detected in the 1.77-1.91 eV spectral region of the four as-grown Mg-doped samples are shown in figure 6.16. Both PL-enhancing and PL-quenching signals are observed. The sharp signal in the middle of the spectra is exclusively detected in the red luminescence band and is attributed to deep defects with energy level in the lower mid-gap region [127,129]. At the high field side of the sharp signal, two other overlapping luminescence-enhancing resonances are observed. From comparison with previous magnetic resonance work [127,134-136], the narrower resonance is attributed to shallow donors, while the broader signal is close to that of a deeper donor signal. In addition to the PL-enhancing lines, an asymmetric quenching signal is detected and it is attributed to shallow Mg-acceptors [134]. Based on the ODMR results presented above, a direct model of donor (shallow and/or deep) to deep centre recombination can be proposed to be the responsible

for the red emission, and the Mg-acceptor centre is believed to be involved in this process competing with the red emission. As in the PL spectra, the ODMR signals become weaker as the Mg concentration is increased. The signals are absent in undoped sample and suppressed after annealing in doped samples.

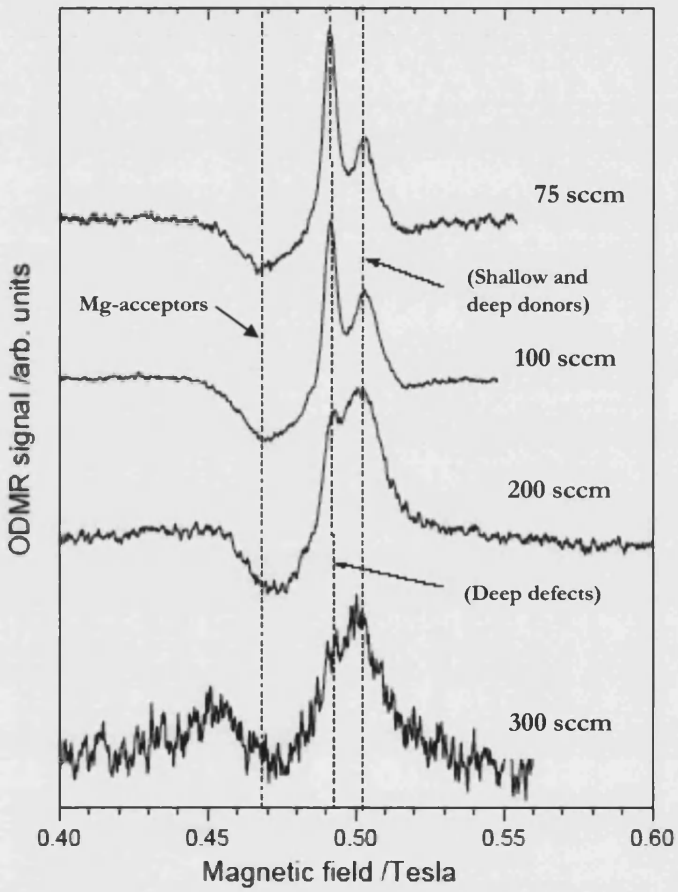

Figure 6.16 ODMR spectra detected on the 1.77 – 1.91eV red region for GaN samples doped with different Mg precursor flow rates (75, 100, 200 and 300 sccm). [Data taken by Bath optical spectroscopy group].

We now turn to the identity of the deep vacancy-related centre. Both V_{Ga} [132] and complexes of nitrogen vacancies associated with substitutional magnesium (V_N-Mg_{Ga}) [137] have been observed in GaN by PAS. Those vacancy-related defects would be expected to be negatively charged to act as positron traps. Calculations [138,139] have shown that the formation energy of V_{Ga} is increased as the Fermi

level moves towards the valence band. This explains the decrease of the strength of the red emission with Mg doping and annealing as the concentration of V_{Ga} decreases. Previous studies suggest that V_{Ga} is a deep acceptor with an energy level of about 1.0 eV above the valence band [141,140], and that V_N-Mg_{Ga} is a deep donor with an energy level at ~440meV below the conduction band [142,143]. PL results suggest the existence of V_{Ga} in the undoped sample. Those Ga vacancies have been observed in previous studies of undoped samples by PAS [125,131]. In the same study, Mg doping has been suggested to reduce the concentration of V_{Ga} where S_b values lower than that of undoped sample have been measured in Mg-doped samples. However, this is not the case in our measurements; as Mg-doped samples exhibited S_b higher than in the undoped sample, suggesting that V_{Ga} and/or a second type of vacancy-related defects, increases in concentration with increasing Mg concentration, must be existed in the doped samples. As mentioned earlier, V_N-Mg_{Ga} complexes have been also observed in GaN and were found to dominate over V_{Ga} in MOVPE grown layers [137].

For V_{Ga} to be observed in the ODMR spectrum, the vacancy would be expected to contain an odd number of holes in the optically-excited magnetic state and the *g*-value would be expected to be close to 2.00. However, V_N-Mg_{Ga} complex could also form the present deep centre, but PAS results require it to be neutral or negatively charged in order to trap the positrons. Under optical excitation the complex may lose an electron and become paramagnetic, leading again to an ODMR signal close to 2.00. It has been reported that the complex dissociates under p-type conditions [137] and therefore, with Mg doping and annealing, its concentration would be expected to decrease, leading to a decrease in the *S* parameter and the red emission.

Thus, a possible model for the deep centre involving V_{Ga} and V_N-Mg_{Ga} complexes is proposed here. An energy level diagram summarizing the recombination process is shown in figure 6.17. This diagram is very similar to a model that has been suggested earlier by Kaufmann [144] and Hofmann [145]. With both V_{Ga} and V_N-Ma_{Ga} included in the deep centre defects, the results can be understood as follows. In the undoped sample, the Fermi level is close to the middle of the band gap and

both V_{Ga} and V_N are exist, however, positrons are not sensitive to V_N because of their positive charge state. With light doping, the dopants are probably forming V_N-Mg_{Ga} centres with V_N; hence, the V_{Ga} concentration remains high and the Fermi level is barely affected. Both the neutral V_N-Mg_{Ga} and the negative V_{Ga} vacancy-related defects are now detected by PAS, and red luminescence is observed as a result of recombination process from deep donors to deep acceptors. Further increase of Mg dopants increases the concentration of V_N-Mg_{Ga} but decreases V_{Ga} concentration, as their formation energy is increased, leading to a decrease in the intensity of the red luminescence as well in the *S* parameter. Annealing of the samples increases the formation energy of V_{Ga} to be above 5eV under nitrogen-rich conditions [139] and hence they can not occur in appreciable concentrations, and as a consequence, the red luminescence is suppressed and the *S* parameter is further decreases.

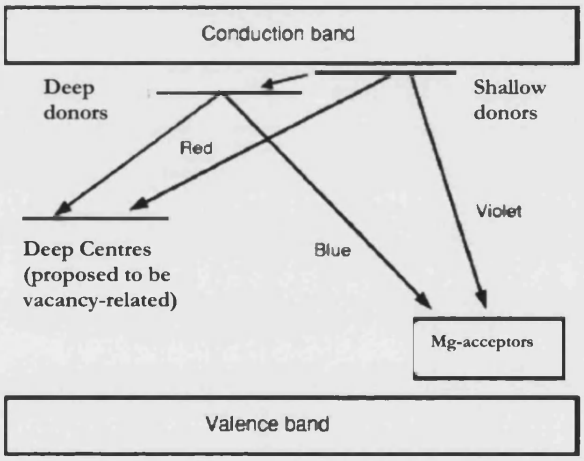

Figure 6.17 Schematic diagram for the recombination process giving rise to the red, blue, and violet bands of GaN.

6.2.4 Conclusion

In summary, epitaxial-grown and Mg-doped GaN layers have been studied using PAS and ODMR. We find that the change of the *S* parameter with Mg concentration and annealing is correlated with the behaviour of the PL and ODMR

signals in the red region, indicating that the red luminescence is vacancy-related. The results lead to the conclusion that the red emission is due to recombination between electrons both from shallow and deeper donors with deep centres and point out to the deep centres being vacancy-related defects.

Summary

In this thesis some examples of the applications of slow beam based positron annihilation spectroscopy (PAS) have been discussed. A review of PAS and a description of the University of Bath beam and the data analysis method were described in chapters 1 and 3. Chapter 2 presented some information and an overview of our concern in this work; namely the open-volume defects induced by ion implantation process.

The evolution of vacancy-type defects in various Si structures has been investigated in chapter 4. At-temperature measurements of the Doppler-broadening in the annihilation line have revealed different annealing behaviour of near-surface, vacancy-type defects induced by 50keV Si^+ ion implantation in Czochralski (Cz)- and epitaxial (epi)- grown Si wafers. Heating to temperatures of 300-500°C was found to cause clustering of implantation-induced defects in both types; however the clustering rate was noted to be faster in Cz-Si, probably due to the presence of impurities in this type facilitating the process. Higher temperatures (>500-640°C) were found to be necessary to anneal away the vacancy clusters in both types of Si, but again with faster annealing rate in Cz-grown samples. Clustering and annealing of implantation-induced defects in Cz-Si wafers implanted with 2MeV Si^+ ions have also been monitored to get an insight of the behaviour of deeper defects. The measured *S* parameter showed a constant response up to 600°C, above which agglomeration of divacancies (V_2) forming vacancy clusters of the size of hexavacancies (V_6), and eventually, annealing away or break up of these clusters with heating for long times at 600°C or going to higher temperatures have been observed. The constant PAS response upon annealing to temperatures in the range between 500-600°C, contrary to what is expected, has been

observed in other studies as mentioned in chapter 4 and it is attributed to vacancy aggregation, where vacancy agglomerates or clusters are formed upon V_2 migration.

A study of the effect of different annealing ambients on the response of vacancy clusters, induced by 60keV He^+ implantation and subsequent annealing at 900°C, in $Si_{0.82}Ge_{0.08}$ structure has been presented in the last section in chapter 4. Annealing in wet oxidizing ambient results in a reduction of the clusters' size probably from V_6 to V_4, while nitrogen ambient exhibited a greater effect as the clusters' size reduced to V_1, where some form of vacancy complexes must exist at this stage as monovacancies would not survive at room temperature. These observations are opposite to what is known in Si, where an oxidizing ambient has a bigger effect on the shrinkage of the clusters as interstitials, injected during the oxidation process, can easily diffuse into them. The difference between Si and SiGe is probably due to the presence of Ge and its effect in suppressing the interstitial injection into the substrate. Our results are in agreement with other studies investigating epitaxial SiGe layers using other techniques and also with proposed models describing the oxidation dynamics of SiGe.

Chapter 5 was concerned with fluorine (F)-related defects introduced by F implantation in Si and Si-SiGe-Si structures and their role in retarding boron transient enhanced diffusion (TED). Fluorine-vacancy (FV) complexes have been directly observed in both structures, and with the support of secondary ion mass spectrometry (SIMS) they have been identified to be of the form of $F_{3n}V_n$ or $F_{4n}V_n$ in Si and Si-SiGe-Si, respectively, with n most likely to be 1 and/or 2. Such FV complexes have been suggested earlier in other experimental and theoretical studies as a likely candidate for explaining boron TED suppression in F-implanted Si. The vacancies trapped by the F atoms are believed to have the ability to trap the interstitials migrating from the end-of-range (EOR) region and thus have significant effect on reducing B diffusion. In our work, both VEPAS and SIMS results have suggested a decrease in the concentration of the FV complexes with increasing the annealing time at 800°C, in Si, or the annealing temperature, in Si-SiGe-Si structure.

Two examples of the use of VEPAS in investigating vacancy-type defects in compound semiconductors, namely indium phosphide (InP) and gallium nitride (GaN) from III-V group, have been presented in chapter 6. In the first example, the ability of VEPAS to detect cavities of the size of a few nm in He^+-implanted InP has been examined. A high *S* parameter of ~1.07 was measured after 70keV He^+ implantation at $5x10^{16}$ and subsequent annealing for a short time at 640°C, indicating the formation of large vacancy clusters but not of the size that was expected to be created in the sample. This opened a discussion about the sensitivity of VEPAS to the presence of nanovoids or cavities. It appeared from this study as well as the study of He^+-implanted $Si_{0.82}Ge_{0.08}$ mentioned earlier that such cavities are not visible to positrons as they are possibly annihilating in smaller open-volume defects existing around them or at their internal surfaces. The second example detailed the results obtained from the collaboration between VEPAS and optically-detected magnetic resonance (ODMR) in studying magnesium (Mg)-doped GaN. Changes in the *S* parameter with Mg concentration were correlated with the ODMR signals, and it has been concluded that the red luminescence is due to recombination between electrons from shallow and/or deep donors with deep centres which are believed to be vacancy-related defects.

In conclusion, we have demonstrated in the studies carried out during this PhD that VEPAS is a powerful defect characterization tool, by which valuable information can be obtained about the identity of open-volume defects in the sub-surface regions of the samples under investigation and up to a few μm. The study of such defects is of significant importance in semiconductor device technology.

References

[1] C.D. Anderson, Phys. Rev. **43,** 491 (1933).

[2] P.A.M. Dirac, Proc. Comb. Phil. Soc. **26,** 361 (1930).

[3] E. Bellotti, M. Corti, E. Fiorini, C. Ligouri, A. Pullia, A. Sarracino, P. Sverzellati, L. Zanotti, Phys. Lett. B **124,** 435 (1983).

[4] S.Mohorovicic, Astron. Nachr **253,** 93 (1934).

[5] M.Deutsch, Phys. Rev. **82,** 455 (1951).

[6] S.Dannefaer, D.Kerr, and D.Craigen, J. Appl. Phys. **79,** 9110 (1996).

[7] Y.Itoh, H.Murakami, and A.Kinoshita, Hyperf. Interact. **84,** 121 (1994).

[8] P. Hautojärvi (ed.), *Positrons in Solids,* Springer-Verlag, Berlin (1979).

[9] R. Krause-Rehberg and H.S. Leipner, *Positron Annihilation in Semiconductors: Defect Studies*, Springer, Berlin (1999).

[10] P. Kirkegaard, N.J. Pedersen, and M. Eldrup, In positron annihilation, L. Dorikens-Vanpraet, M. Dorikens, and D. Segers (eds.), World Scientific, Singapore (1989).

[11] L. Madanski and F. Rasetti, Phys. Rev. **79,** 397 (1950).

[12] K.G. Lynn, Phys. Rev. Letts. **43,** 391 (1979).

[13] A.P.Jr. Mills, Phys. Rev. Letts. **41,** 1828 (1978).

[14] J.M. Dale, L.D. Hulett, and S. Pendyala, Surf. Interface Anal. **2,** 199 (1980).

[15] T. Akahane, T. Shiba, N. Shiotani, S. Tanigawa, T. Mikado, R. Suzuki, M. Chiwaki, T. Yamazaki, T. Tominasu, Appl. Phys. A **51,** 146 (1990).

[16] G. Kögel, D. Schödlbauer, W. Trifshäuser, and J. Winter, Phys. Rev. Letts. **60,** 1550 (1988).

[17] A.F. Makhov, Sov. Phys. Sol. State **2,** 1934 (1961).

[18] S. Valkealahti and R.M. Nieminen, Appl. Phys. A **35,** 51 (1984).

[19] A. Vehanen, K. Saarinen, P. Häutojarvi, and D. Mathiot, Phys. Rev. B **35,** 4606 (1987).

[20] J. Mäkinen, C. Corbel, P. Häutojarvi, and D. Mathiot, Phys. Rev. B **43,** 12114 (1991).

[21] Nielsen, Bent, K.G. Lynn, A. Vehanen, P.J. Schultz, Phys. Rev. B **32,** 2296 (1985).

[22] S. Mäkinen, H. Rajainmäki, and S.Linderoth, Phys. Rev. B **42,** 11166 (1990).

[23] W. Brandt and R. Paulin, Phys. Rev. B **5,** 2430 (1972).

[24] S. DeBenedetti, C. Cowan, and W.R. Konneker, Phys. Rev. **76,** 440 (1949).

[25] S. Berko and H.N. Pendleton, Annu. Rev. Nucl. Part. Sci. **30,** 543 (1980).

[26] R.N. West, ICPA7; Proc. of the 7th Int. Conf. on Pos. Ann., 1 (1985).

[27] I.K. Mackenzie, T.L. Khoo, A.B. McDonald, and B.T. McKee, Phys. Rev. Letts. **19,** 946 (1967).

[28] S.M. Sze, *Semiconductor devices: Physics and Technology*, Wiley, New York (2002).

[29] H. Ryssel and I. Ruge, *Ion Implantation*, Wiley, New York (1986).

[30] J.F. Ziegler, J.P. Biersack, and U. Littmark. The Stopping and Range of ions in Solids, Pergamon Press, New York (1985).

[31] P. Hautojärvi, H. Huomo, J. Lahtinen, J. Mäkinen, A. Vehanen, Mater. Sci. Forum **10-12,** 527 (1986).

[32] G.D. Watkins and J.W. Corbett, Phys. Rev. **138,** A543 (1965).

[33] J.L. Lindström, L.I. Murin, V.P. Markevich, T. Hallberg, and B.G. Svensson, Physica B **273/274,** 291 (1999).

[34] L.J. Cheng, J.C. Corelli, J.W. Corbett, and G.D. Watkins, Phys. Rev. **152,** 761 (1966).

[35] P. Pellegrino, P. Lévêque, J. Lalita, and A. Hallén, Phys. Rev. B **64,** 195211 (2001).

[36] G. Alfieri, E.V. Monakhov, B.S. Avset, and B.G. Svensson, Phys. Rev. B **68,** 233202 (2003).

[37] V.P. Markevich, A.R. Peaker, S.B. Lastovskii, L.I. Murin, and J.L. Lindström, J. Phys.: Condens. Matter **15,** S2779-S2789 (2003).

[38] E.V. Monakhov, A. Ulyashin, G. Alfieri, A. Yu. Kuznetsov, B.S. Avset, and B.G. Svensson, Phys. Rev. B **69,** 153202 (2004).

[39] Y.-H. Lee and J.W. Corbett, Phys. Rev. B **13,** 2653 (1976).

[40] A. Uedono, Y. Ujihira, L. Wei, Y. Tabuki, S. Tanigawa, J. Sugiura, M. Ogasawara, and M. Tamura, Mater. Res. Soc. Symo. Proc. **262,** 1061 (1992).

[41] M. Fujinami, Phys. Rev. B **53,** 13047 (1995).

[42] R.D. Goldberg, P.J. Schultz, and P.J. Simpson, Appl. Surf. Sci. **85,** 287 (1995).

[43] D.A. Abdulmalik, P.G. Coleman, N.E.B. Cowern, A.J. Smith, B.J. Sealy, W. Lerch, S. Paul, and F. Cristiano, Appl. Phys. Lett. **89,** 052114 (2006).

[44] G.M.Lopez, V. Fiorentini, G. Impellizzeri, S. Mrabella, and E. Napolitani, Phys. Rev. B **72,** 045219 (2005).

[45] R.M. Nieminen and J. Laakkonen, Appl. Phys. **20,** 181 (1979).

[46] M. Fujinami, A. Tsuge, and K. Tanaka, J. Appl. Phys. **79,** 9017 (1996).

[47] B. Nielsen, O.W. Holland, T.C. Leung, and K.G. Lynn, J. Appl. Phys. **74,** 1636 (1993).

[48] S. Dannefaer, A. Avalos, D. Kerr, R. Poirier, V. Shmarovoz, and S.H. Zhang, Phys. Rev. B **73,** 115202 (2006).

[49] P.J. Simpson, M. Vos, I.V. Mitchell, C. Wu, and P.J. Schultz, Phys. Rev. B **44,** 12180 (1991).

[50] D.A. Abdulmalik, P.G. Coleman, and I.Y. Al-Qaradawi, Appl. Surf. Sci. **252,** 3209 (2006).

[51] T.E.M. Staab, A. Sieck, M. Haugk, M.J. Puska, Th. Frauenheim, and H.S. Leipner, Phys. Rev. B **65,** 115210 (2002).

[52] D.V. Makhov and L.J. Lewis, Phys. Rev. Lett. **92,** 255504 (2004).

[53] S.K. Estreicher, Phys. Status. Solidi (b) **217,** 513 (2000).

[54] M.N. Kham, H.A.W. El Mubarek, J.M. Bonar, and P. Ashburn, Mater. Sci. Eng. B **124-125,** 192 (2005).

[55] J.S. Williams, Mater. Sci. Eng. A **253,** 8 (1998).

[56] J. Wong-Leung, E. Nygren, and J.S. Williams, Appl. Phys. Lett. **67,** 416 (1995).

[57] O.V. Feklisova and E.B. Yakimov, Solid State Phenom. **95-96,** 495 (2004).

[58] A.P. Knights and P.G. Coleman, Defects and Diffusion Forum **183-185,** 41 (2000).

[59] N.B. Chilton and P.G. Coleman, Meas. Sci. Technol **6,** 53 (1995).

[60] I.K. Mackenzie, J.A. Eddy, and R.R. Gingerich, Phys. Letts. A **33,** 279 (1970).

[61] M. Clement, J.M.M. de Nijs, P. Balk, H. Schut, and A. van Veen, J. Appl. Phys. **79,** 9029 (1995).

[62] A.van Veen, H. Schut, J. De Vries, R.A. Hakvoort, and M.R. Ijpma, in *AIP Conf. Proc.* **218,** 171 (1990).

[63] S. Eichler, J. Gebauer, F. Börner, A. Polity, R. Krause-Rehberg, E. Wendler, B. Weber, W. Wesch, and H. Börner, Phys. Rev. B **56,** 1393 (1997).

[64] R. Kalyanaraman, T.E. Haynes, O.W. Holland, H.-J.L. Gossman, C.S. Rafferty, and G.H. Gilmer, Appl. Phys. Lett. **79,** 1983 (2001).

[65] P.G. Coleman, F. Malik, and A.P. Knights, J. Phys.: Condens. Matter **14,** 681 (2002).

[66] A. Uedono, S. Tanigawa, A. Ogura, H. Ono, R. Suzuki, T. Ohdaira, and T. Mikado, J. Appl. Phys. **87,** 1659 (2000).

[67] A.Uedono, T. Kitano, K. Hamada, T. Moriya, T. Kawano, S. Tanigawa, R. Suzuki, T. Ohdaira, and T. Mikado, Jap. J. Appl. Phys. Part 1 **36,** 2571 (1997).

[68] R. Poirier, V. Avalos, S. Dannefaer, F. Schiettekatte, and S. Roorda, Physica B **340-342,** 609 (2003).

[69] V. Avalos and S. Dannefaer, Phys. Rev. B **54,** 1724 (1996) and references therein.

[70] P.G. Coleman (ed.), *Positron Beams and their applicatios,* World Scientific, Singapore (2000).

[71] M. Xu and X.Q. Feng, Theoretical and Applied Fracture Mechanics **42,** 295 (2004).

[72] R. Kalyanaraman, T.E. Haynes, M. Yoon, B.C. Larson, D.C. Jacobson, H.J.L. Gossmann, and C.S. Rafferty, Nucl. Instrum. Methods Phys. Res. , B **175-177,** 182 (2001).

[73] G.H. Gilmer, T.D. de la Rubia, D.M. Stock, and M. Jaraiz, Nucl. Instrum. Methods Phys. Res. ,B **102,** 247 (1995).

[74] J.L. Benton, S. Libertino, P. Kringhøj, D.J. Eaglesham, J.M. Poate, and S. Coffa, J. Appl. Phys. **82,** 120 (1997).

[75] G.D. Watkins, Mater. Sci. Semicond. Process. **3,** 227 (2000).

[76] X.D. Pi, C.P. Burrows, P.G. Coleman, R.M. Gwilliam, and B.J. Sealy, J. Phys.: Condens Matter **15,** S2825 (2003).

[77] S. Szpala and P.J. Simpson, J. Appl. Phys. **89,** 5991 (2001).

[78] X.D. Pi, C.P. Burrows, and P.G. Coleman, Appl. Surf. Sci. **194,** 255 (2002).

[79] S. Libertino, S. Coffa, C. Spinella, A.L. Magna, and V. Privitera, Nucl. Instrum. Methods Phys. Res. , Sect. B **178,** 25 (2001).

[80] V. Privitera, S. Coffa, F. Priolo, K.K. Larsen, S. Libertino, and A. Carnera, Nucl. Instrum. Methods Phys. Res. Sect. B **120,** 9 (1996).

[81] D.J. Paul, Semicond. Sci. Technol. **19,** R75 (2004).

[82] M. Spadafora, A. Terrasi, S. Mirabella, A. Piro, M.G. Grimaldi, S. Scalese, E. Napolitani, M. Di Marino, D. De Salvador, and A. Carnera, Mat. Sci. Semi. Proc. **8,** 219 (2005).

[83] E. Napolitani, M. Di Marino, D. De Salvador, A. Carnera, M. Spadafora, M. Mirabella, A. Terrasi, and S. Scalese, J. Appl. Phys. **97,** 036106 (2005).

[84] M.A. Rabie, Y.M. Haddara, and J.J. Carette, J. Appl. Phys. **98,** 074904 (2005).

[85] R.S. Brusa, G.P. Karwasz, N. Tiengo, and A. Zecca, Phys. Rev. B **61,** 10154 (2000).

[86] V. Raineri, M. Saggio, and E. Rimini, J. Mater. Res. **15,** 1449 (2000).

[87] P.J. Simpson and A.P. Knights, Mater. Sci. Forum **445-446,** 180 (2004).

[88] M. Uematsu, H. Kageshima, and K. Shiraishi, Comput. Mater. Sci. **24,** 229 (2002).

[89] V. Raineri, S. Giuffrida, and E. Rimini, Appl. Phys. Lett. **79,** 3959 (2001).

[90] M. Clement, J.M.M. de Nijs, P. Balk, H. Schut, and A. van Veen, J. Appl. Phys. **79,** 9029 (1996).

[91] N.E.B. Cowern, B. Colombeau, J. Benson, A.J. Smith, W. Lerch, S. Paul, T. Graf, F. Cristiano, X. Hebras, and D. Bolze, Appl. Phys. Lett. **86,** 101905 (2005).

[92] P.J. Simpson, Z. Jenei, P. Asoka-Kumar, R.R. Robison, and M.E. Law, Appl. Phys. Lett. **85,** 1538 (2004).

[93] X.D. Pi, C.P .Burrows, and P.G. Coleman, Phys. Rev. Lett. **90,** 155901 (2003).

[94] G. Impellizzeri, J.H.R. dos Santos, S. Mirabella, F. Priolo, E. Napolitani, and A. Carnera, Appl. Phys. Lett. **84,** 1862 (2004).

[95] H.A.W. El Mubarek and P. Ashburn, Appl. Phys. Lett. **83,** 4134 (2003).

[96] G.M. Lopez and V. Fiorentini, Appl. Phys. Lett. **89,** 092113 (2006).

[97] M. Diebel and S.T. Dunham, Phys. Rev. Lett. **93,** 245901 (2004).

[98] C.C. Ling, Y.F. Shek, A.P. Huang, S. Fung, and C.D. Beling, Phys. Rev. B **59,** 5751 (1999).

[99] Y.Y. Shan, P. Asoka-Kumar, and K.G. Lynn, Phys. Rev. B **54,** (1996).

[100] C.Corbel, P. Hautojärvi, J. Makinen, A. Vehanen, and D. Mathiot, J. Phys.: Condens Matter **1,** 6315 (1989).

[101] D.T. Britton, P. Willutzki, W. Triftshauser, E. Hammerl, W. Hansch, and I. Eisele, Appl. Phys. A **58,** 389 (1994).

[102] Y.F. Shek, C.C. Ling, C.D. Beling, and S. Fung, Appl. Phys. A **74,** 233 (2002).

[103] A.H. Deng, Y.Y. Shan, S. Fung, and C.D. Beling, J. Appl. Phys. **91,** 3931 (2001).

[104] J.A. Duffy, W. Bauer-Kugelmann, G. Kögel, and W. Triftshäuser, Appl. Surf. Sci. **116,** 241 (1997).

[105] A.P. Knights and P.G. Coleman, Mater. Sci. Forum. **445-446,** 123 (2004).

[106] S. Dannefaer, J. Phys. C **15,** 599 (1982).

[107] P.J. Schultz, E. Tandberg, K.G. Lynn, B. Nielsen, T.E. Jackman, M.W. Denhoff, and G.C. Aers, Phys. Rev. Lett. **61,** 187 (1988).

[108] G. Impellizzeri, J.H.R. dos Santos, S. Mirabella, E. Napolitani, A. Carnera, and F. Priolo, Nucl. Instrum. Methods Phys. Res. B **230,** 220 (2005).

[109] T. Noda, J. Appl. Phys. **96,** 3721 (2004).

[110] J. Slotte, Nucl. Instrum. Methods Phys. Res. B **253,** 130 (2006).

[111] H.A.W. El Mubarek, M. Karunaratne, J.M. Bonar, G.D. Dilliway, Y. Wang, P.L.F. Hemment, A.F. Willoughby, and P. Ashburn, IEEE Trans. Electron Devices **52,** 518 (2005).

[112] P.G. Coleman, N.B. Chilton, and J.A. Baker, J. Phys.: Condens. Matter **2,** 9355 (1990).

[113] M.Y. Tsai, D.S. Day, B.G. Streetman, P. Williams, C.A. Evans, and Jr., J. Appl. Phys. **50,** 188 (1979).

[114] S.-P.Jeng, T.-P. Ma, R. Canteri, M. Anderleb, and G.W. Rubloff, Appl. Phys. Lett. **61,** 1311 (1992).

[115] L. Wei, S. Tanigawa, and A. Uedono, Hyperfine Interact. **84,** 243 (1994).

[116] P.J. Schultz, P.J. Simpson, U.G. Akano, and I.V. Mitchell, In Materials Modification by Energetic Atoms and Ions Symposium. K.S.Grabowski, S.A.Barnett, S.M.Rossnagel, and K.Wasa (eds.). Mater. Res. Soc. Pittsburgh, 319 (1992).

[117] P.J. Simpson, U.G. Akano, P.J. Schultz, and I.V. Mitchell, Mater. Sci. Form **105-110,** 1435 (1992).

[118] Z.Q. Chen and S.J. Wang, Semicond. Sci. Technol **14,** 271 (1999).

[119] M. Tiginyanu, A.I. Terletsky, and V.V. Ursaki, Solid State Commun. **96,** 789 (1995).

[120] N. Dharmarasu, B. Sundarakkannan, R. Kesavamoorhy, K.G.M. Nair, and J. Kumar, Physica B **262,** 329 (1999).

[121] P.J. Simpson, I.V. Mitchell, G.O. Este, and F.R. Shepherd, Nucl. Instrum. Methods Phys. Res. B **148,** 381 (1999).

[122] M. Chicoine, S. Roorda, R.A. Masut, and P. Desjardins, J. Appl. Phys. **94,** 6116 (2003).

[123] A.P. Knights, F. Malik, and P.G. Coleman, Appl. Phys. Lett. **75,** 466 (1999).

[124] N.R. Potter and P.G. Coleman, Phys. Status Solidi, accepted for publication.

[125] J. Oila, V. Ranki, J. Kivioja, K. Saarinen, P. Hautojärvi, J. Likonen, J.M. Baraanowski, K. Pakula, T. Suski, M. Leszczynski, and I. Grzegory, Phys. Rev. B **63,** 1 (2001).

[126] J. Oila, K. Saarinen, A.E. Wickenden, D.D. Koleske, R.L. Henry, and M.E. Twigg, Appl. Phys. Lett. **82,** 1021 (2003).

[127] M.W. Bayeri, M.S. Brandt, O. Ambacher, M. Stutzmann, E.R. Glaser, R.L. Henry, A.E. Wickenden, D.D. Koleske, T. Suski, I. Grzegory, and S. Porowski, Phys. Rev. B **63,** (2001).

[128] B.K. Meyer, Semiconductors and Semimetals **57,** 371 (1999).

[129] M.W. Bayeri, M.S. Brandt, E.R. Glaser, A.E. Wickenden, D.D. Koleske, R.L. Henry, and M. Stutzmann, Phys. Status Solidi (b) **216,** 547 (1999).

[130] Y.A. Kennedy and E.R. Glaser, *in Identification of Defects in Semiconductors, Semiconductors and Semimetals*, M. Stavola (ed.), Academic, San Diego, 51A, p. 93-136 (1998).

[131] J. Moxom, J. Xu, R. Suzuki, T. Ohdaira, G. Brandes, and J.S. Flynn, J. Appl. Phys. **92,** 1898 (2002).

[132] K. Saarinen, T. Laine, S. Kuisma, J. Nissilä, P. Hautojärvi, L. Dobrzynski, J.M. Baranowski, K. Pakula, R. Stepniewski, M. Wojdak, A.

Wysmolek, T. Suski, M. Leszczynski, I. Grzegory, and S. Porowski, Phys. Rev. Lett. **79,** 3030 (1997).

[133] X.D. Pi, P.G. Coleman, C.L. Tseng, C.P. Burrows, B. Yavich, and W.N. Wang, J. Phys.: Condens. Matter **14,** L243-L248 (2002).

[134] E.R. Glaser, W.E. Carlos, G.C.B. Braga, J.A. Freitas Jr., W.J. Moore, B.V. Shanabrook, R.L. Henry, A.E. Wickenden, D.D. Koleske, H. Obloh, P. Kozodoy, S.P. DenBaars, and U.K. Mishra, Phys. Rev. B **65,** 085312 (2002).

[135] E.R. Glaser, T.A. Kennedy, J.A. Freitas Jr., B.V. Shanabrook, A.E. Wickenden, D.D. Koleske, R.L. Henry, and H. Obloh, Physica B **273-274,** 58 (1999).

[136] W.E. Carlos, J.A. Freitas, M. AsifKhan, D.T. Olson, and J.N. Kuznia, Phys. Rev. B **48,** 17878 (1993).

[137] S. Hautakangas, J. Oila, M. Alatalo, K. Saarinen, L. Liszkay, D. Seghier, and H.P. Gislason, Phys. Rev. Lett. **90,** 137402 (2003).

[138] T. Mattila and R.M. Nieminen, Phys. Rev. B **55,** 9571 (1997).

[139] J. Neugebauer and C.G. Van de Walle, Phys. Rev. B **50,** 8067 (1994).

[140] E. Calleja, F.J. Sánchez, D. Basak, M.A. Sánchez-Garsía, E. Muňoz, I. Izpura, F. Calle, J.M.G. Tijero, J.L. Sánchez-Rojas, B. Beaumont, P. Lorenzini, and P. Gibart, Phys. Rev. B **55,** 4689 (1997).

[141] J. Neugebauer and C.G. Van de Walle, Appl. Phys. Lett. **68,** 1829 (1996).

[142] O. Gelhausen, M.R. Phillips, E.M. Goldys, T. Paskova, B. Monemar, M. Strassburg, and A. Hoffmann, Phys. Rev. B **69,** 125210 (2004).

[143] U. Kaufmann, M. Kunzer, M. Maier, H. Obloh, A. Ramakrishnan, B. Santic, and P. Schlotter, Appl. Phys. Lett. **72,** 1326 (1998).

[144] U. Kaufmann, M. Kunzer, H. Obloh, M. Maier, Ch. Manz, A. Ramakrishnan, and B. Santic, Phys. Rev. B **59,** 5561 (1999).

[145] D.M. Hofmaun, B.K. Meyer, H. Alves, F. Leiter, W. Burkhard, N. Romanov, Y. Kim, J. Kruger, and E.R. Weber, Phys. Status Solidi (a) **180,** 261 (2000).